ABSTRACT

Title of Thesis: APPLICATION OF X-RAY PULSAR NAVIGATION: A CHARACTERIZATION OF THE EARTH ORBIT TRADE SPACE

Wayne Hong Yu, Master of Science, 2015

Thesis directed by: Dr. Liam Healy
Department of Aerospace Engineering

The potential for pulsars as a navigation source has been studied since their discovery in 1967. X-ray pulsar navigation (XNAV) is a celestial navigation system that uses the consistent timing nature of X-ray photons from milli-second pulsars (MSP) to perform space navigation. Much of the challenge of XNAV comes from the faint signal, availability, and distant nature of pulsars. This thesis is the study of pulsar XNAV measurements for extended Kalman filter (EKF) tracking performance within a wide trade space of bounded Earth orbits, using a simulation of existing X-ray detector space hardware. An example of an X-ray detector for XNAV is the NASA Station Explorer for X-ray Timing and Navigation (SEXTANT) mission, a technology demonstration of XNAV set to perform on the International Space Station (ISS) in 2016.

The study shows that the closed Earth orbit for XNAV performance is reliant on the orbit semi-major axis and eccentricity as well as orbit inclination. These parameters are the primary drivers of pulsar measurement availability and significantly influence the natural spacecraft orbit dynamics. Sensitivity to initial orbit determination error growth due to the scarcity of XNAV measurements within an orbital period require appropriate timing of initial XNAV measurements. The orbit angles of argument of perigee and right ascension of the ascending node, alongside the other orbit parameters, complete the initial cadence of XNAV measurements. The performance of initial XNAV measurements then propagates throughout the experimental period.

www.manaraa.com

APPLICATION OF X-RAY PULSAR NAVIGATION: A CHARACTERIZATION OF THE EARTH ORBIT TRADE SPACE

by

Wayne Hong Yu

Thesis submitted to the Faculty of the Graduate School of the
University of Maryland, College Park in partial fulfilment
of the requirements for the degree of
Masters of Science
2015

Advisory Committee:
Dr. Liam M. Healy, Chair/Advisor
Associate Professor Raymond J. Sedwick
Assistant Professor Christine M. Hartzell

www.manaraa.com

© Copyright by
Wayne Hong Yu
2015

www.manaraa.com

Preface

The views expressed in this thesis are those of the author and do not reflect the official policy or position of the National Aeronautics and Space Administration or the United States Government.

"If you want to build a ship, don't drum up people to collect wood and don't assign them tasks and work, but rather teach them to long for the endless immensity of the sea."

Antoine de Saint-Exupéry

www.manaraa.com

Dedication

To my father, Yan Pong Yu. I present my thesis in honor and respect to you.

www.manaraa.com

Acknowledgements

There are many that I would like to thank for the years it has taken to accomplish this thesis. First and foremost, I would like to thank my advisor Dr. Healy for his support and guidance as well as thesis committee members Dr. Raymond Sedwick and Dr. Christine Hartzell for their guidance and support throughout my thesis. I would like to give a special thanks to Dr. Dave Akin and the University of Maryland Space Systems Lab for providing me the career opportunity that began my research in the first place.

Due to the thesis' relationship with NASA, I would like to thank the many staff members at the NASA Goddard Spaceflight Center that have supported and vetted my research. I would like to thank the NASA SEXTANT team, in particular Dr. Jason Mitchell, Dr. Luke Winternitz, and Ms. Jennifer Valdez for providing the support material to experiment on this thesis. I would also like to thank Dr. Paul Ray and Dr. Kent Wood from the Naval Research Laboratory for their guidance on the structure of milli-second pulsars. I would also like to thank Dr. J. Russell Carpenter, Dr. Alinda Mashiku, Dr. Trevor Williams, and Dr. Conrad Schiff for their added support throughout my graduate studies.

In addition, I would like to thank my family and friends for their patience. In particular, I would like to thank my parents for instilling the balance between passion and obsession in my studies. Finally, I would like to thank my beautiful girlfriend Ms. Katherine McBryan for the mutual support we have shared all these years. I am eternally grateful to you all.

www.manaraa.com

Table of Contents

www.manaraa.com

www.manaraa.com

www.manaraa.com

List of Tables

www.manaraa.com

List of Figures

www.manaraa.com

www.manaraa.com

www.manaraa.com

www.manaraa.com

List of Abbreviations

AOP	Argument of Periapsis
ARGOS	Advanced Research and Global Observation Satellite
BCI	Body-Centered Inertial
CRLB	Cramér-Rao Lower Bound
DARPA	Defense Advanced Research Projects Agency
ΔDOR	Delta Differential One way Ranging
DOF	Degree of Freedom
DSN	Deep Space Network
ECEF	Earth Centered Earth Fixed
ECI	Earth Centered Inertial
ECC	Eccentricity
EKF	Extended Kalman Filter
ELC	ExPRESS Logistics Carrier
FRAM	Flight Releasable Attachment Mechanism
GEONS	Goddard's Enhanced Onboard Navigation System
GEO	Geosynchronous Earth Orbit
GMAT	General Mission Analysis Tool
GPS	Global Positioning System
INC	Inclination
ISS	International Space Station
JPL	Jet Propulsion Laboratory
LEO	Low Earth Orbit
LOS	Line of Sight
MLE	Maximum Likelihood Estimation
MSP	Millisecond Pulsar

www.manaraa.com

NASA	National Aeronautics and Space Administration
NHPP	non-homogeneous Poisson process
NICER	Neutron-star Interior Composition ExploreR
NRL	Naval Research Laboratory
NOAA	National Oceanic and Atmospheric Administration
RAAN	Right Ascension of Ascending Node
RIC	Radial, In-track, Cross-track Spacecraft-fixed Rotating Reference Frame
RSS	Root Sum Square
RXTE	Rossi X-ray Timing Explorer
SAA	South Atlantic Anomaly
SEXTANT	Station Explorer for X-ray Timing and Navigation Technology
SMA	Semi-Major Axis
SNR	Signal-to-Noise Ratio
SPICE	Spacecraft Planet Instrument C-matrix Events
STMD	Space Technology Mission Directorate
TA	True Anomaly
TOA	Time-of-Arrival
UMCP	University of Maryland at College Park
VBLI	Very Long Baseline Interferometry
XNAV	X-ray Pulsar Navigation

www.manaraa.com

Chapter 1: Introduction

This thesis is a study of pulsar XNAV space navigation tracking performance with a wide trade space of bounded natural Earth orbits. This is done by simulating existing X-ray detector space hardware. This chapter introduces the concept of XNAV and describes the overall structure of the thesis. It includes the motivation, an introduction, and a summary of the other chapters. If there are any unknown acronyms, please refer to the list of abbreviations.

1.1 Motivation

The human endeavor of exploration, be it on Earth or beyond, stems from an instinctual nature to understand the unknown and to return that knowledge back home. With space exploration, one of the most fundamental requirements to this endeavor is spacecraft navigation. The traditional techniques of space navigation are heavily based upon Earth ground based assets/operations and are used for missions that have a proximity to Earth. However, range uncertainty increases as the distance to these assets increase [6]. With spacecraft missions away from Earth, the current most critical ground based asset is the Deep Space Network (DSN). Using techniques such as the Very Long Baseline Interferometry (VBLI), DSN can provide 1-10 km

www.manaraa.com

position accuracy per AU of distance from Earth [35]. With Delta Differential One way Ranging (ΔDOR), that accuracy is equivalent to about 4 km position accuracy per AU of distance from Earth [33]. DSN also supports a wider range of mission phases compared to other navigation assets due to its versatility [6] [23]. However, this means that DSN is in high demand for a system with finite resources.

With the limited availability of DSN ground stations due to their extensive operations and an increased demand for interplanetary missions, there is a benefit to exploring other navigation assets [2]. XNAV is one such asset. The navigation technique uses the observation of celestial X-ray sources to provide both timing and position navigation measurements in a manner similar to Global Positioning System (GPS) [46]. Because the timing models of pulsars can be kept on board a spacecraft to cross reference and generate a navigation measurement, XNAV can perform navigation on board the spacecraft. Due to the control input demands of formation flight, relative autonomous navigation has also been a potential application of XNAV [23] [53]. Due to the timing information provided by XNAV, XNAV will be applicable to planetary, interplanetary, and interstellar navigation.

As such, there is a push to demonstrate XNAV in space as a potential navigation asset. Even though XNAV can provide measurements in Earth orbits as well as other interplanetary missions, navigation assets such as GPS have a higher update frequency and provide a more accurate state estimate near Earth. On the other hand, interplanetary missions far from Earth that could directly be enhanced by XNAV would incur a significant cost and risk without further demonstration missions.

www.manaraa.com

As a result, the National Aeronautics and Space Administration (NASA) SEXTANT demonstration mission will demonstrate XNAV for the first time on the ISS in LEO [19]. This mission is an opportunity to demonstrate XNAV with lower cost and risk than an ideal XNAV mission. It will also provide insight on similar orbits if they are applied at other planetary bodies. If DSN needs support or if another navigation asset is required for a planetary mission, XNAV can provide that support. SEXTANT will also be a single data point of reference to demonstrate XNAV as a potential navigation asset. Future near Earth missions that demonstrate XNAV would be a reasonable next step in vetting XNAV as a navigation asset.

With these considerations in mind, the thesis describes an extension of XNAV performance into general bounded Earth orbits. This knowledge could help support future demonstrations around Earth as well as other planetary bodies. The author hopes to add knowledge of tracking performance as a reference for future missions considering XNAV as a navigation asset.

1.2 Pulsar XNAV Concept Overview

This is a concept overview of XNAV navigation. It is an idealized perception to convey how a wave front of photons is converted into navigation information.

Consider two observers and a single source that emits photons. At a time t, that source emits a wave front of photons towards the two observers. As seen in Figure 1.1, these photon wave fronts arrive in succession to each observer. Both observers locally time when the same photon wave front arrives at their location. It

www.manaraa.com

is assumed that sufficient accuracy and precision in the timing process and in the synchronization of absolute time between observers is achieved. With that assumption, the distance Δd between these two observers would be proportional, within first order, to the time delay t_d between both observers. A visual representation can be seen in Figure 1.1.

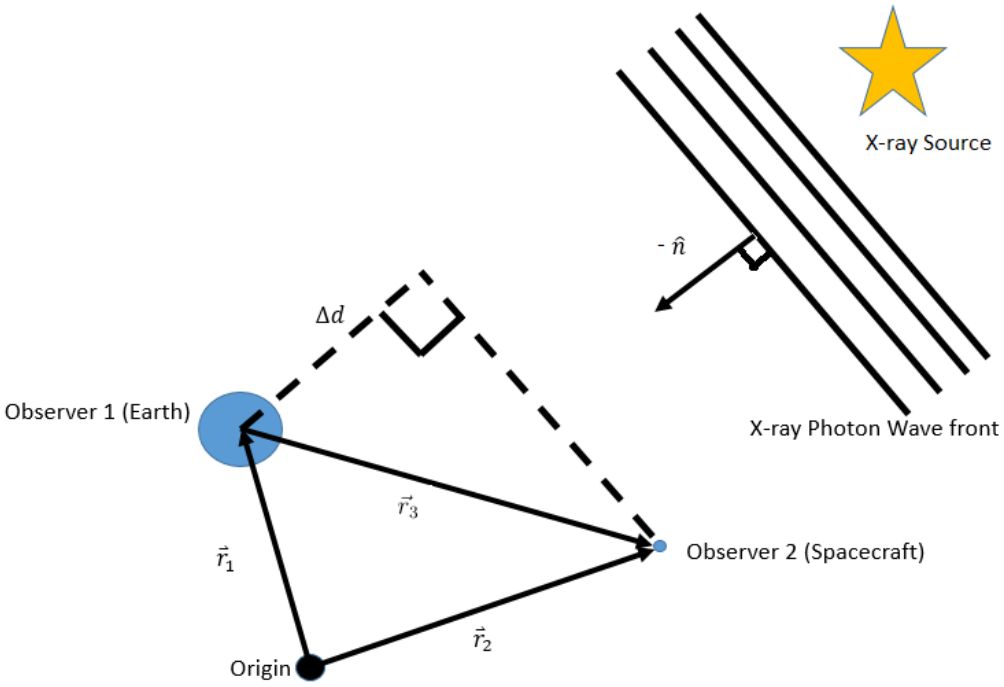

Figure 1.1: XNAV Diagram

$$\Delta d = \hat{n} \cdot (\vec{r}_2 - \vec{r}_1) = \hat{n} \cdot \vec{r}_3 = ct_d \tag{1.1}$$

In the equation above, c is the speed of light, $\vec{r}_1$ and $\vec{r}_2$ are the vectors from the origin to each observer, and $\hat{n}$ is the normalized direction vector towards the source. The differenced position vector that points from Earth to the spacecraft observer is represented with $\vec{r}_3$. With successive iterations of this timing comparison,

www.manaraa.com

one can estimate the range between the two observers based on light time delay. With nominally three or more X-ray sources, one could estimate this range in three dimensions.

The previous description shows that XNAV can be performed with one source and two observers. It is generalized for a relative navigation problem. This thesis is focused on an absolute navigation problem, so some simplifications can be made. First, the two observers are located at the spacecraft and at the geocenter. The spacecraft's state ($\vec{x}$) is defined in relation to the geocenter [23]. While ground systems could provide geocenter observations of the photon wave front to the spacecraft, the spacecraft can also hold polynomial coefficients that model the expected photon arrival time at the geocenter. In this way, the spacecraft can perform autonomous on board absolute navigation. Second, the source must emit energy that is bright enough for a hardware detector and have predictable timing behavior. The source used in this thesis are X-rays from an MSP. A dense neutron star with a rotation period on the order of milliseconds, an MSP demonstrates an incredibly stable long term clock of X-ray photon emissions that are comparable to atomic clocks [29]. These sources are appropriate for autonomous on board absolute navigation. In summary, Figure 1.2 provides a more formal representation of pulsar XNAV.

www.manaraa.com

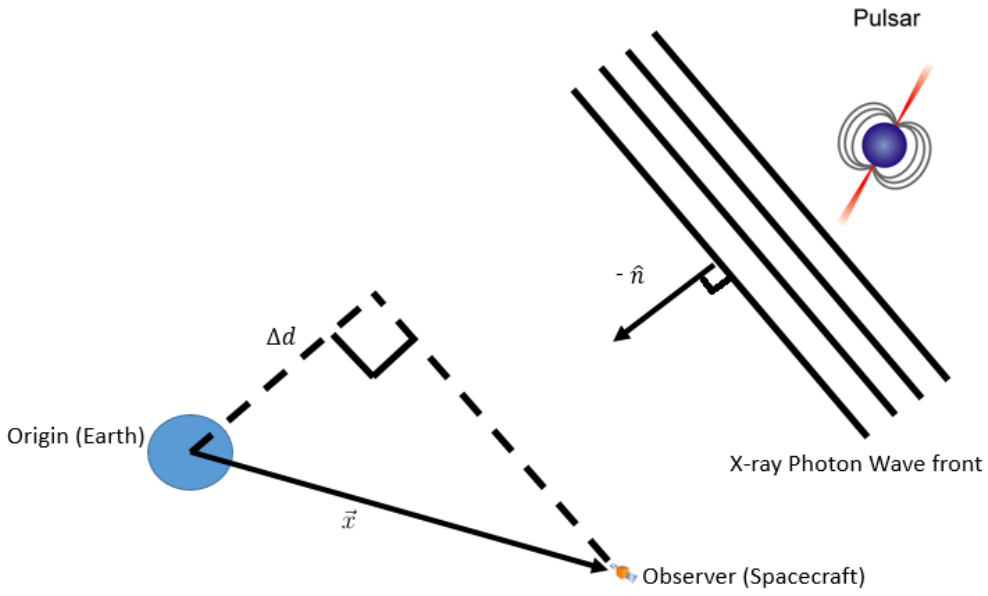

Figure 1.2: Pulsar XNAV Diagram

1.3 Previous Research

The initial discovery of pulsars was in 1967 by Bell and Hewish. The proposal of pulsars providing clock and timing information for Earth-based systems came from Reichley, Downs and Morris at the Jet Propulsion Laboratory (JPL) in 1971 [45]. Pulsars have been continuously studied for their timing accuracy and their relative comparison with atomic clocks. Hartnett and Luiten's 2011 study is an example of current research in the area [29]. With its timing information, pulsars were considered as a potential navigation source. In 1974, Downs proposed a navigation technique using pulsar radio signals [20]. With the discovery of X-ray emissions from pulsars in the 1970s, in 1981 Chester and Butman proposed using X-ray pulsars instead to support navigation systems [13]. The initial proposal of light time delay as a measurement of navigation range was made at this time. In

www.manaraa.com

1988, Wallace recognized the potential challenges of using radio signals from pulsars due to the Signal-to-Noise Ratio (SNR). The required dish size for an appropriate SNR would also be impractical for spacecraft system design [52]. In 1993, Wood proposed a comprehensive system for X-ray navigation as part of the Advanced Research and Global Observation Satellite (ARGOS) Naval Research Laboratory (NRL) mission [55]. Hanson continued this work within spacecraft attitude determination as part of his dissertation at Stanford, using data from the HEAO-A1 spacecraft [27]. Sheikh demonstrated the earliest X-ray pulsar measurement models that could be used with a navigation filter such as an Extended Kalman Filter (EKF) or in a batch least squares solution [46] at the University of Maryland at College Park (UMCP). This was also a part of what was called the XNAV research program, directed by Defense Advanced Research Projects Agency (DARPA). Emadzadeh expanded these X-ray measurement models for use in relative spacecraft navigation by studying signal processing techniques needed to time tag photons in real time [22] [23]. Applications of XNAV were studied to supplement GPS [56] by Woodfork in 2005 and DSN [53] by Winternitz in 2013.

1.4 Thesis Goal

The thesis describes a simulation that creates measurements and applies them to a navigation state estimate. It uses a stochastic model to detect X-ray photon arrival times from a pulsar source. With enough arrival times from a pulsar source, the time offset between the spacecraft arrival times and Earth arrival times is cal-

www.manaraa.com

culated. This information is used to create a measurement. The thesis does not use outside references other than pulsar parameters. The thesis does set up the scenario to replicate the X-ray hardware detector, rather than using a direct measurement model for the navigation filter.

The NASA NICER/SEXTANT hardware is simulated in this thesis. The NICER/SEXTANT mission on the ISS will be in a LEO orbit, seen in Figure 1.3. The orbit is in an Earth Centered Inertial Frame called the MJ2000 frame. Any geographic representations of Earth will be with the MJ2000 frame. The frame is described in chapter 2. The X, Y and Z axes are the Cartesian axes in kilometers. The orbit is in blue and the dotted black lines represent the Earth. Finally, the black line going through the Earth is the Earth magnetic axis.

www.manaraa.com

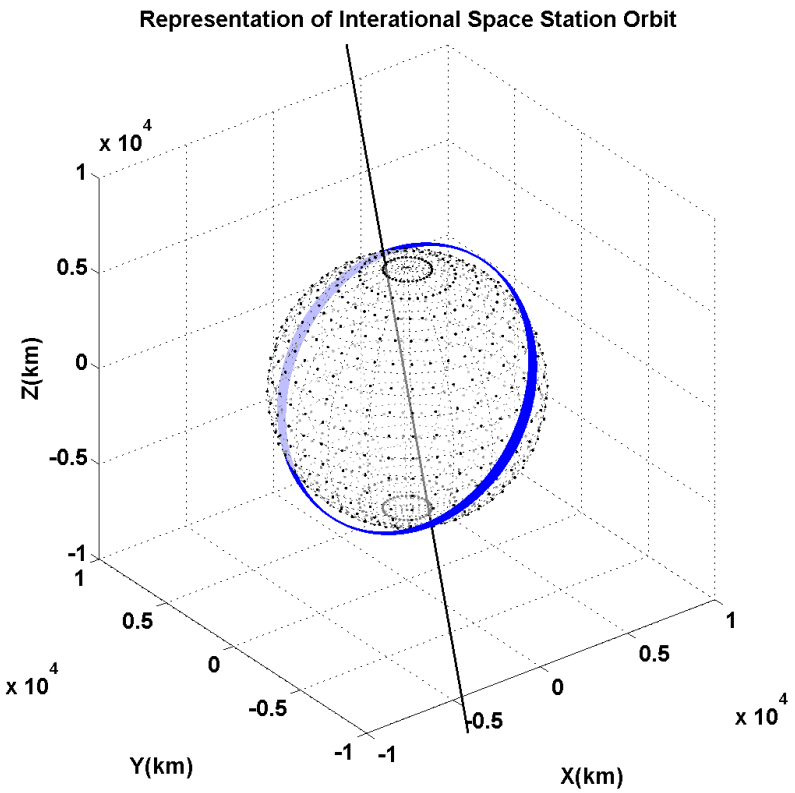

Figure 1.3: Example ISS LEO

The thesis explores the use of XNAV to a general trade space of bounded Earth orbits. A graphical representation of the trade space can be seen in Figure 1.4. Each color represents a different degree of freedom used to explore the bounded orbit trade space.

www.manaraa.com

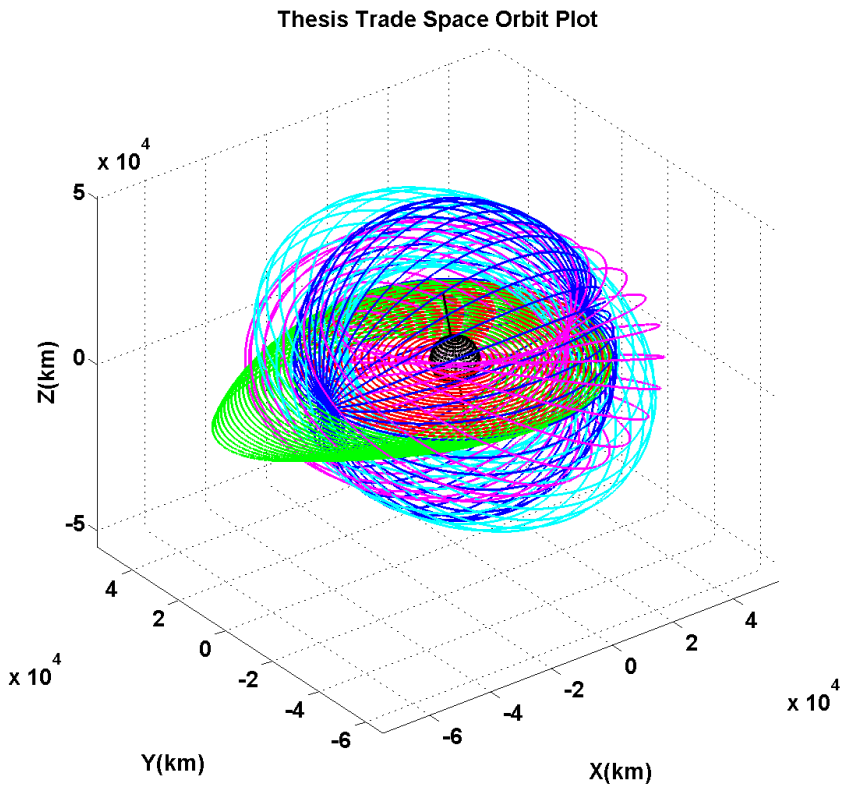

Figure 1.4: Thesis orbit design trade space

The thesis is an extension of previous research by characterizing XNAV for tracking general bounded Earth orbits. Contributions include a model of Earth background radiation as well as a novel pulsar observation scheduling algorithm. Both were created to accommodate for a general bounded Earth orbit. These models help to evaluate the application of XNAV with similar orbit regimes.

The goal is to describe how the initial conditions of an orbit influence tracking performance. Previous research describes tracking for a LEO or a Geosynchronous Earth Orbit (GEO). This thesis describes an extension of that knowledge to the

www.manaraa.com

general family of bounded orbits. That goal is achieved by looking at the coupled behavior that each initial orbit state condition had on the final tracking performance. An overall perception on XNAV implementation is discovered for bounded natural Earth orbits.

1.5 Thesis Overview

Chapter 1 introduces the motivation and concept of XNAV. It enumerates the previous academic research within the field which has lead up to the writing of this thesis. It also provides a summary and its contributions to the research of XNAV.

Chapter 2 details the concepts of astrodynamics and space navigation used in this thesis. The chapter summarizes the dynamics models used in the propagation of the spacecraft as well as the filter used to estimate the propagation of the spacecraft. The chapter also summarizes the coordinate frames and terminology used in the evaluation of XNAV. Finally, the chapter concludes by providing the parameters that are used in this thesis for spacecraft truth ephemeris generation and spacecraft state estimation.

Chapter 3 details the X-ray pulsar sources used in this thesis. An overview of pulsars as neutron stars is given, as well as the properties that help define pulsars as timing models for XNAV. A catalog of potential pulsar targets is provided and a subset of that catalog used for this thesis is presented.

Chapter 4 details the development of XNAV hardware and experimentation. An introduction is made to two current experiments called the NICER science in-

www.manaraa.com

strument and SEXTANT, a XNAV technology demonstration that is used on the NICER instrument. Finally, the chapter details the hardware properties and assumed parameters of NICER used in the thesis.

Chapter 5 details the use and significant modification of the SEXTANT simulation to apply XNAV for the study of bounded Earth orbits. The chapter describes the phase estimation model based on the simulated arrival times of X-ray photons. It also presents the tested trade space of bounded orbits as well as the visibility, scheduling, and background radiation environment models used for the orbit trade space.

Chapter 6 details tracking performance with a five Degree of Freedom (DOF) orbit design trade space. The first study tests the sensitivity of varying one DOF for each DOF. A second study fixes one DOF and tests the sensitivity of varying the other DOF.

Finally, chapter 7 summarizes results, presents future work, and provides final comments.

www.manaraa.com

Chapter 2: Astrodynamics and Space Navigation

This chapter details the astrodynamics and navigation concepts used throughout this thesis. The information provided here come from various sources on astrodynamics and space navigation [5] [49] [17] [48]. This information is to provide technical context to the thesis and it is all referenced academic research.

The coordinate reference frames are first listed and described. Afterwards, the force models and orbit parameters are described. The following process is repeated for the navigation filter design. Finally, the chapter concludes with a summary of the thesis's specific formulation of orbit design and navigation filter.

This chapter as a whole uses various notations which are specific to navigation and orbit design. Similar variables are used in the astronomy section of this thesis. Context will be provided before using the appropriate set of variables and notations for the rest of this thesis. For general reference, $\vec{x}$ is the spacecraft state vector, $\vec{v}$ is the spacecraft velocity vector, and $\vec{a}$ is the spacecraft acceleration vector. Subscripts will indicate the reference frame and superscripts will provide further information. Finally, vectors are assumed to be column vectors and bold vectors are used to denote matrices.

www.manaraa.com

2.1 Coordinate Reference Frames

In order to properly describe dynamical systems for space flight dynamics and navigation, a suite of coordinate frames are required.

2.1.1 Body Centered Inertial Frame

The Body-Centered Inertial (BCI) frame denotes a Cartesian space around a given planetary body. The origin of the frame is at the center of that body with three orthogonal unit vectors. All unit vectors are denoted with a hat accent. This thesis uses a subset of the BCI frame called the Earth Centered Inertial (ECI) frame, which is a BCI frame with an origin at the Earth's geocenter. The $\hat{I}$ axis vector is in the direction of the celestial first point of Aries which is also the direction of the vernal equinox. The $\hat{K}$ axis vector is through the Earth north pole. The $\hat{J}$ axis makes the right hand orthogonal complement of these two vectors. See Figure 2.1 for a graphical representation of ECI.

Finally, a subset of the ECI frame is the MJ2000 frame. The MJ2000 frame is the frame used in this thesis when referencing ECI. A visual representation can be seen in Figure 2.2. The MJ2000 frame is the ECI frame oriented to the modified Julian date epoch of January 1st, 2000 [49]. Though the $\hat{K}$ vector is traditionally defined as the Earth north pole, the MJ2000 frame has the $\hat{K}$ vector pointed in the celestial north pole direction instead. The celestial north pole is the axis of nutation that the Earth's spin axis processes around. This frame will be specified with just the subscript (ex. $\vec{X}_E$). Another term is the True of Date (TOD), which is the ECI

www.manaraa.com

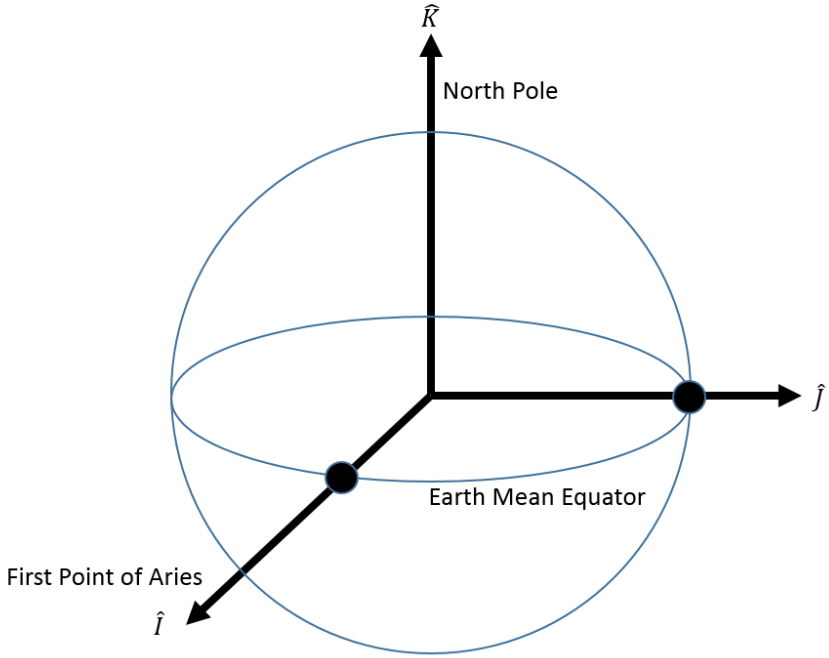

Figure 2.1: Graphical Representation of the ECI frame

frame which is adjusted to the specific epoch when the vectors are defined [49]. This frame will be specified with a subscript ($\vec{x}_{TOD}$).

2.1.2 Earth Centered Earth Fixed Frame

The ECEF frame aligns with the polar motion due to the offset of the Earth's principal moment of inertial and its instantaneous axis of rotation. At a given epoch, the $\hat{K}_{ECEF}$ axis vector is the adopted geographic pole that is aligned with the North pole at a given epoch. The $\hat{I}_{ECEF}$ axis vector points at the intersection of the Greenwich Meridian and the Earth's equator, also called the Prime Meridian. The $\hat{J}_{ECEF}$ frame is the right hand orthogonal complement to these vectors. See Figure 2.3 for a graphical representation.

www.manaraa.com

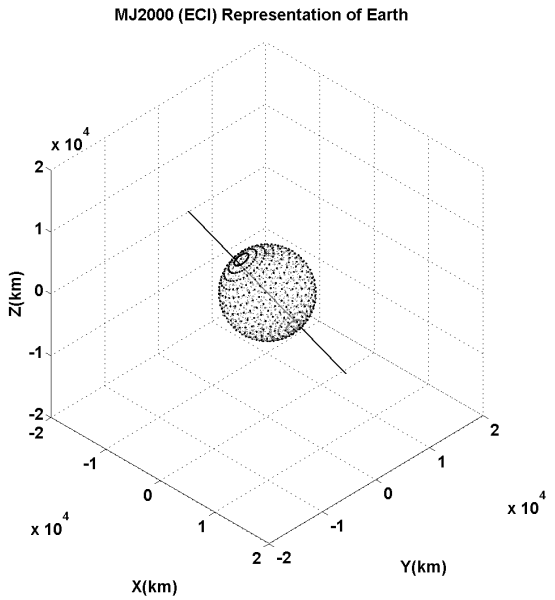

Figure 2.2: Graphical Representation of the MJ2000 frame, a variant of an ECI frame.

2.1.3 Geodetic/Geocentric Longitude and Latitude

Longitude and latitude map a location around the Earth ellipsoid using two spherical angles. Longitude is an east-west angular displacement with a 0°point at the prime meridian and a negative notation in the western direction. It has a range between [-180,180]. Latitude is the north-south angular displacement with a 0°point at the equator and a negative notation in the southern direction. It has a range between [-90,90].

There are two forms of latitude: geodetic and geocentric. These are two conventions based on the location on Earth's surface and an Earth centered origin respectively. Geocentric latitude is the angle between a vector from the Earth geocenter to the Earth equator and a vector from the center of the Earth to the

www.manaraa.com

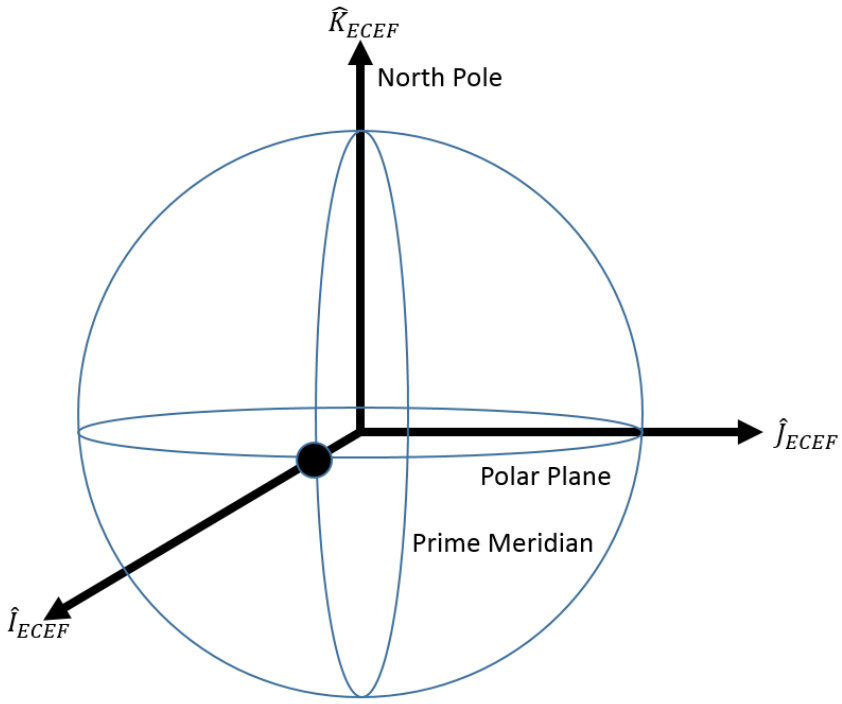

Figure 2.3: Graphical Representation of the ECEF frame

spacecraft, making the Earth center the angle vertex. Geodetic latitude is an angle measured between a vector on the equatorial plane and a second vector that is perpendicular to the Earth surface. Its vertex is not at the Earth Center. See Figure 2.4 for a visual description. For future reference, ϕ_{gd} and ϕ_{gc} will indicate geodetic and geocentric latitude respectively. Longitude will also use the subscript, though the values for the angle are all equal. Finally, note that the reference ellipsoid used in this thesis for these angle definitions is the WGS-84 model [56].

2.1.4 Radial-Intrack-Crosstrack Spacecraft Coordinate Frame (RIC)

To effectively identify forces and any other dynamical behavior local to the spacecraft, a local body frame reference is required. Also known by a variety of

www.manaraa.com

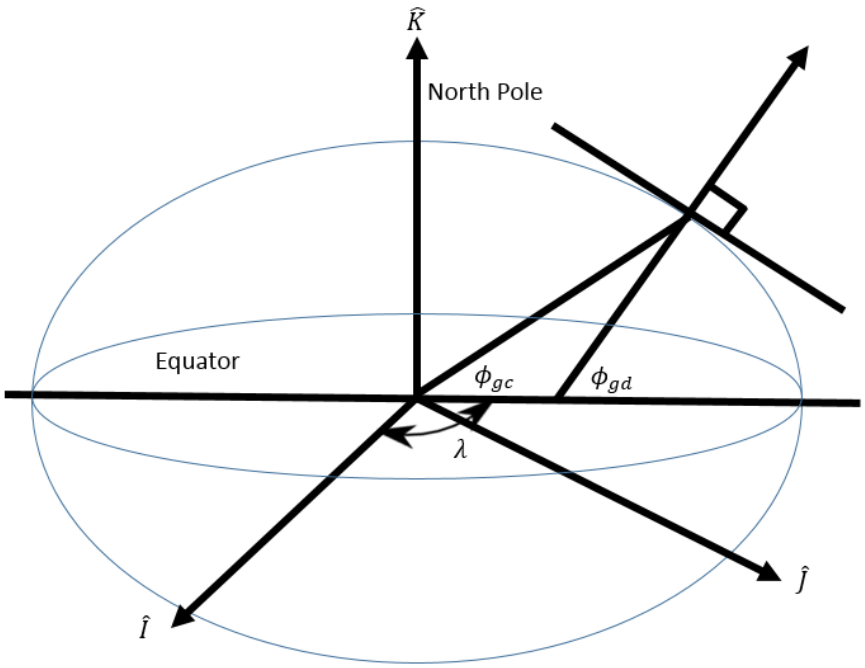

Figure 2.4: Graphical Representation of Geodetic(ϕ_{gd})/Geocentric(ϕ_{gc}) latitude and longitude(λ)

other conventions such as the RSW frame or the Radial, Along-track, Cross-track frame [56], the RIC frame is an orthogonal body fixed frame with its origin at the center of mass of the spacecraft. A graphical representation can be seen in Figure 2.5 using RSW notation.

The instantaneous position vector of the spacecraft $\hat{R} = \hat{I}_{RIC}$ of the RIC frame, the instantaneous angular momentum vector $\hat{W} = \hat{K}_{RIC}$ in the RIC frame and the orthogonal cross product $\hat{S} = \hat{J}_{RIC}$ in the RIC frame. Note that this frame is based off the physical vectors of spacecraft's angular momentum and position vector. The velocity vector is not aligned with the $\hat{I}_{RIC}$ except at the perigee and apogee of an orbit. However with a circular orbit, the $\hat{I}_{RIC}$ vector will align with the velocity

www.manaraa.com

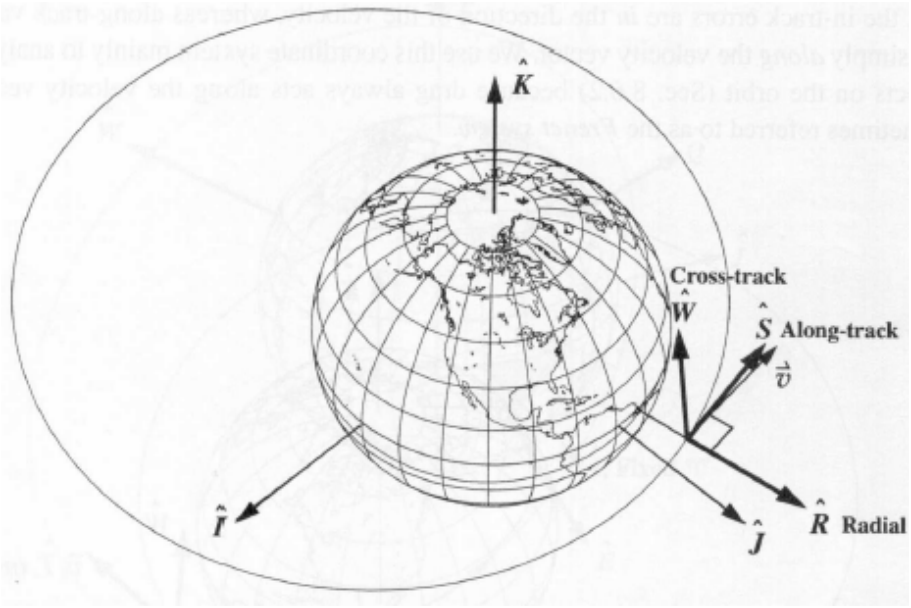

Figure 2.5: Graphical Representation of the RIC frame [49]

vector at all times.

2.1.5 Celestial Coordinate Systems

To make references to celestial bodies that are assumed to be fixed in the ECI, two spherical angles are sufficient to describe the direction of that object to the observer. Two commonly used systems are called the equatorial and ecliptic celestial coordinate frames. See Figure 2.6 for a graphical representation of the two spherical angles. The equatorial frame uses the Earth celestial equator and the ecliptic uses the Earth orbit ecliptic as the plane for defining right ascension.

www.manaraa.com

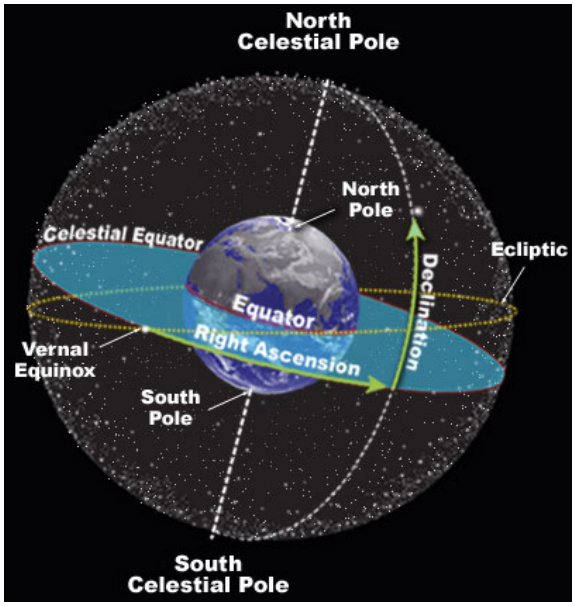

Figure 2.6: Graphical Representation of the Celestial Sphere [47]

2.2 Astrodynamics Background

This section reviews the force models used in this thesis. It uses two body motion (Newton's law of universal gravitation) and non-spherical gravity acceleration terms.

$$\vec{F}_{ext} = \vec{F}_{Earth} + \vec{F}_{Geopot} \tag{2.1}$$

When normalized by the spacecraft mass, the spacecraft acceleration is revealed, which can be integrated to numerically calculate position and velocity of the spacecraft over time:

$$\vec{a} = \vec{a}_{Earth} + \vec{a}_{Geopot} \tag{2.2}$$

The following sections state each acceleration term used in the thesis. The

www.manaraa.com

information is referenced from multiple sources [5] [49] [17].

2.2.1 Newton's Law of Universal Gravitation

Newtonian dynamics of space flight extends from the application of Newton's second law of motion for a spacecraft in orbit. Consider an ECI frame which includes a satellite of mass m which defined in space by a position vector $\vec{x}_E$ in the ECI frame. The origin of the ECI frame is Earth with mass M_E, a mass significantly greater than spacecraft mass m. The velocity of the spacecraft is denoted as $\vec{v}_E$ and its acceleration as $\vec{a}_E$ in the ECI frame. See Figure 2.7 for a graphical representation. Note that a vector magnitude of a spacecraft's position is called the spacecraft radius, or r. Also, the term spacecraft Earth altitude is defined as spacecraft height from the Earth's surface, equal to the difference of the spacecraft radius and the Earth's hard body radius.

Newton's second law of motion is defined as follows:

$$\frac{d}{dt}(m\vec{v}_E) = \vec{F}_{ext} \tag{2.3}$$

With F_{ext} denoting any external forces acting on the spacecraft. A variety of forces act on a spacecraft with varying degrees of complexity, but the most fundamental acting force in this regime comes from Newton's Law of Universal Gravitation. Assuming point masses, the force $\vec{F}_{Earth}$ that drives the spacecraft's

www.manaraa.com

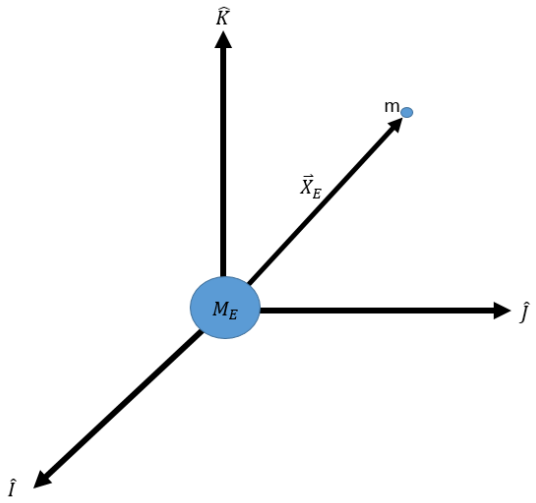

Figure 2.7: Diagram of spacecraft vector in the ECI frame

acceleration is defined below:

$$\vec{F}_{Earth} = -\frac{GM_E m}{||\vec{x}_E||^2}\vec{x}_E = -\frac{\mu m}{r^2}\hat{x}_E \tag{2.4}$$

The constant G is called the gravitational constant with a value of $6.67408 * 10^{-11} m^3 kg^{-1} s^{-2}$ while μ is called the standard gravitational parameter, specific for each central body.

And when both sides of the equation are normalized by spacecraft mass, the acceleration term is:

$$\vec{a}_{Earth} = -\frac{\mu}{r^2}\hat{x}_E \tag{2.5}$$

www.manaraa.com

2.2.2 Non-Spherical Gravity

The model of Earth forces used in this thesis are based on an ellipsoid shaped Earth. These higher order gravitational forces are a conservative potential. They are driven only by the position of the spacecraft relative to Earth. The derivation requires a formal subdivision of the ellipsoid into harmonic coefficients. This results in a potentially infinite sum of corrective gravitational terms. Full derivations are provided in detail from multiple sources [49] [32] [36]. The acceleration due to the geopotential used in this thesis is defined in the ECI True of Date frame. To define this acceleration, the potential equation is provided first in Equation (2.6).

$$U_{Geopot} =$$

$$U_{Geopotential}(r, \phi_{gc}, \lambda_{gc}) = \frac{\mu}{r} \sum_{n=2}^{N} {C_n}^0 (\frac{R_{Earth}}{r})^n {P_n}^0 (sin(\phi_{gc})) +$$

$$\frac{\mu}{r} \sum_{n=2}^{N} \sum_{m=1}^{n} (\frac{R_{Earth}}{r})^n {P_n}^m (sin(\phi_{gc}) [{S_n}^m sin(m\lambda_{gc}) + {C_n}^m cos(m\lambda_{gc})] \quad (2.6)$$

where

r = magnitude of the vector from the Earth's center of mass to the satellite

ϕ_{gc} = geocentric latitude

λ_{gc} = geocentric longitude

μ = standard gravitational parameter of Earth $(398600.4415 * 10^9 m^3/s^2)$

R_{Earth} = equatorial radius of the Earth $(6378000m)$

www.manaraa.com

N = maximum degree included in the expansion

${P_n}^m(sin(\phi_{gc}))$ = associated Legendre function

$S_{nE}^{\ m}, C_{nE}^{\ m}$ = harmonic coefficients for the Earth

With the variable N, one can set the higher order gravity potential terms used in the spacecraft force model. For example, the first and second harmonics terms ($N = 2$) form the nonspherical potential due to the sum of zonal and tesseral harmonics. It is also called the J_2 perturbation [36].

The acceleration due to the geopotential is defined in the ECI True of Date frame:

$$\begin{aligned}\vec{a}_{Geopot} &= \left(\ddot{X}_{Geopot}, \ddot{Y}_{Geopot}, \ddot{Z}_{Geopot}\right)^T \\ &= \left(\frac{\delta U_{Geopot}}{\delta r}(\frac{\delta r}{\delta \vec{r}_{TOD}})^T + \frac{\delta U_{Geopot}}{\delta \phi_{gc}}(\frac{\delta \phi_{gc}}{\delta \vec{r}_{TOD}})^T + \frac{\delta U_{Geopot}}{\delta \lambda_{gc}}(\frac{\delta \lambda_{gc}}{\delta \vec{x}_{TOD}})^T\right) \quad (2.7)\end{aligned}$$

The following defines the ECI True of Date components $\vec{x}_{TOD} = (x_{TOD}, y_{TOD}, z_{TOD})$ [49]:

$$\ddot{X}_{Geopot} = \left(\frac{1}{r}\frac{\delta U_{Geopot}}{\delta r}\frac{z_{TOD}}{r^2\sqrt{x_{TOD}^2 + y_{TOD}^2}}\frac{\delta U_{Geopot}}{\delta \phi_{gc}}\right)x_{TOD} - \left(\frac{1}{x_{TOD}^2 + y_{TOD}^2}\frac{U_{Geopot}}{\delta \lambda_{gc}}\right)y_{TOD} \quad (2.8)$$

$$\ddot{Y}_{Geopot} = \left(\frac{1}{r}\frac{\delta U_{Geopot}}{\delta r}\frac{z_{TOD}}{r^2\sqrt{x_{TOD}^2 + y_{TOD}^2}}\frac{\delta U_{Geopot}}{\delta \phi_{gc}}\right)y_{TOD} - \left(\frac{1}{x_{TOD}^2 + y_{TOD}^2}\frac{U_{Geopot}}{\delta \lambda_{gc}}\right)x_{TOD} \quad (2.9)$$

$$\ddot{Z}_{Geopot} = \left(\frac{1}{r}\frac{\delta U_{Geopot}}{\delta r}\right)z_{TOD} + \frac{\sqrt{x_{TOD}^2 + y_{TOD}^2}}{r^2}\frac{\delta U_{Geopot}}{\delta \phi_{gc}} \quad (2.10)$$

www.manaraa.com

2.2.3 Kepler's Orbital Elements

It is well known that planetary orbits are shaped like conic sections [5] [49]. This suggests that a different change of coordinates can reveal more about an orbit. Kepler elements represent an orbit as a conic section in 3-D space. There are six Kepler elements. Three describe the orbit within a 2-D plane. The other three are Euler angle rotations that rotate the 2-D orbit plane within a 3-D space.

Given a known Cartesian state of $\vec{x}_E$ and $\vec{v}_E$ in the ECI frame and the following assumptions:

- Only applying Newton's gravitation force.
- A two body orbit, where one body's point mass is much greater than the other point mass.

Two properties of a spacecraft orbit are then conserved: energy and angular momentum [49]. This conservation allows Kepler's orbital elements to fully define a spacecraft orbit.

The three parameters that define a conic section in the orbit plane are called eccentricity (ECC), semi-major axis (SMA), and true anomaly (True Anomaly (TA)).

The ECC value e is the magnitude of the eccentricity vector, an integration constant that comes from relating the spacecraft acceleration and angular momentum:

$$\vec{e} = \frac{\vec{v}_E \times \vec{h}_E}{\mu} - \frac{\vec{x}_E}{r} \tag{2.11}$$

www.manaraa.com

The SMA value of a then has a fundamental relationship with specific orbital energy with one form of the vis-viva equation. It is an equation of the total specific energy of the orbit, given the assumptions.

$$\frac{-\mu}{2a} = \frac{1}{2}v^2 - \frac{\mu}{r} \tag{2.12}$$

Where $v = ||\vec{v}_E||$.

This form of the vis-viva equation defines the total orbit specific energy. It also separates Cartesian elements and Kepler elements. The Cartesian elements show that the total orbit energy is the sum of the spacecraft kinetic energy $\frac{1}{2}v^2$ and potential energy $-\frac{\mu}{r}$. With Kepler elements, only the SMA element is required to define orbit energy $(-\frac{\mu}{2a})$.

In this form, SMA is a constant value of specific orbital energy. Due to this particular property, it is often used to determine first order stability in orbit determination when the dynamics force model is dominated by conservative forces [10].

Another important orbit property that is derived from SMA is the orbital period(T). This is the time required for a satellite to travel one full revolution around a central body. With the previously stated assumptions of two body motion around a large central body as well as Kepler's third law, this relationship is:

$$T = 2\pi\sqrt{\frac{a^3}{\mu}} \tag{2.13}$$

Another Kepler element required in order to define a spacecraft along an orbit is the TA. It is an angle defined from the $\vec{e}$ vector in the orbit plane that is swept

www.manaraa.com

out by the arrow, denoted usually by the term υ.

Once the geometric orbital elements are defined, the other orbital elements place the orbit plane into the 3-D space. See Figure 2.8. Note that the inertial frame in this figure is equivalent to the previously defined vector: $(\vec{I}, \vec{J}, \vec{K}) = (\hat{X}_E, \hat{Y}_E, \hat{Z}_E)$. Also, the angular momentum vector $\vec{h}_E = \vec{h}$.

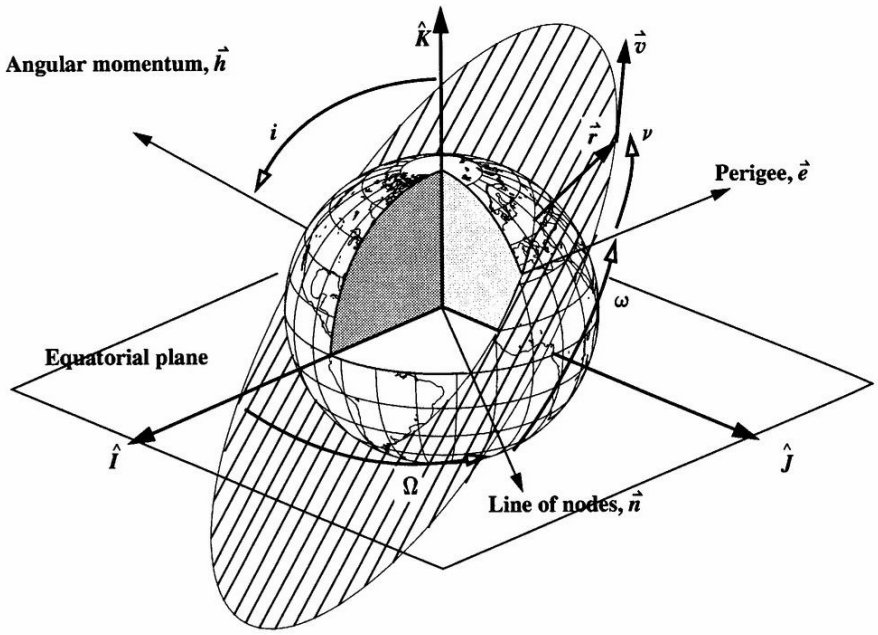

Figure 2.8: Graphical Representation of orbit angles [49]

As seen in Figure 2.8, the orbit plane is rotated into the 3-D space by three Euler rotation angles:

1. INC(i): The angle between the angular momentum vector $\vec{h}_E$ and the positive inertial vector $\hat{Z}_E$.

2. AOP(ω): The angle between the node vector $\vec{n}$ in Figure 2.8 and the eccentricity vector $\vec{e}$.

www.manaraa.com

3. RAAN(Ω): The angle between the node vector $\vec{n}$ in Figure 2.8 and the positive inertial vector $\hat{X}_E$.

These three Euler angles have locations where the angle is undefined. If the orbit is circular (where ECC = 0), the AOP angle is undefined as the eccentricity vector is undefined. If the orbit is equatorial, the orbit RAAN is undefined as the node vector is undefined. In these cases, the orbit value for AOP and RAAN are set to 0, respectively. Other orbit parameter definitions for these special cases are stated explicitly in the General Mission Analysis Tool (GMAT) math specification document. The tool was used to generate spacecraft ephemeris [32].

Together, these six terms terms fully define a spacecraft orbit in three dimensional space.

2.2.4 Perturbations

This thesis uses non-spherical gravity terms in its force model. This changes the behavior of Kepler elements significantly, as it must now vary based on changing Earth forces. This section describes that rate of change, as it has an influence on the thesis results. This section is further detailed in reference [17].

Kepler's orbital elements are created with the assumption of two body motion. The addition of higher order non-spherical gravity causes the elements to vary over time. Most of the major influences of non-spherical gravity come from the first two orders of the gravitational potential equation (so using Equation (2.6) with N = 2). This influence is called the J_2 perturbation.

www.manaraa.com

These equations include a constant called J_2 which encapsulates second order gravitational harmonics. For Earth, that constant value of $J_2 = 1.08263 \times 10^{-3}$. The primary influence of the J_2 perturbation causes RAAN and AOP to precess over time [5] [17]. This can be summarized with the following two equations:

$$\dot{\Omega} = -\left(\frac{3}{2}\frac{\sqrt{\mu}J_2R_{Earth}^2}{(1-e^2)^2a^{\frac{7}{2}}}\right)cos(i) \tag{2.14}$$

$$\dot{\omega} = -\left(\frac{3}{2}\frac{\sqrt{\mu}J_2R_{Earth}^2}{(1-e^2)^2a^{\frac{7}{2}}}\right)\left(\frac{5}{2}sin^2(i) - 2\right) \tag{2.15}$$

Defined earlier, R_{Earth} is the hard body radius of the Earth, J_2 is the J_2 perturbation constant for Earth, and μ is the standard gravitation parameter. As is seen here, the secular precession of these two rotation angles are a result of SMA, ECC, and INC. The following figures show the influence of these three orbital elements on the two rotation angles.

www.manaraa.com

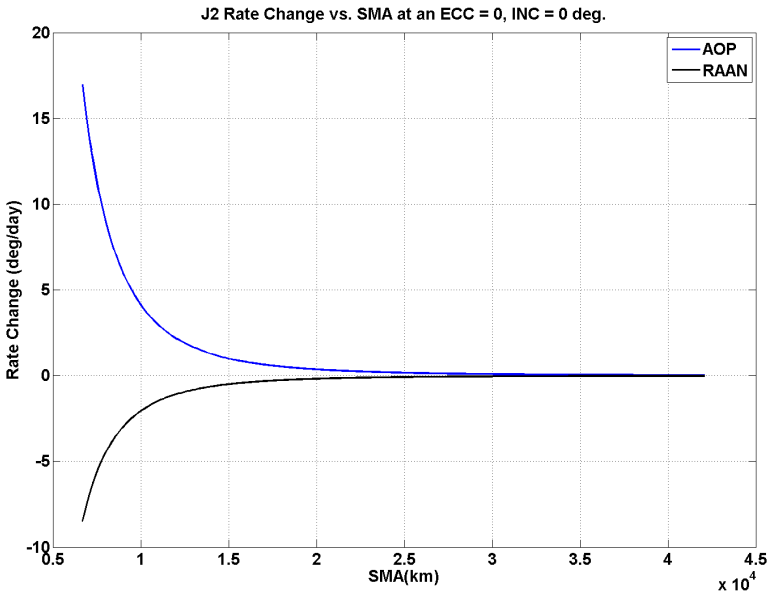

Figure 2.9: AOP and RAAN rate of change versus SMA due to J_2

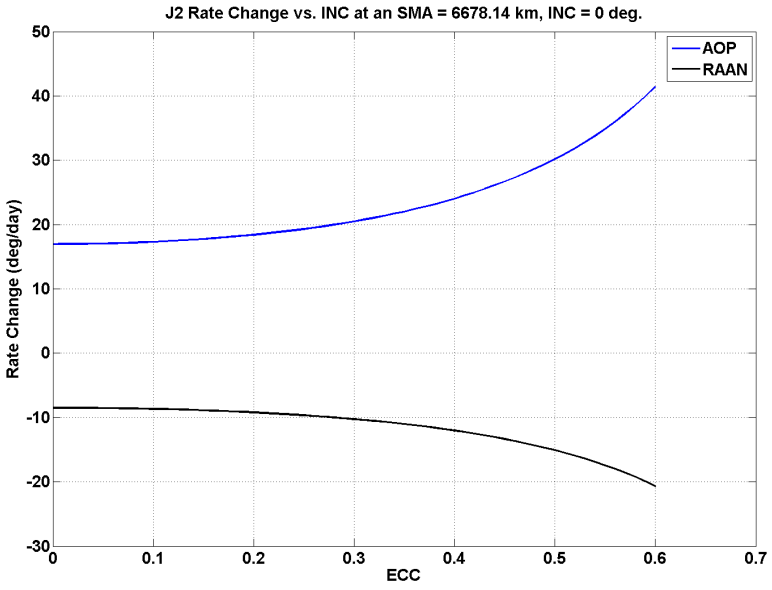

Figure 2.10: AOP and RAAN rate of change versus ECC due to J_2

www.manaraa.com

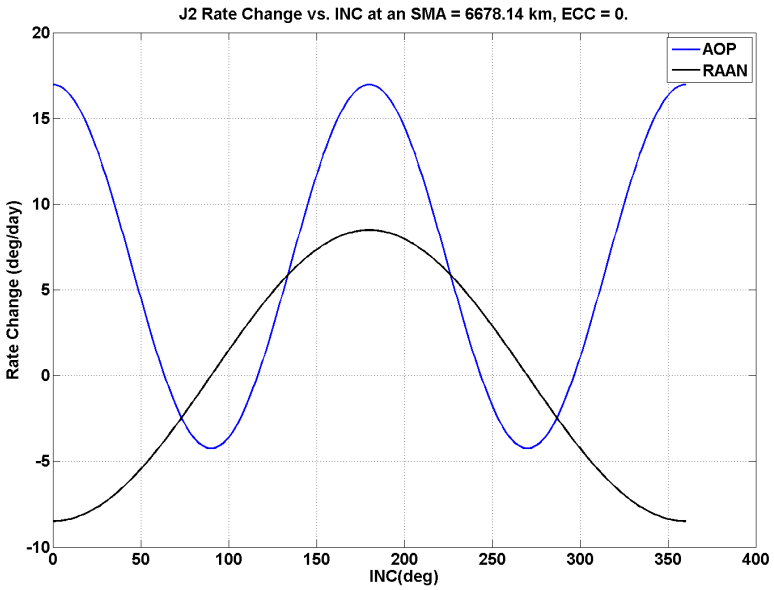

Figure 2.11: AOP and RAAN rate of change versus INC due to J_2

For Figure 2.9, 2.10, and 2.11, the horizontal axis in each is the range of the thesis orbit trade space in kilometers or degrees respectively. The vertical axis on all three figures is the rate change for both AOP and RAAN in degrees per day. A positive angle rate of change means that the orbit node vector will drift eastward. A negative angle rate of change means that the node vector will drift westward. As seen, an orbit with a low value of SMA and INC result in a higher rate of change for the two rotation angles. The maximum magnitude is 20°. For ECC, the increase of ECC causes the rate change to have a greater magnitude, with a 40°maximum.

2.3 Space Navigation Background

Space navigation rectifies the difference between ideal dynamics models and physical reality by estimating the spacecraft state over time. This state estimate

www.manaraa.com

is supplemented with observations influenced by the physical reality of random and systematic errors. See Figure 2.12 for a graphic representation of the process.

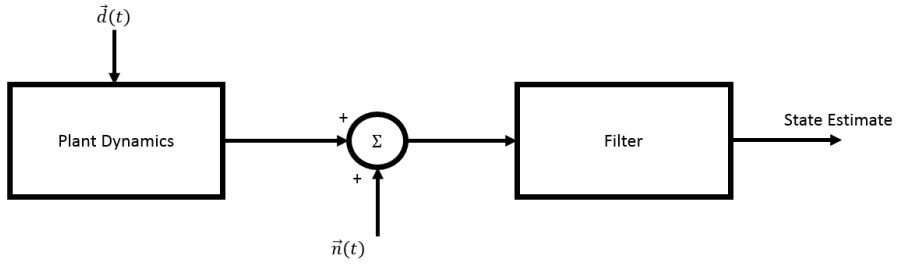

Figure 2.12: State Estimation Flow Diagram

State estimation is a process that utilizes measurement inputs to provide an estimate of the output state. The plant dynamics will have external disturbances $\vec{d}(t)$ and the measurements of the output of plant dynamics will have noise $\vec{n}(t)$. The filter must be robust to these stochastic influences and provide an estimate state. There is no direct feedback control on the dynamics with space navigation. However, this thesis uses an EKF to estimate the spacecraft state. The basis of the EKF comes from the Kalman Filter, most commonly described in a feedback loop [7].

2.3.1 Kalman Filter

The Kalman filter is an algorithm that uses measurements with statistical noise to estimate unknown variables. It is traditionally posed as a feedback loop similar to the one seen in Figure 2.13. The Kalman filter is a linear optimization that assumes Gaussian stochastic noise. Further details into the derivations in this section are contained in various references on spacecraft navigation and control theory [48] [7].

www.manaraa.com

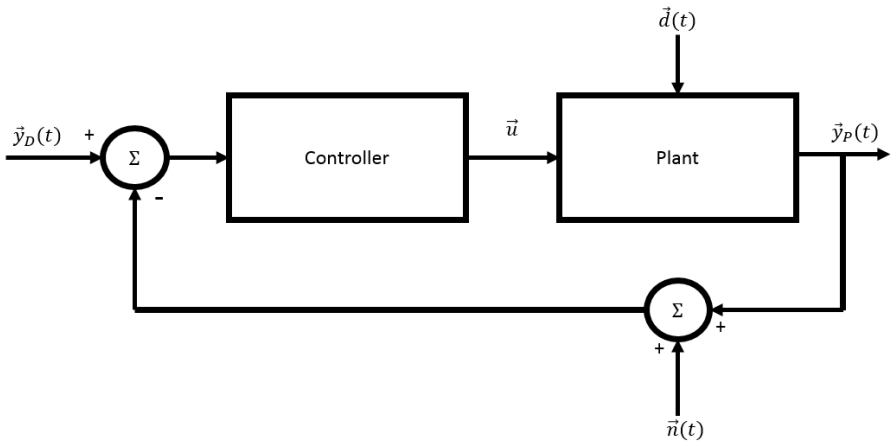

Figure 2.13: Single Loop Feedback Control Loop

Seen in Figure 2.13, a single loop feedback control law represents a relationship between the plant and the controller. The plant is the block that represents the physical behavior of the system. The controller represents the hardware and models created by the user to work with the plant. A desired output $\vec{y}_D(t)$ of the plant dynamics is entered by the user and directed to the controller. This controller takes the desired output and creates the required inputs $\vec{u}$ to pass to the plant. The plant output of $\vec{y}_P(t)$ is measured and returned as feedback measurements into the controller. Disturbances $\vec{d}(t)$ and noise from the feedback of measurements $\vec{n}(t)$ are stochastic representations of model offset. They represent external influences to the system.

The ideal objective for navigation tracking is to provide a controller that can give unbiased minimum variance tracking between the desired output $\vec{y}_D(t)$ and the actual output $\vec{y}_P(t)$. Equation (2.18) is an analytical representation of the cost

www.manaraa.com

function.

$$\vec{e}(t) = \vec{y}_D(t) - \vec{y}_P(t) \tag{2.16}$$

$$E[\vec{e}(t)] = 0 \tag{2.17}$$

$$E[\vec{e}(t)^T \vec{e}(t)] = trace[\Sigma_{ee}(t)] \tag{2.18}$$

Moving this concept towards space navigation, consider the spacecraft state $\vec{x}$ that is being estimated by a state $\hat{\vec{x}}$. The same minimization is desired in reducing the offset of the state estimate to the actual state vector. The estimation process uses measurements $\vec{y}$ in a feedback control loop as defined below. Note that the frame for these states is generalized but it must be consistent.

$$\vec{e}(t) = \vec{x}(t) - \hat{\vec{x}}(t) \tag{2.19}$$

$$\vec{y}(t) = \mathbf{H}(t)\hat{\vec{x}}(t) + \vec{n}(t) \tag{2.20}$$

$\mathbf{H}(t)$ is the measurement matrix used to innovate the state with a linear transformation of the current estimate of the state.

To begin solving the orbit determination problem, the following assumptions are made:

1. The system is linearly time invariant.

www.manaraa.com

2. $\hat{x} = E[\vec{x}|\vec{y}]$ is the mean square optimal prediction [7].

3. The linear prediction above is sufficient to assert an optimal solution.

4. All stochastic noise are wide sense stationary white noise processes.

5. Measurement noise and disturbance values are uncorrelated.

The minimization of the offset of the state estimate to the actual state vector at iteration k is presented below. Derivations are elaborated in these sources: [7] [48]. Note that the time dependence is suppressed in the following notation.

First, the measurement noise and disturbances on the state variables can be unified within what are called the measurement noise and process noise matrices. The disturbances (also called process noise) matrix $\mathbf{Q}$ is defined as the expectation of the inner product of the process. The stochastic noise assumption allows these matrices to become constants.

$$\mathbf{Q} = E[\vec{d}\vec{d}^T] = constant \tag{2.21}$$

The measurement noise matrix represents the expectation of the inner product of the measurement noise.

$$\mathbf{R} = E[\vec{n}\vec{n}^T] = constant \tag{2.22}$$

In the state space formulation of this design with the given assumptions, the plant dynamics are a constant matrix $\mathbf{F}$ The state transition matrix is then given by $\Phi_k = e^{\mathbf{F}t_s}$ where t_s is the sampling time of the filter.

www.manaraa.com

The following subsequently is the discrete form of the Kalman filter. The discrete form of the Kalman filter shows an iterative step process between each calculation. The "$-$" superscript indicates the previous iteration within that equation, be it the k^{th} iteration or the $(k-1)^{th}$ iteration.

$$\hat{\vec{x}}_k = \hat{\vec{x}}_k^- + \mathbf{K}_k(\vec{y}_k - \mathbf{H}_k\hat{\vec{x}}_k^-) \tag{2.23}$$

$$\mathbf{K}_k = \mathbf{P}_k^-\mathbf{H}_k^T(\mathbf{H}_k\mathbf{P}_k^-\mathbf{H}_k^T + \mathbf{R}_k]^{-1} \tag{2.24}$$

$$\hat{\vec{x}}_k^- = \mathbf{\Phi}_{k-1}\hat{\vec{x}}_{k-1} \tag{2.25}$$

$$\mathbf{P}_k^- = \mathbf{\Phi}_k\mathbf{P}_{k-1}\mathbf{\Phi}_k^T + \mathbf{Q}_k \tag{2.26}$$

$$\mathbf{P}_{k-1} = [\mathbf{I} - \mathbf{K}_{k-1}\mathbf{H}_{k-1}]\mathbf{P}_{k-1}^- \tag{2.27}$$

$\mathbf{P}$ is the covariance matrix of the state that indicates the filter's statistical knowledge of state estimation convergence. The Kalman gain $\mathbf{K}$ matrix is a set of coefficients that balance between using measurement updates and or the process estimation for each iteration of k. Finally, $\mathbf{I}$ is an identity matrix.

This formulation is commonly called the Kalman filter. It is used as a robust filter that allows different sensors with dynamically changing rates and availability through its H matrix for successive iterations of k. It is the basis for the EKF used in this thesis, though modified specifically for XNAV testing.

www.manaraa.com

On a final note, a common way to represent covariance filter performance is to plot the standard deviation alongside the actual state estimation errors. The value 3σ represents three times the standard deviation of the filter state error. As the actual difference between the truth and estimate state is unknown to the filter, this value represents the current knowledge error that the filter has on the actual error. The spacecraft position vector is a 3x1 vector, so the following defines the σ metric for the position covariance matrix. The same is applied for the velocity vector.

Starting with a representation of the covariance matrix:

$$\mathbf{P} = \begin{bmatrix} P_{11} & P_{12} & P_{13} \\ P_{21} & P_{22} & P_{23} \\ P_{31} & P_{32} & P_{33} \end{bmatrix} \tag{2.28}$$

The diagonal represents the variance estimate of each state element in the filter. Using that diagonal, the σ metric is:

$$\sigma = \sqrt{RSS(diag(P))} \tag{2.29}$$

$$\sigma = \sqrt{(P_{11}^2 + P_{22}^2 + P_{33}^2)^{\frac{1}{2}}} \tag{2.30}$$

This metric will be represented at 3σ, versus time, alongside the actual errors between truth and estimate state. If the filter is performing effectively, this 3σ metric should encompass the actual state errors throughout the entire scenario.

www.manaraa.com

2.3.2 Extended Kalman Filter (EKF)

The Kalman filter, though useful, is an estimator designed for linear system models with a linearly optimal predictor criteria for the estimate state.

The EKF is an extension of the Kalman filter for a nonlinear system model. It linearizes the system about the current estimate state and applies the Kalman filter at that state. Note that the time dependence is suppressed in the following notation.

The dynamics and measurements of the system are now defined as a set of nonlinear differential equations in $\vec{x}$:

$$\dot{\vec{x}} = \mathbf{f}(\vec{x}) + \vec{d}, \tag{2.31}$$

$$\vec{y} = \mathbf{h}(\vec{x}) + \vec{n} \tag{2.32}$$

Where $\mathbf{f}(x)$ and $\mathbf{h}(x)$ represent the nonlinear functions of dynamics and the measurement model based on the state. The system must now linearize about an estimate of the state $\hat{x}$ of these two functions:

$$\mathbf{F} = \left.\frac{\partial \mathbf{f}(\vec{x})}{\partial \vec{x}}\right|_{\vec{x}=\hat{\vec{x}}} \tag{2.33}$$

$$\mathbf{H} = \left.\frac{\partial \mathbf{h}(\vec{x})}{\partial \vec{x}}\right|_{\vec{x}=\hat{\vec{x}}} \tag{2.34}$$

$\vec{F}$ and $\vec{H}$ are the system dynamics and measurement matrices, respectively.

www.manaraa.com

The same equations and definitions still apply from the Kalman filter, but they are now defined using the plant $\mathbf{f}$ and measurement matrix $\mathbf{h}$ which are now functions of the state.

In summary, with both Kalman filter equations and the EKF update, the equations are:

$$\mathbf{P}_k^- = \Phi_k \mathbf{P}_{k-1} \Phi_k^T + \mathbf{Q}_k \qquad \text{(Covariance Predict)} \tag{2.35}$$

$$\mathbf{K}_k = \mathbf{P}_k^- \mathbf{H}_k^T (\mathbf{H}_k \mathbf{P}_k^- \mathbf{H}_k^T + \mathbf{R}_k)^{-1} \qquad \text{(Kalman Gain)} \tag{2.36}$$

$$\mathbf{P}_{k-1} = (\mathbf{I} - \mathbf{K}_{k-1} \mathbf{H}_{k-1}) \mathbf{P}_{k-1}^- \qquad \text{(Covariance Update)} \tag{2.37}$$

The new state estimate $\hat{x}_k$ is given by

$$\hat{\vec{x}}_k = \hat{\vec{x}}_k^- + \mathbf{K}_k (\vec{y}_k - \mathbf{h}(\hat{\vec{x}}_k^-)). \tag{2.38}$$

2.4 Thesis Filter Design and Dynamics Force Model

This thesis is a study in the performance of XNAV measurements with tracking natural closed Earth orbits. First, this section details the metrics used in this thesis to judge filter performance. It then describes the measurement model and summarizes its input. The filter's settings are then enumerated for the thesis.

Two post processing metrics are used to quantify the navigation influence of XNAV measurements. One is the definitive state error, the difference between the state and its estimate over time. It provides a profile of XNAV performance at each time step. The second metric used is the definitive state error transformed into the

www.manaraa.com

equivalent value of SMA. This is calculated through the vis viva equation (2.12). SMA has the unique property of being the primary driver of specific orbital energy. This makes the observation of SMA error a strong predictor that the definitive state error will converge [10].

The filter design uses measurement information from X-ray photons. In summary, the process takes Figure 2.12 and focuses on the filter and measurement model in Figure 2.14.

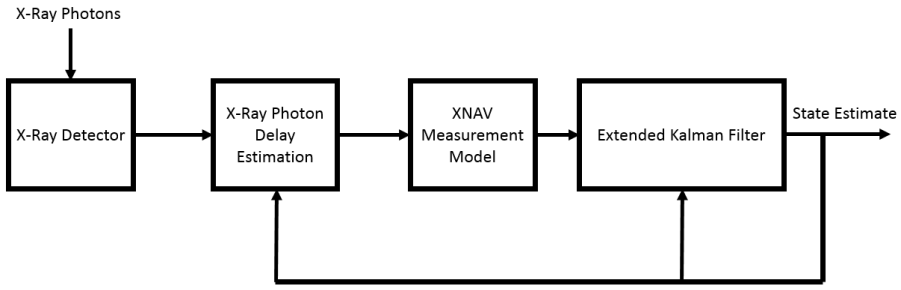

Figure 2.14: XNAV Navigation System Overview

The X-ray detector detects and time tags X-ray photons as they arrive. Time tagging photons in a process used to compare the arrival of photons at an X-ray detector to the expected arrival at Earth. With enough time tagged photons, a phase in the pulsar's signal is estimated at the detector. This estimate is compared to a reference based on Earth observations. Based on that phase, the time difference of arrival between the Earth reference and the detector is calculated. After that, the process is formulated into a state estimate and processed through the filter. This process is expanded further in chapter 3 and chapter 5. Also, with an EKF, the state estimate must be used in phase estimation as well as the filter itself.

www.manaraa.com

The EKF settings were also changed in order to address the thesis directly. The trade space looks at a wide range of closed Earth orbits. Two settings for the EKF are for the process noise matrix and the measurement noise matrix. These matrices weigh the use of the EKF estimate propagator versus the XNAV measurements in the filter process.

For this thesis, the measurement noise matrix $\mathbf{R}$ is the directly defined by Equation (3.15) in chapter 3. This equation defines a concept called the Cramér-Rao lower bound, detailed in chapter 3. Nominally, the process noise matrix $\mathbf{Q}$ would also need to be adjusted for each orbit design. The XNAV measurements are the focus of the thesis, not the tuning of the process matrix. As such, a series of changes were made to the filter in order to study measurement based navigation performance.

1. The process noise Q is zeroed out.

2. The truth and estimate state force models are exactly the same, with two body forces and the same order of higher order geopotential gravity terms.

3. The same initial state offset of 1 km SMA was made between the initial truth and estimate state.

4. The covariance initial state is set to bound the initial state offset.

Items 1 and 2 by themselves would make any navigation irrelevant, as the estimate state's dynamics on board the spacecraft would always match the truth state for all time. Item 3 ensures error growth between the estimate and the truth.

www.manaraa.com

With items 2 and 3, the filter will be forced to use XNAV measurements over the estimate propagator. Item 4 ensures that the filter will recognize a need to make a correction. With these four items, the filter relies purely on XNAV measurements for any state estimation convergence.

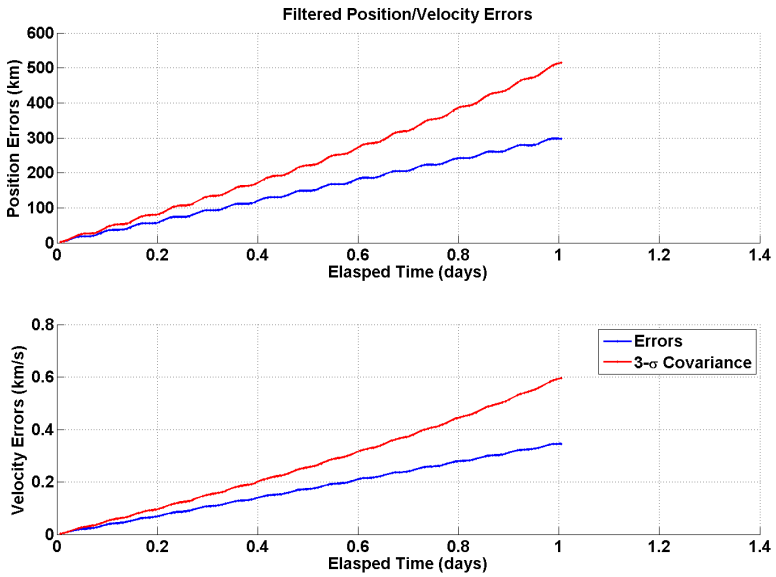

Figure 2.15: Navigation performance at a 300 km altitude circular orbit with no applied measurements

As seen in Figure 2.15, a scenario that does not apply any XNAV measurements will deteriorate. The blue line indicates the actual error between truth/estimate states while the red line indicates the filter's knowledge of that error within the covariance. As the covariance carries the variance of both position and velocity in its diagonal, the red line represents the 3σ covariance value. For both position and velocity estimates, the error within the simulation has a dominant linear increase in error, with slight sinusoidal behavior due to the higher order gravity terms. The

www.manaraa.com

XNAV measurements are the focus on the thesis and are the only driver of any navigation convergence.

Future work would include adding in more and more orbit force models into the estimate and truth propagators, while also evaluating the EKF performance based on tuning the process noise matrix. This work would involve adding Monte Carlo testing scenarios in order to characterize predictive state accuracy as well as robustly testing the process noise matrix to characterize filter performance for a given closed Earth orbit design. Finally, newer filtering techniques for nonlinear processes such as particle filters and unscented Kalman filters have been heavily considered for XNAV research and would make great future work in this challenging XNAV orbit regime [23]. The local linearization around the state estimate with the EKF means an increased sensitivity of performance to the frequency of measurement scheduling. With the various challenges that are enumerated with scheduling XNAV measurements, other formulations may prove useful.

www.manaraa.com

Chapter 3: X-ray Pulsars

This chapter details the background on X-ray pulsars as sources for XNAV and the selected sources for this thesis. An overview on pulsars is described first. This is followed by an overview of X-ray pulsar physical properties and timing models. Afterwards, the model used to simulate pulsar properties and their timing behavior is described. This includes the introduction of the Cramér-Rao Lower Bound (CRLB), a metric used to tie timing accuracy versus observation time on each pulsar. Finally, the current catalog of potential XNAV pulsars are listed and the pulsars used in this thesis are detailed.

In this chapter, there are various notations which are application specific to pulsar profiling and timing models. Context will be fully provided before using the appropriate set of variables and notations for the rest of this thesis.

3.1 Background

Pulsars are dense, magnetized, rotating neutron stars which can emit across a wide range of the electromagnetic spectrum. Pulsars are formed as the result of a compressed core after a supernova. This allows the neutron star to retain its angular momentum but with a much smaller radius. An example image of a pulsar

www.manaraa.com

can be seen in Figure 3.1. Seen in the figure, a pulsar constantly emits energy along its magnetic axis. The magnetic axis is offset from the pulsar's rotation axis. This causes the periodic wave front of energy seen at Earth. Being one of the densest known objects in the universe, the pulsar can maintain its energy emissions while rotating. Anomalies in the timing behavior of certain pulsars do occur at times as the star's energetics are not always constant. However they are infrequent and are observed every couple of years on the order of 10^{-6} seconds for the Vela pulsar to 10^{-8} seconds for the Crab pulsar [23].

Pulsars are grouped into the energy sources that maintain their rotation. These include gravitational potential energy, rotational kinetic energy, and magnetic field energy sources [28] [16]. The gravitational potential energy powered pulsar is a magnetized (10^{12} Gauss, a trillion times greater than on Earth) neutron star that exists in a binary star system with another stellar companion. To maintain both rotational and energy emission intensity, they slowly draw accreted matter from the other stellar companion to build its gravitational potential energy. However, these targets have a significant drift in period over time which requires further complexity in the on board timing models for XNAV [23] [46]. Rotation powered pulsars use the pulsar's rotational energy to emit energy. The rotation rate of these pulsars decrease more quickly than other pulsars and their magnetic fields are weaker (10^{8-9} Gauss). However, the emissions are at a more predictable rate which is useful for XNAV. Finally, pulsars called magnetars drain their own magnetic field with its own energy emissions [28] [16]. They have magnetic fields that are orders of magnitude greater than most other pulsars (10^{14} Gauss). These stars are not as popular for XNAV

www.manaraa.com

due to their less consistent timing nature to other pulsars, but they are still viable candidates for XNAV with increased observation time. The pulsars used in this thesis are MSPs. They are pulsars that used gravitational potential energy.

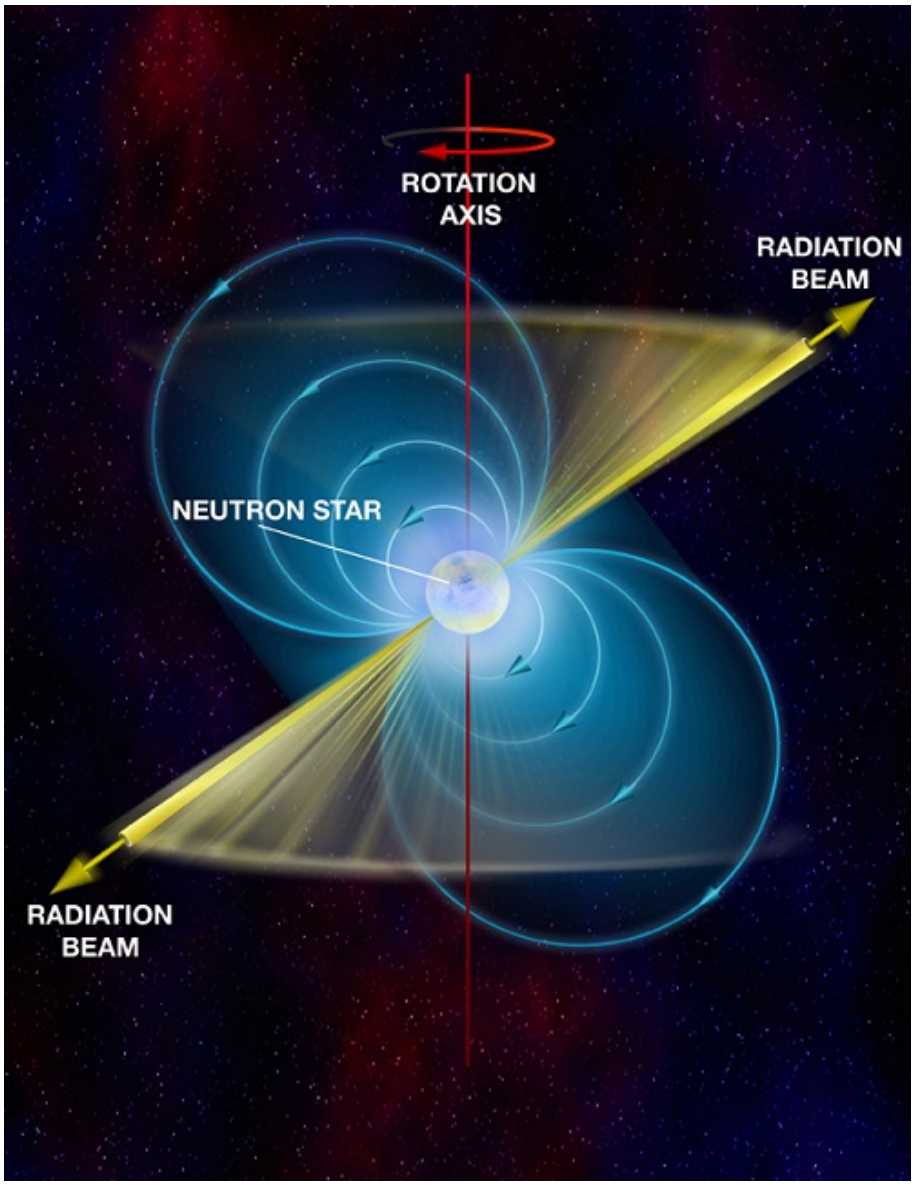

Figure 3.1: Example Image of a Pulsar [53]

A subset of pulsars that have emissions in the X-ray spectrum are called MSPs. They have a relatively fast period of 1.5-16 milliseconds and a magnetic field on the

www.manaraa.com

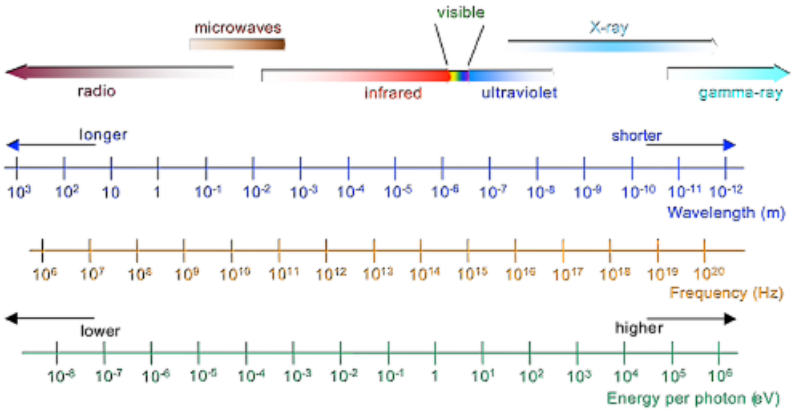

Figure 3.2: The Electromagnetic Spectrum [46]

order of 10^8 to 10^9 Gauss. They generally fall into the energy sources of gravitational potential and rotational energy. They are created when a binary star companion's accreted matter restarts and supplies energy to these pulsars [23].

MSPs are often in binary star systems and are classified into two spectral classes [21] [28].

Class I: Faint, soft broad pulses that have ideal timing behavior.

Class II: Bright hard narrow pulses that exhibit some timing noise and small glitches.

An example of both classes with a graphical representation of photon pulsar flux over cycles(or phases) can be seen in Figure 3.3.

www.manaraa.com

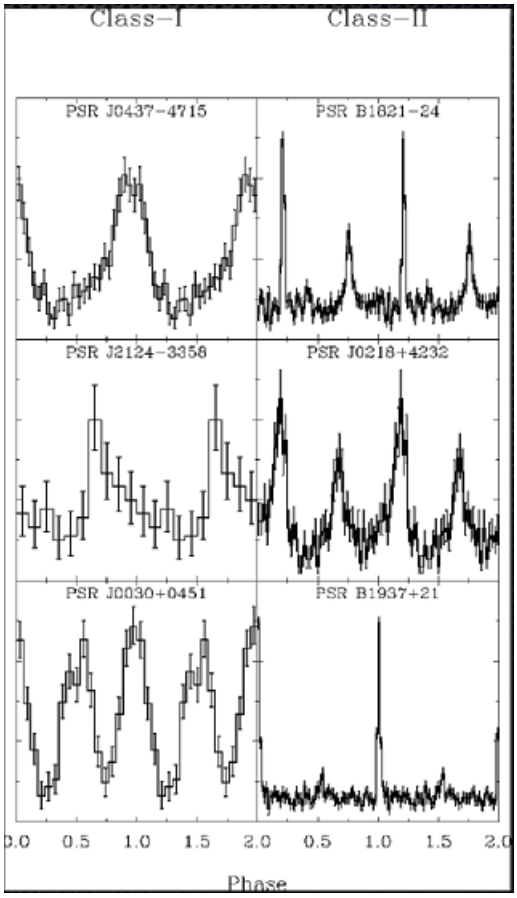

Figure 3.3: Graphical Examples of Pulsar Classes [21]

3.2 Millisecond Pulsar (MSP)

A stable timing reference is essential for navigation performance. This requires that the received photon wave fronts need some qualitative properties: significant intensity, stable periodic behaviors, and sharp emission profiles. One class of periodic sources are MSPs. MSPs have a timing stability in their emissions comparable to atomic and cesium clocks [29]. They also are observable in the X-ray spectrum, which is particular useful for XNAV [46]. These two properties are expanded in the following paragraphs.

www.manaraa.com

The timing consistency of a clock source is calculated by statistically measuring the precision of the clock over time. Research groups usually summarize this consistency with a term called the Allan variance. The Allan variance is generally defined as the time average of the squared differences of frequency deviation readings [18]. As seen in Figure 3.4, the pulsar stability of pulsars are presented on the left plot while the stability of various atomic clocks are on the right plot. The logarithmic vertical axes in both plots is the Allan variance and the logarithmic horizontal axes represent the length of the data set in years. Seen in the figure, the Allan variance for both pulsars and atomic clocks is on the order of 10^{-12} to 10^{-15} seconds after three years. An updated analysis in this area comes from Hartnett and Luiten [29]. Their plot is seen in Figure 3.5. According to current research, MSPs provide a timing accuracy comparable to atomic clocks. This is a sufficient property for XNAV using current X-ray detector technology.

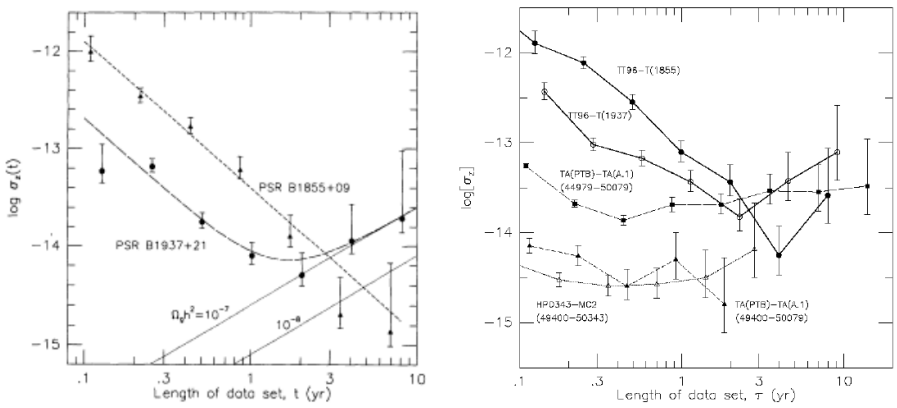

Figure 3.4: 1997 Study of Terrestrial and Celestial Timing Source Allan Variances [38]

www.manaraa.com

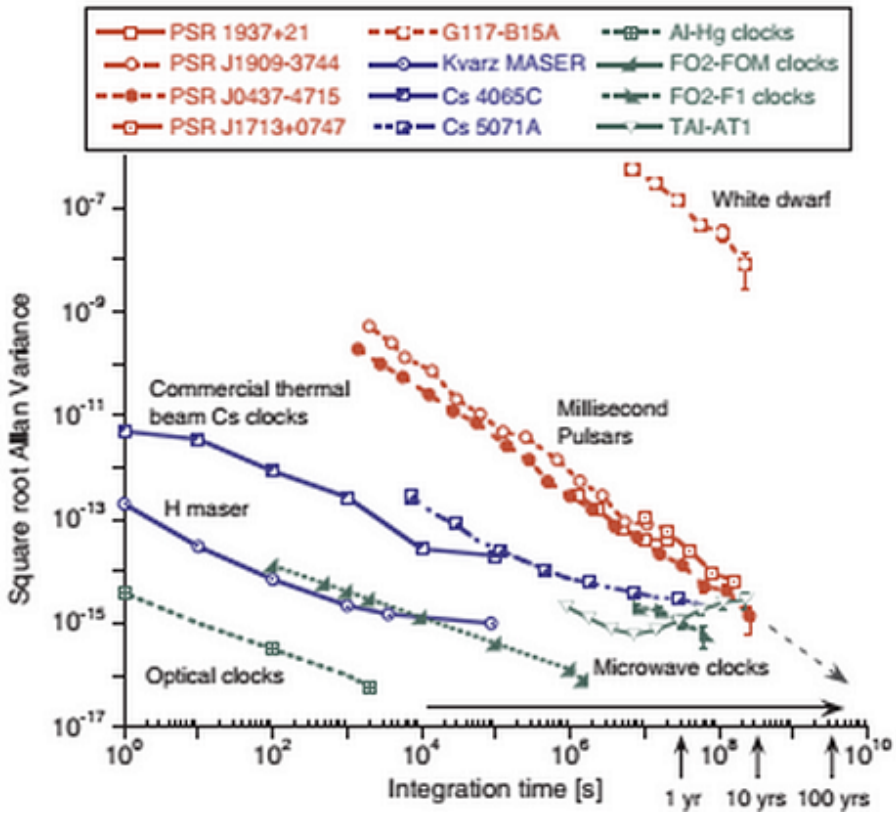

Figure 3.5: Hartnett and Luiten 2011 Study on Terrestrial and Celestial Timing Source Allan Variances[29]

Pulsars have been observed to emit in the radio, visual, X-ray, and gamma frequencies [23]. These emissions typically range from 100 MHz to a couple GHz [23]. Most frequencies are impractical as detectors on spacecraft. This is driven by the fundamental diffraction limit which determines the angular resolution that a detector can distinguish between two different sources. This term is defined by a ratio of 1.22 times wavelength over telescope diameter [53]. The angular resolution derived from the diffraction limit eliminates the practical use of the majority of the electromagnetic spectrum. The telescope diameter for most frequencies would be

www.manaraa.com

impractical to a spacecraft design [46]. The X-ray spectrum however can bring these costs down to a diameter of 13 centimeters with a instrument length of about 1 meter [53], making the X-ray spectrum a much more viable source for XNAV.

3.3 MSP Physical and Timing Properties

To model the timing behavior of an MSP at an X-ray detector, a representation of the photon time of arrivals must be formulated. With this representation, the simulation of the thesis can replicate arrival photon times for use in XNAV.

The first subsection describes an individual pulsar using a term called the total rate function. Using the rate function, the second subsection describes the stochastic representation of a photon time of arrival. The last subsection describes a metric called the Cramér-Rao lower bound. This metric is used to compare different pulsar sources for XNAV.

3.3.1 Total Photon Count Rate Function

A specific pulsar's photon time of arrivals at a detector is characterized by a total photon count rate function. In order to describe the total photon count rate, the following parameters must be described first: the light curve function, the source/background flux, and the pulsar phase.

The light curve function is a representation of photon arrival behavior over the pulsar's rotational period. As this light curve function repeats with each pulsar rotation, a subdivision of this rotation period is defined as the pulsar phase. A

www.manaraa.com

phase value of 1 is equivalent to the full pulsar rotational period. See Figure 3.6 as an example.

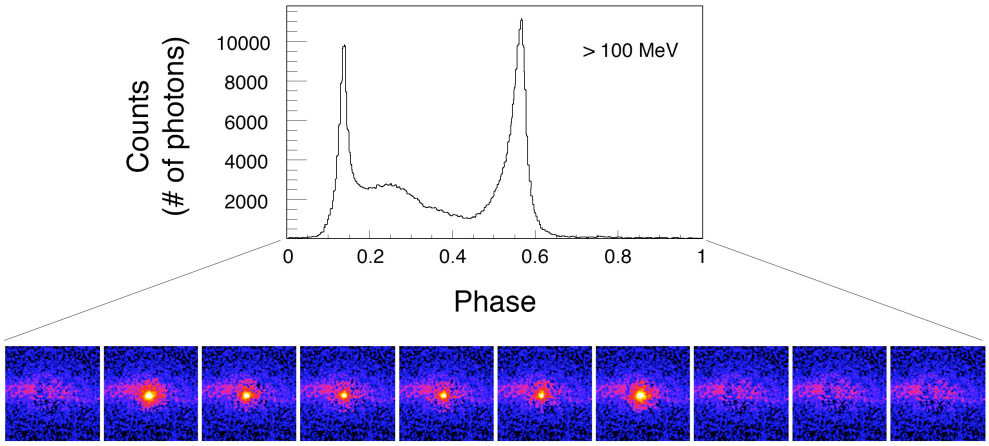

Figure 3.6: A diagram showing the Vela pulsar lightcurve profile over a single pulse. [11]

As seen in Figure 3.6, the plot depicts the total number of collected X-ray photons versus a pulsar phase. The technique that produces this information is called epoch folding. It involves averaging the data over multiple pulsar rotational periods.

When normalized so the total count rate is integrated to 1, this behavior can be comparable to other pulsars one to one. This form of the function is called the pulsar light curve function. Commonly known MSP light curve functions can be seen in Figure 3.7.

www.manaraa.com

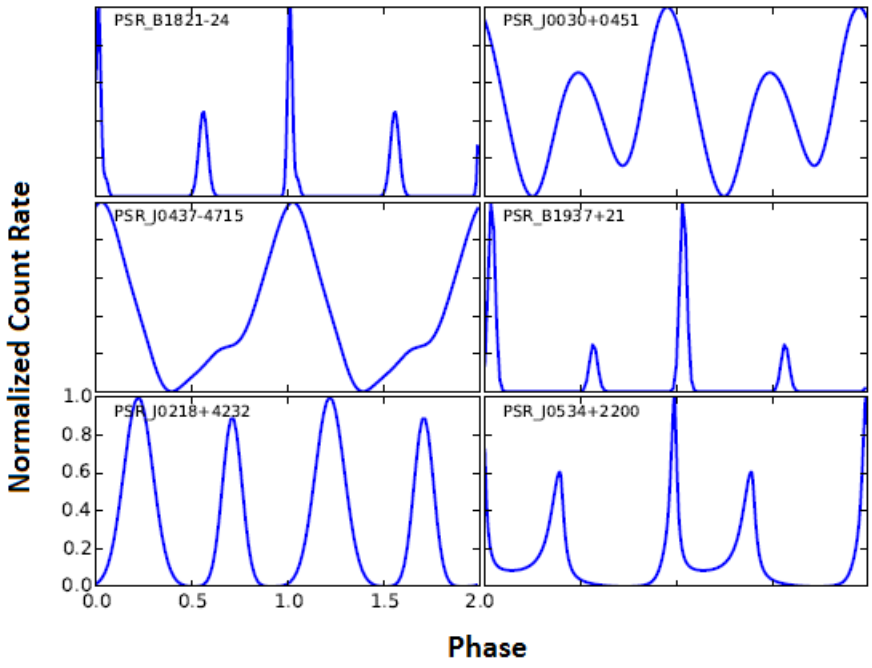

Figure 3.7: Representation of a Normalized Pulsar Profile Comparison. [54]

The fluxes (or photon count rates) that help define the pulsar alongside the pulsar light curve function are the source and the background rates. Both these rates will be greater than or equal to 0 and summarize the total magnitude of energy arriving at the detector over each phase. The source rate represents the pulsar photon counts per second that are within the detectable frequency of the x-ray detector. The background rate represents the photon counts per second of any energy outside of the source count rate. When photons are simulated in the XNAV simulation, the background count rate includes any ambient radiation around the spacecraft. The source photon count rate from an MSP is denoted with the term α and the background photon count rate is denoted as β.

Putting it all together, the total count rate function is defined in Equation (3.2)

www.manaraa.com

over time t.

$$\lambda(t) \geq 0 \tag{3.1}$$

$$\lambda(t) = \beta + \alpha h(\phi(t)) \tag{3.2}$$

Where $h(\phi)$ is a normalized light curve function, ϕ is the detected phase within a pulsar's periodic cycle and α and β terms are the source and background count rates respectively. $h(\phi)$ is the a function with the normalized phase rate, defined with the equations below. Finally, see Table 3.1 with a description of common MSPs and their count rate profiles.

$$\int_0^1 h(\phi)d\phi = 1 \tag{3.3}$$

$$min(h(\phi)) = 0 \tag{3.4}$$

In Table 3.1, the rotation period and the estimate source rate are listed. The background rate is based on energy from the given pulsar target that is not within the detectable X-ray frequency. Finally, the last column details the observatory source from which these values are calculated from. See reference [53] for further details.

www.manaraa.com

Table 3.1: List of Potential MSP Pulsars for Navigation [54]

Name	Period (ms)	Source Pulsed Rate (α, cnts/s)	Total Bkg Rate (β, cnts/s)	TOA & Models Source
Crab Pulsar	33.000	660.000	13860.20	Jodrell Bank
B1937+21	1.558	0.029	0.24	PPTA
B1821-24	3.054	0.093	0.22	PPTA/Nançay
J0218+4232	2.323	0.082	0.20	Nançay
J0030+0451	4.865	0.193	0.20	NANOGrav
J1012+5307	5.256	0.046	0.20	NANOGrav
J0437-4715	5.757	0.283	0.62	PPTA
J2124-3358	4.931	0.074	0.20	PPTA
J2214+3000	3.119	0.029	0.26	NANOGrav
J0751+1807	3.479	0.025	0.22	Nançay
J1024-0719	5.162	0.015	0.20	PPTA

3.3.2 Photon Time of Arrival(TOA) Model

In order to perform XNAV, photons are time tagged and collected over observation periods on the pulsar. Detailed in chapter 5, the process of simulating a XNAV measurement comes from an observing a batch of simulated photon time of arrivals.

This subsection states how the photons are simulated for time tagging in the thesis simulation. Much of this formulation is detailed in various references, but the

www.manaraa.com

fundamental equations and assumptions are defined in Emadzadeh's textbook [23].

Consider the variable t_i as the time of arrival of the i^{th} photon, with $t_0 = 0$. Then note the definition of N_t:

$$N_t = max(n, t_n <= t) \tag{3.5}$$

This value N_t indicates the number of detected photons in the time range $(0, t)$. Photon time of arrivals are typically defined as a stochastic non-homogeneous Poisson process (NHPP) with a time varying rate defined as $\lambda(t) \leq 0$. Its properties include [23]:

1. Probability of detecting one photon in a time interval is

$$P(N_{t+\Delta t} - N_t = 1) = \lambda(t)\Delta t \tag{3.6}$$

   for $\Delta t \to 0$.

2. Probability of detecting more than one photon in the time interval is

$$P(N_{t+\Delta t} - N_t \geq 2) = 0 \tag{3.7}$$

   for $\Delta t \to 0$.

3. Non-overlapping increments are independent, where

$$N_t - N_s \tag{3.8}$$

   for $t > s$ is the increment of the stochastic process $(N_t, t > 0)$

www.manaraa.com

From here, the number of detected photons over a given period is defined by the Poisson random variable for N_t:

$$P(N_t = k) = \frac{1}{k!}[(\int_0^t \lambda(x)dx)^k * e^{-\int_0^t \lambda(x)dx}] \tag{3.9}$$

The mean is

$$E[N_t] = var[N_t] = \int_0^t \lambda(x)dx = \Lambda(t) \tag{3.10}$$

While the probability density function is

$$P(t_{i\,i=1}^{M}, M) = \begin{cases} e^{-\Lambda} \prod_{i=1}^{M} \lambda(t_i) & \text{for M} \geq 1 \\ e^{-\Lambda} & \text{for M} = 0 \end{cases} \tag{3.11}$$

The function $\lambda(t)$ is the total count rate function as described earlier. A graphical representation of photon time of arrivals and the light curve is presented in Figure 3.8. The pulsar light curve is plotted in red alongside associated photon time of arrivals in blue. The continued collection of photons in blue should add photon arrivals that resemble the pulsar light curve in red.

www.manaraa.com

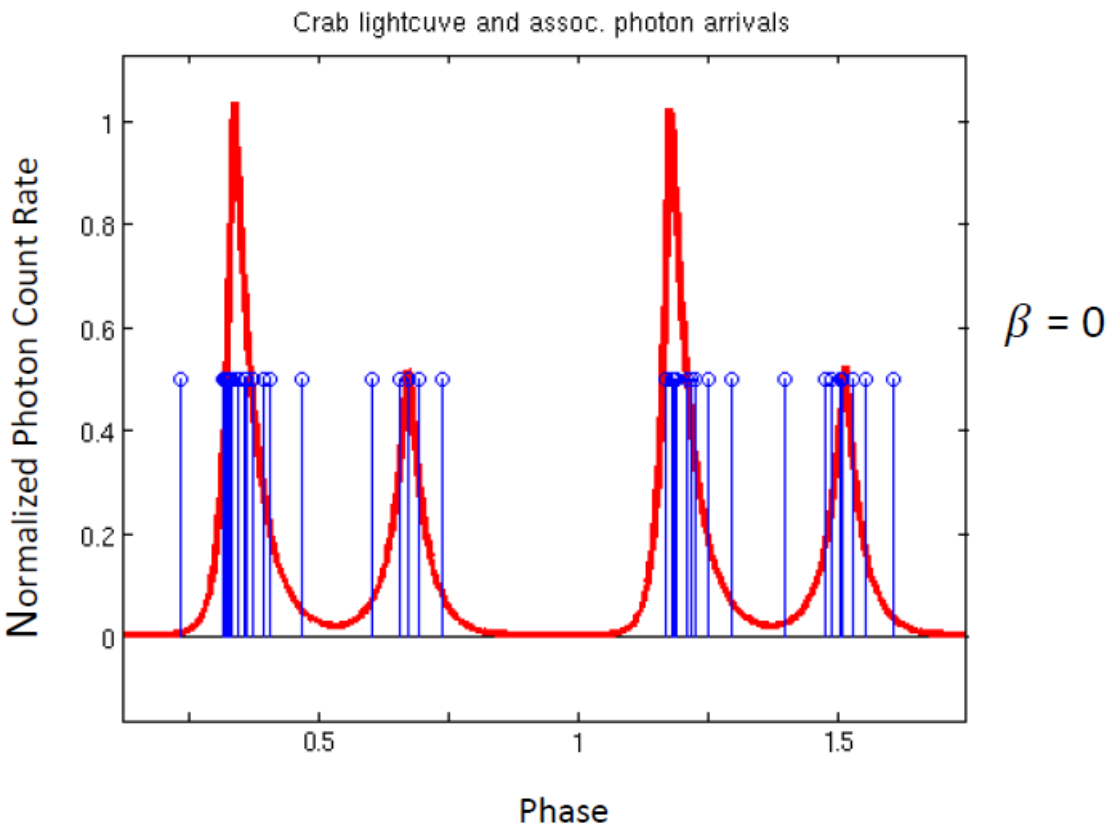

Figure 3.8: Light Curve function with Associated Photon Arrivals. [28]

The background rate of the curve seen in Figure 3.8 is 0. Increasing the background count rate means that the blue photon arrivals arrive with a higher flux. This increased flux deteriorates the correlation between the light curve and the associated photon arrivals, resulting in a deteriorated timing accuracy of the pulsar XNAV measurement. The thesis models the local background radiation of the spacecraft for the XNAV measurement process.

In the thesis simulation, this process is used to simulate photon time of arrivals to the X-ray detector. When enough photon time of arrivals are calculated,

www.manaraa.com

calculations are made to compare the X-ray detector's time offset with the Earth reference to make an XNAV measurement. These calculations are described in chapter 5. However, the time offset is calculated with an estimator. Thus, a metric called the Cramér-Rao lower bound can be used to compare pulsar measurement performance [23].

3.3.3 Cramér-Rao Lower Bound (CRLB)

The CRLB places a lower bound on the variance of any unbiased estimator [23]. With XNAV, this term is used primarily to characterize how much observation time (T_{obs}) it will cost to be able to achieve a variance of timing error for estimating pulsar photon time of arrival. This formulation does not take into account any hardware or systematic errors that may increase observation time, so it is an optimistic figure of merit for pulsar timing accuracy. Timing accuracy, using light time delay, is an indication of the lower bound of position state accuracy for XNAV. It is also used as the measurement noise matrix for the EKF of the thesis, described in chapter 2. $\vec{L}$ holds the unknown phase/frequency, and is defined as:

$$\vec{L} = (\phi, f)^T \tag{3.12}$$

The CRLB is defined as the inverse of the Fischer information matrix $I(\vec{L})$ [23]:

$$I(\vec{L}) = \frac{I_p}{6}\begin{bmatrix} 6T_{obs} & 6T_{obs}^2 \\ 3T_{obs}^2 & 2T_{obs}^3 \end{bmatrix} \tag{3.13}$$

www.manaraa.com

where

$$I_p = \int_0^1 \frac{[\alpha h'(\phi)]^2}{\beta + \alpha h(\phi)} d\phi \tag{3.14}$$

So

$$CRLB(\vec{L}) = I^{-1}(\vec{L}) = \frac{2}{I_p} \begin{bmatrix} \frac{2}{T_{obs}} & \frac{3}{T_{obs}^2} \\ \frac{-3}{T_{obs}^2} & \frac{6}{T_{obs}^3} \end{bmatrix} \tag{3.15}$$

3.3.4 Pulsar Location and Visibility

Pulsars must be visible to the X-ray detector to be used for XNAV. The majority of pulsars are along the galactic ecliptic seen in Figure 3.9. Solar occultations are also depicted and are further detailed in chapter 5.

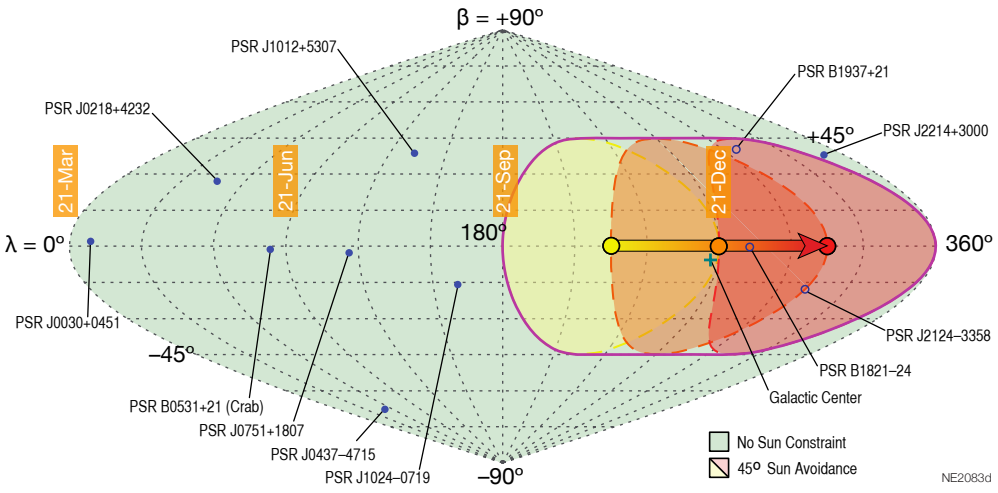

Figure 3.9: A diagram of the distribution of possible MSPs in the galactic ecliptic frame [39].

As seen, the majority of targets can be visible throughout the year, with most of them below the ecliptic latitude β of +/-45°. Figure 3.10 gives a binary representation of that visibility with each colored line when the pulsar is visible in

www.manaraa.com

a LEO.

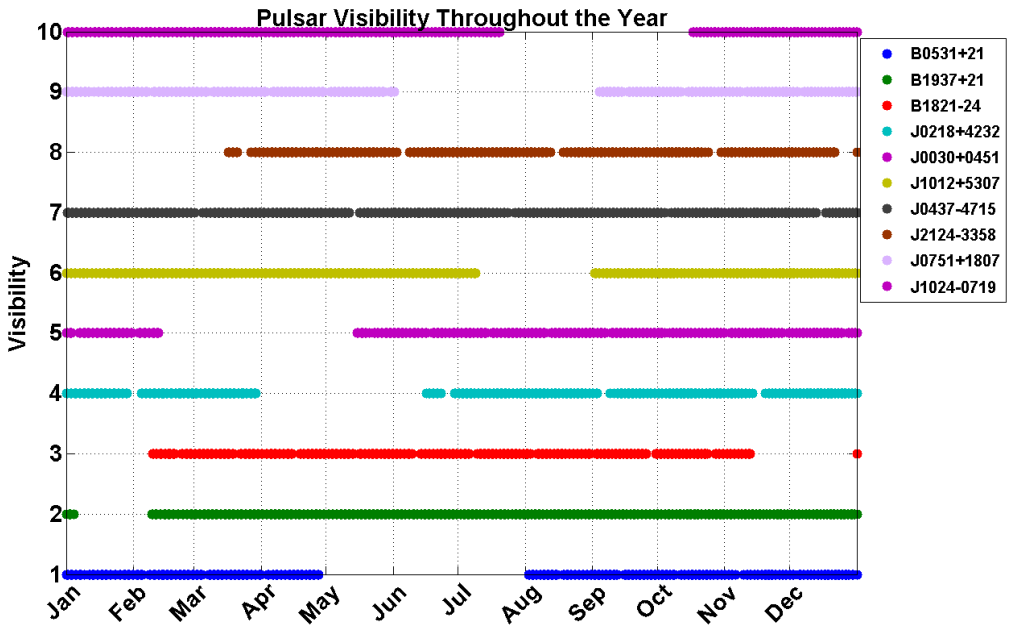

Figure 3.10: Visibility of Potential Pulsars in LEO throughout the Year

Solar occultations are a significant factor in driving MSPs visibility and ultimately XNAV. They are represented as the orange areas seen in Figure 3.9 and the large gaps seen in Figure 3.10. The formulation of how these occultations are modeled are addressed in later sections.

Pulsar directions can be converted from ecliptic latitude and longitude into unit vectors in the ECI frame, as seen in Table 3.2.

Note that, with the significant distance of the pulsars from an Earth orbit regime, this table can be used for any inertial coordinate frame, so long as its origin is the same order of magnitude distance from these pulsars.

www.manaraa.com

Table 3.2: List of Potential MSP Pulsars ECI Unit Vectors [54]

Name	Unit X	Unit Y	Unit Z
B0531+21	0.102	0.921	0.375
B1937+21	0.392	-0.843	0.368
B1821-24	0.097	-0.902	-0.421
J0218+4232	0.607	0.417	0.676
J0030+0451	0.988	0.132	0.085
J1012+5307	-0.535	0.271	0.800
J0437-4715	0.240	0.635	-0.734
J2124-3358	0.646	-0.520	-0.559
J0751+1807	-0.443	0.841	0.311
J1024-0719	-0.907	0.401	-0.127

3.4 Thesis X-Ray MSPs Properties and Settings

Four pulsars were chosen for this thesis. The number and location of pulsars were chosen to provide a diverse geometric set of data to solve for a state in three dimensions. The pulsars chosen for this thesis were: B1937+21, B1821-24, J0218+4232, and J0437-4715.

These targets were selected as a minimum set of required pulsars for XNAV. They were also chosen based on their documented use in multiple research papers [54] [39]. The thesis does not include a separate trade analysis on the selection between all MSP targets. This is due to the added complexity of the thesis scope.

www.manaraa.com

Table 3.3: List of Thesis MSP Pulsars for Navigation

Name	Period (ms)	Source Pulsed Rate (α, cnts/s)	Total Bkg Rate (β, cnts/s)	TOA & Models Source	ECI Unit X	ECI Unit Y	ECI Unit Z
B1937+21	1.558	0.029	0.24	PPTA	0.392	-0.843	0.368
B1821-24	3.054	0.093	0.22	PPTA/Nançay	0.097	-0.902	-0.421
J0218+4232	2.323	0.082	0.20	Nançay	0.607	0.417	0.676
J0437-4715	5.757	0.283	0.62	PPTA	0.240	0.635	-0.734

A future study in this direction would require running the thesis orbit design cases with all possible combinations of other pulsars. The simulated X-ray detector in this thesis can only study one pulsar at a time. Because of this fact, observation scheduling would need to be understood across all combinations of MSPs.

In the ECI frame, the four pulsars have unit vectors from Earth, as seen in Figure 3.11. Note that the targets are not evenly spread across the ECI x axis; the chosen pulsar target were a compromise between geometry, timing accuracy and other timing model properties.

The four pulsars are also evaluated on their timing model accuracy versus observation time with the CRLB bound. Timing accuracy is represented in Figure 3.12 as the timing standard deviation. The greater the deviation, the less accurate the state estimate pulsar information becomes.

Figure 3.12 represents the phase timing standard deviation versus observation time. It is the value in the position (1,1) of the 2x2 matrix seen in Equation (3.15) versus observation time. On the logarithmic scale, increasing the observation time on a pulsar results in the overall decrease of the standard deviation of calculating photon time of arrival. These pulsars provided a grouping of timing accuracy which is comparably more accurate than the other pulsar targets. Future work would

www.manaraa.com

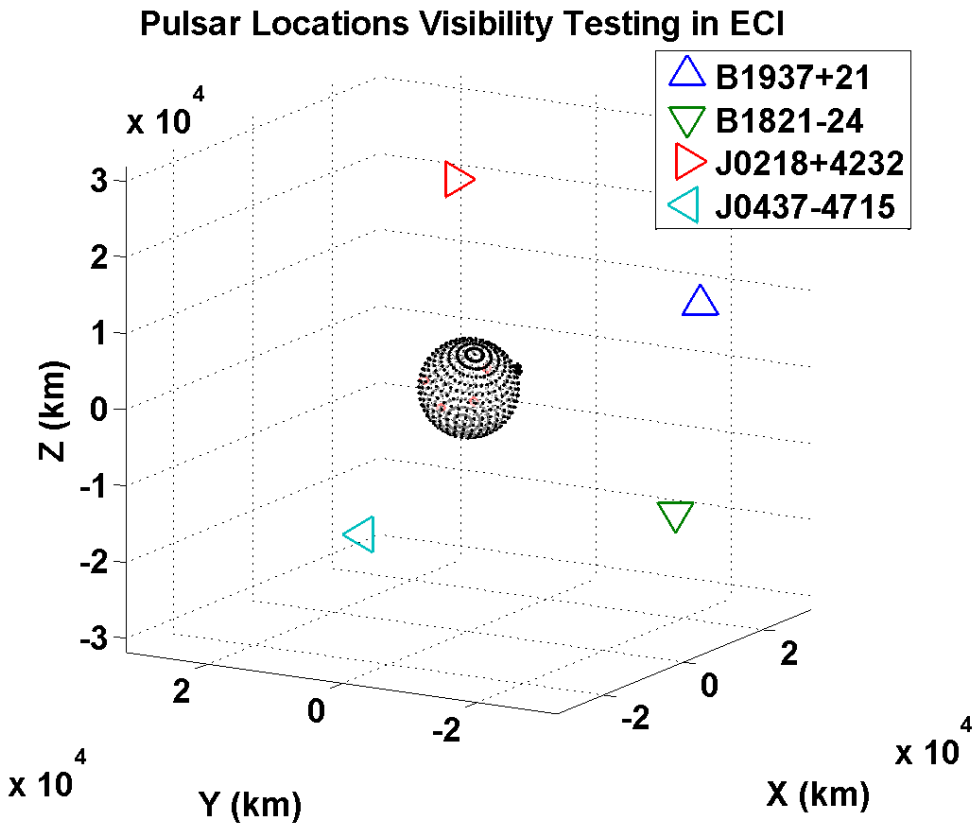

Figure 3.11: Thesis Pulsar Unit Vectors in ECI

include adding further targets, as well as including phase estimation techniques in characterize their performance compared to the analytical CRLB.

It is also important to note that one can choose any point along each plot in Figure 3.12 and dynamically adjust timing accuracy for navigation performance. This study fixes that value. There is future work in the subject of dynamically modifying these settings while performing XNAV.

The setting chosen on the CRLB is based on providing effective timing accuracy while also adjusted for reasonable observation periods. Too little observation time and timing accuracy will be insufficient. Too much observation time will de-

www.manaraa.com

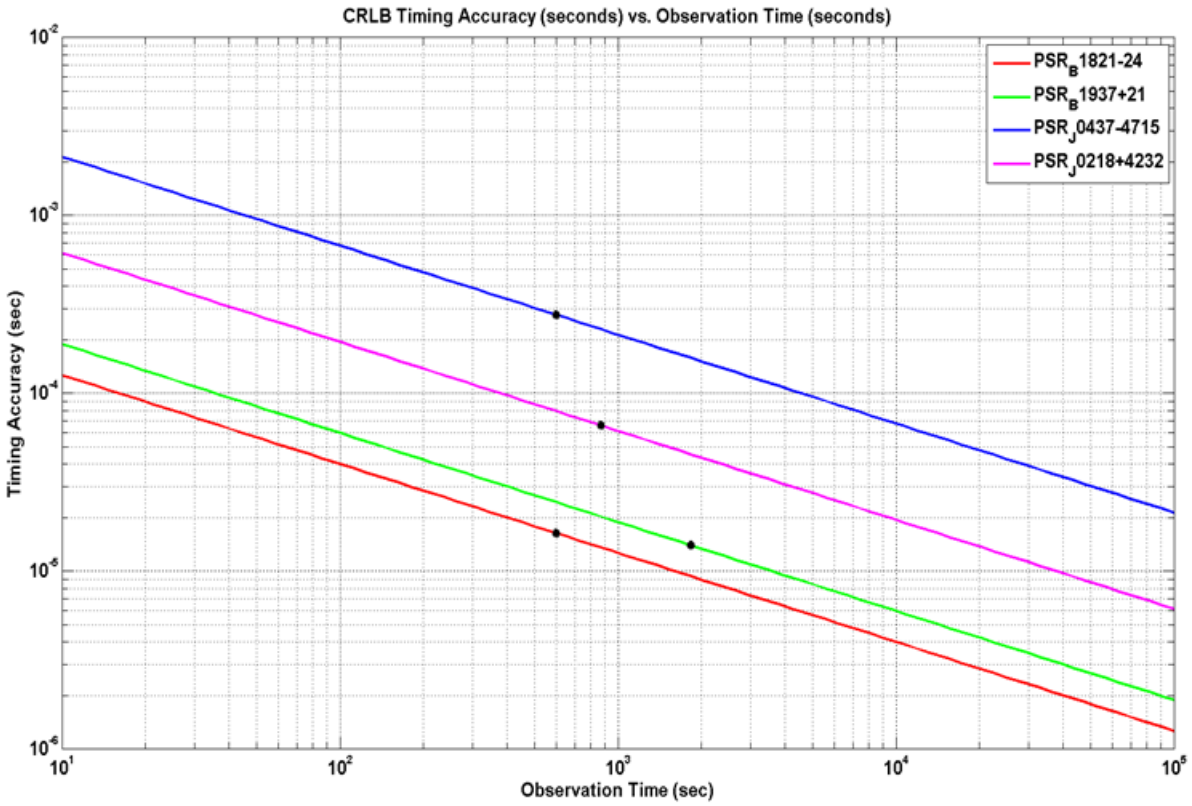

Figure 3.12: Source pulsars chosen and CRLB observation time

grade the measurement information over multiple orbits. To set the navigation performance overall, a lower bound of observation time was made based on providing a minimal 2e-5 second timing accuracy(an equivalent to about 5 km of position state accuracy). On the other side, observations of each pulsar were capped based on the orbital period of the smallest value of SMA in the trade space (5400 seconds). With occultations and other limiting factors of visibility on XNAV, a maximum was placed at 1800 seconds of observation time. With both the vertical and horizontal axis bounded, the following observation times were chosen in Table 3.4. The chosen values are represented by the black dots in Figure 3.12.

www.manaraa.com

Table 3.4: List of Thesis MSP Pulsars CRLB Observation

Name	Timing Accuracy (sec)	Observation Time (sec)
B1937+21	1.40e-5	1800
B1821-24	1.64e-5	600
J0218+4232	6.4e-5	900
J0437-4715	2e-4	600

This provides some variation of observation time below 1800 seconds while also attempting to reach a 5 km position state accuracy. Further work in this area in terms of navigation performance may prove fruitful.

Please note that the CRLB lower bounds the XNAV measurement timing accuracy to about a 5 km position accuracy. This is the general baseline to be expected of this formulation of XNAV performance. It is an estimate of the NICER mission hardware as well as the estimation of pulsar time of arrivals. This is not true for all formulations, but it is for the particular formulation that is based on the SEXTANT mission [39]. The NICER hardware and the SEXTANT mission information used in this thesis is elaborated on in chapter 4.

www.manaraa.com

Chapter 4: XNAV-Related Hardware

This chapter describes the hardware properties used in this thesis. The chapter starts by reviewing past spacecraft X-ray detector experiments and an overview of the detector hardware. The chapter concludes with a listing of all the hardware challenges that were implemented into this thesis.

4.1 Previous Research and Development

The exploration of X-ray signals from pulsars and other celestial bodies must be made from orbiting spacecraft due to atmospheric attenuation. This can be seen in Figure 4.1. A variety of X-ray spacecraft have been launched in order to explore pulsars and their X-ray signals. These include the NRL USA experiment on ARGOS (1993), Rossi X-ray Timing Explorer (RXTE)(1995), Chandra X-ray Observatory (1999), the DARPA XNAV and XTIM projects along with Ball Aerospace, Microcosm Inc., and NRL (2005 and 2009 respectively) and finally the NASA NICER and SEXTANT missions [12] [43] [55] [28] [40].

Spacecraft X-ray experiments are based on the detectable energy range, effective area, and the timing accuracy of the detectors. Within these general parameters, multiple missions vary their performance capabilities based on their official mission.

www.manaraa.com

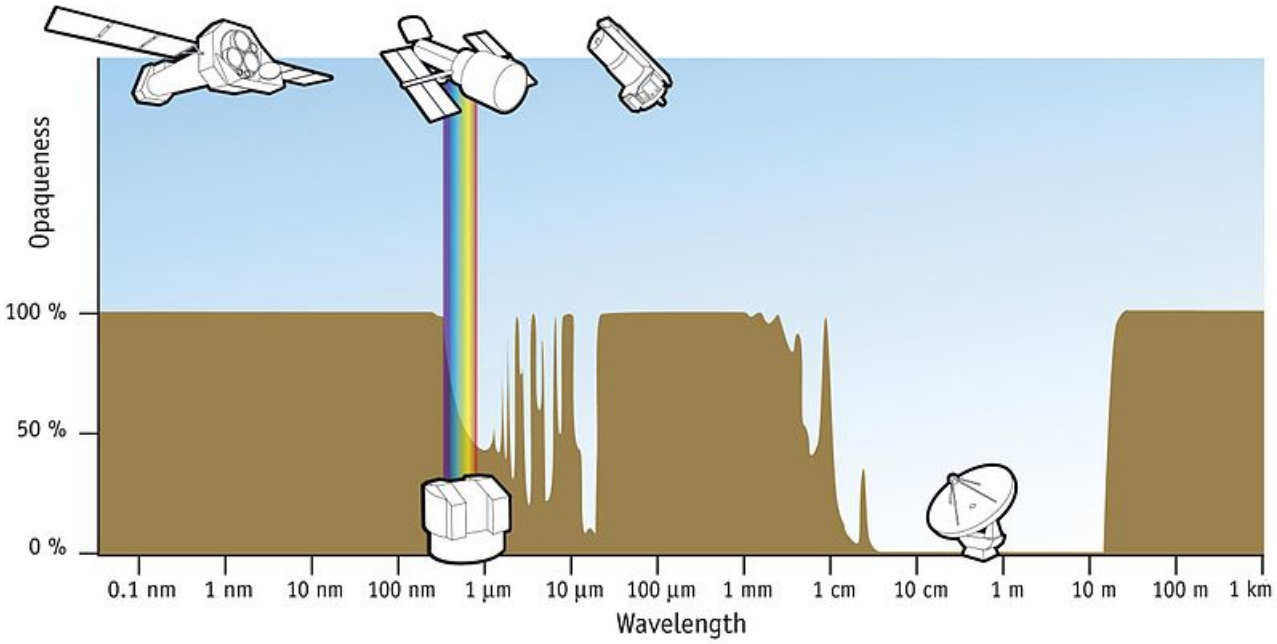

Figure 4.1: Visibility of Signals in the Electromagnetic Spectrum. X-ray signals range from 10 nm to 10 pm [41]

X-ray detectors work by measuring the energy that is released when X-ray photons collide with atoms within the detector material. That energy is proportional to the amount of photons that are detected. The NICER/SEXTANT mission uses an X-ray detector with silicon drift detectors. Silicon drift detectors are devices that measures X-ray photon energy by the ionization of a highly pure silicon. A series of ring electrodes then cause the electron to drift into a collection electrode, allowing the instrument to measure higher count rates. Nanosecond level timing is possible with this instrument. [46] [25]. Further information on X-ray detectors can be found in A.

With these detectors, X-ray instruments usually add concentrator optics and

www.manaraa.com

other electronic hardware in order to reject background radiation. For example, the source count rate on the Crab pulsar and the other MSPs are orders of magnitude different, as seen in Table 3.1. Variations of hardware must be made in order to accommodate both sets of pulsars.

When it comes to pulsar timing accuracy, a variety of detectors and instrument suites can maximize the amount of timing accuracy for a particular set of pulsar measurements.

4.2 NICER/SEXTANT mission

The infrastructure of the NICER/SEXTANT mission is borrowed heavily for the thesis. This thesis does not use any NICER hardware specifications for its results. The thesis models the simulation as an imitation of the X-ray detector. Different missions would design a different instrument, but this thesis uses the NICER instrument as a template.

Further work can be pursued in the systems level design of a X-ray detector for XNAV. Further elaboration on these assumptions will be detailed in chapter 5.

The thesis does use a significant amount of the SEXTANT mission infrastructure. The algorithms used in the thesis and their formulation are detailed in full in both reference [39] and [54].

www.manaraa.com

4.2.1 NICER Overview and Hardware

NICER is a NASA explorer mission of opportunity whose purpose is to study gravitational, electromagnetic, and nuclear physics environments within neutron stars. It is designed to observe soft X-rays within 100 nanosecond timing resolution in a 0.2-12 eV environment as a X-ray detector instrument an an external payload on board the ISS. It has a peak effective area of 1800 cm^2 at 1.5 eV. NICER and it's software enhancement SEXTANT will be launched on a SpaceX rocket to be an on board payload on the ISS in 2016. NICER has been the subject of various publications and announcements [26] [39].

The instrument consists of co-aligned 56 X-ray concentrator optics, each with silicon drift detectors [26]. See Figure 4.2 for a general image and location of instruments. It is approximately a 1 m^3 telescope array that folds forward to stow into the ISS Express Logistics Carrier(ELC) interface, which can be seen in Figure 4.3.

The NICER design is made in order to reject the local background radiation with each of the 56 X-ray telescopes. It also must rotate to point to each individual pulsar target to tag pulsar TOA to within its 100 nanosecond resolution.

4.2.2 SEXTANT Overview

The SEXTANT technology demonstration is a flight software enhancement to the NICER instrument, funded by the NASA Space Technology Mission Directorate (Space Technology Mission Directorate (STMD)). The team will use the same data stream as NICER to perform XNAV-only orbit determination. The SEXTANT team

www.manaraa.com

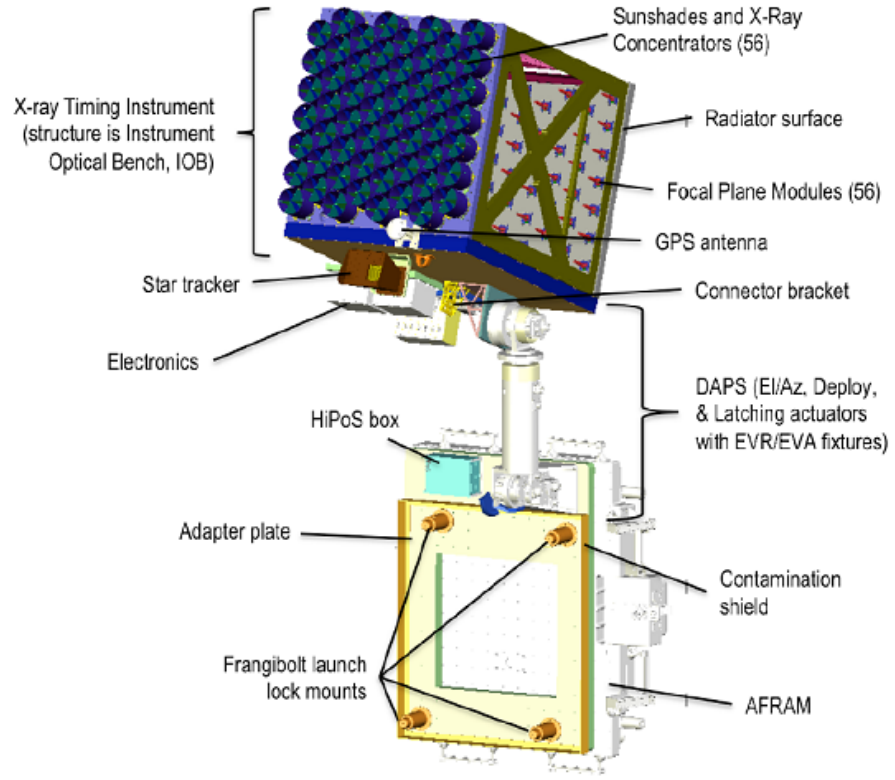

Figure 4.2: NICER Instrument Image. Concentrator optics are in blue which will be mechanically pointed towards each pulsar target [26].

will seed their navigation filter with a degraded GPS solution from the NICER GPS instrument before performing XNAV. The demonstration is considered successful if the on-board position knowledge error is no more than 10 km Root Sum Square (RSS) worst direction within 2 weeks of measurements [39] [53].

As seen in Figure 4.4, the infrastructure is designed to generate orbit/pulsar information, generate navigation measurements, and then apply them to a state estimate in a navigation filter. In other words, this simulation can be broken down into three sections: orbit design/pulsar profile, simulate pulsar measurements, and finally the navigation filter. This process starts by generating a truth ephemeris using an

www.manaraa.com

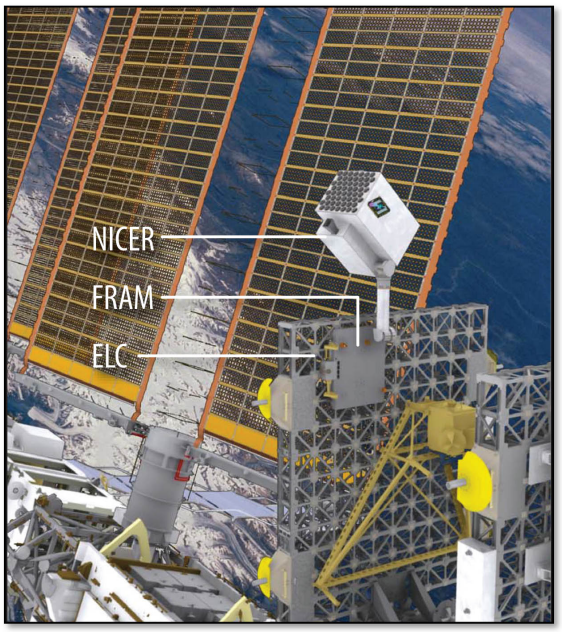

Figure 4.3: NICER instrument on the Flight Releasable Attachment Mechanism(FRAM) and Express Logistics Carrier(ELC) of the ISS [12]

open source NASA orbit design tool called GMAT [32]. Using this ephemeris, the simulation calculates any orbit specific parameters such as pulsar visibility and the orbit background radiation. Using this information, a pulsar observation schedule and the relevant on-board pulsar timing models are generated [39].

The simulation has three paths to simulate photon measurements. The red arrowed testing path is a process that simulates navigation measurements and measurement noise with the pulsar information. The green arrowed path is a process that simulates photons individually, using the gathered time tagged information for measurements. The blue arrowed path is a process that uses a laboratory hardware X-ray emitter and detector experiment to physically time tag photons for measurements. Once the measurement is created it goes into the EKF to estimate the state

www.manaraa.com

of the spacecraft [39].

www.manaraa.com

المنارة للاستشارات

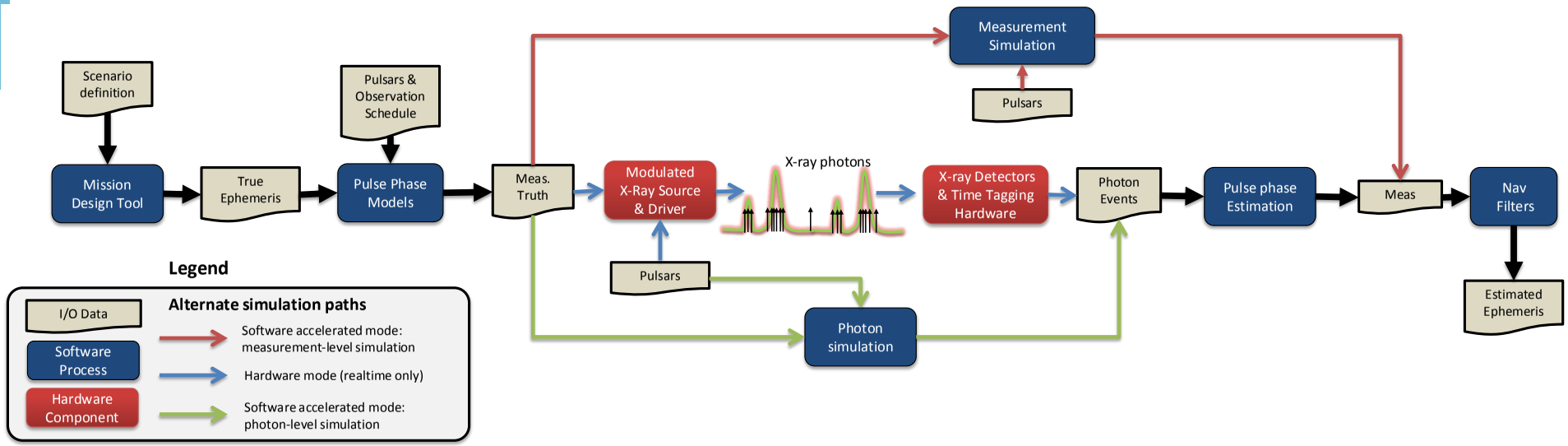

Figure 4.4: SEXTANT Testing Infrastructure [53]

www.manaraa.com

4.3 Thesis Hardware Implementation

NICER is a science mission that, with the SEXTANT mission enhancement, is an example of an XNAV instrument. Though it is not optimized specifically for XNAV, it is an instrument that encompasses challenges inherent in maintaining appropriate timing resolution for XNAV. Current research in XNAV now include hardware testing [54] [3]. This thesis includes these assumptions as they are relevant to XNAV research.

The simulation used for the thesis is a heavily redesigned SEXTANT simulation. It is redesigned to handle the trade space outside of the SEXTANT LEO orbit design. There are also several assumptions about the hardware. They include:

1. The instrument is not on the ISS, but a generalized Earth orbiting spacecraft.

2. The instrument collects X-ray photons from one pulsar target at a given epoch. Multiple pulsars cannot be observed at one time.

3. Slew is modeled in the design of the pulsar observation schedule as a constant velocity with no hardware obstructions.

4. The pulsar observation schedule is generated before running the filter state estimate using that schedule.

5. The hardware is capable of handing the environment of the studied orbit trajectory.

The trade space of orbits that the thesis studies involves a unique spacecraft

www.manaraa.com

design that can handle the orbit environment without hardware failure. This thesis does not model hardware reliability. Future work can be put into studying the hardware capabilities of an X-ray detector to provide more effective background radiation shielding. Some possible hardware additions would be a tungsten field of view limiter, a permanent magnet to sweep out low energy electrons, or adding radiation hard material around the detector to reject any ambient energy sources in the X-ray frequency.

This thesis assumes that it is feasible to generate XNAV measurements, but it does model how the background radiation influence the XNAV measurement. This is elaborated on in chapter 5.

www.manaraa.com

Chapter 5: Testing Overview

The testing process used to perform XNAV is detailed in this chapter. First, the chapter gives an overview of the entire simulation and how it is organized. It then describes the trade space of this thesis as well as the force models / spacecraft parameters used. Afterwards, the orbit design/pulsar profile models needed to make the XNAV measurement within the thesis trade space are described. Finally, the chapter reviews how an XNAV measurement is generated.

5.1 Thesis Simulation

The thesis takes the SEXTANT simulation process and breaks up the process into three main sections: orbit design/pulsar profile, simulating pulsar measurements, and the navigation filter.

The orbit design/pulsar profile section of Figure 5.1 describes the information needed to run the XNAV simulation. The orbit truth ephemeris is first generated in the NASA open source software called GMAT. Using the ephemeris, pulsar visibility and scheduling is then generated. The background radiation environment throughout the projected spacecraft trajectory is also calculated in this section. Finally, pulsar timing information for the spacecraft trajectory is generated.

www.manaraa.com

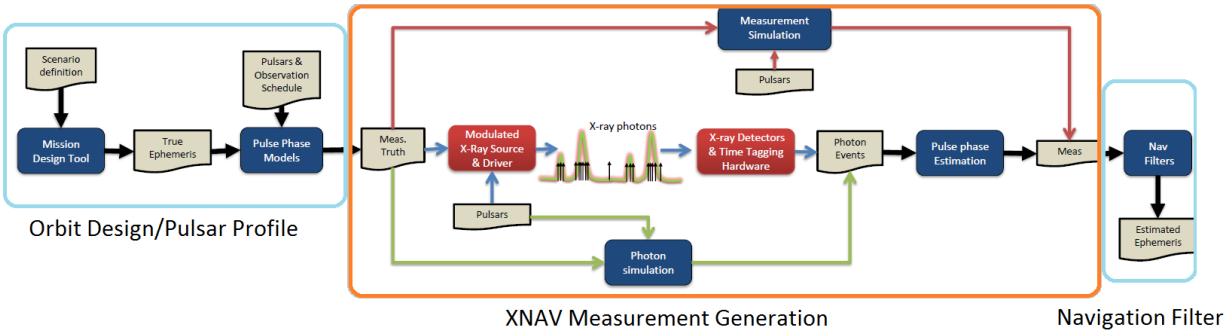

Figure 5.1: Thesis Simulation Infrastructure [53]

Once the orbit design/pulsar profile information is produced, the simulation runs the XNAV measurement process and the EKF filter concurrently. This is continued until the end of the scenario.

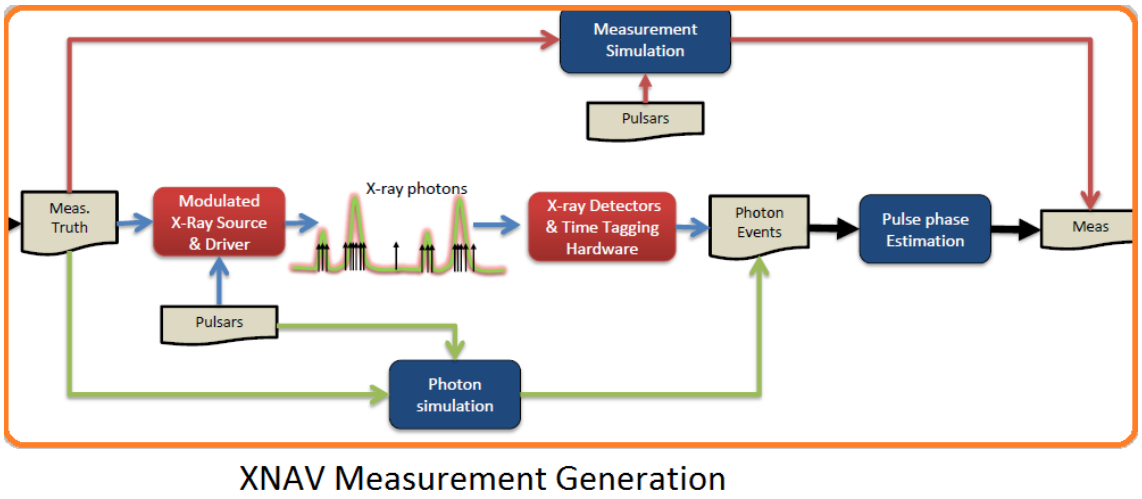

Figure 5.2: Thesis Simulation: XNAV Measurement Generation with all Paths

For generating XNAV measurements, the green arrowed path seen in Figure 5.2 was chosen for this thesis. The formulation of simulating pulsar measurements was

www.manaraa.com

not created for this thesis, only used. The design of the pulsar measurement model is discussed in detail in [54]. Background on pulsars used in this chapter can be found in chapter 3. After the measurement is generated, the measurement is ingested by the EKF and processed into the running state estimate solution. The flight software called NASA Goddard's Enhanced Onboard Navigation System (GEONS) implements the EKF and performs the state estimation [37]. The chosen settings and parameters of the EKF for this thesis are detailed in chapter 2.

The design work done for this thesis focuses on the cyan areas of the simulation. These include the orbit design and the navigation filter sections. The simulation of pulsar measurements was, as stated earlier, simply used for this thesis.

5.2 Spacecraft Parameters and Orbit Trade Space

This section describes the spacecraft dynamics and the orbit geometry trade space used in this thesis. For spacecraft dynamics, this includes parameters that are used to define the spacecraft's orbit trajectory.

As seen in Table 5.1, the spacecraft mass was chosen as a common reference mass for Earth spacecraft [32]. The force models include only two body motion and higher order gravitational parameters. The force model uses higher order gravity terms by setting $N = 30$ in Equation (2.6).

The orbit design trade space is a set of initial Kepler element orbit parameters of the spacecraft. As these trajectories are natural orbits, Table 5.2 lists the initial orbit parameters that the spacecraft will start at before traversing.

www.manaraa.com

Table 5.1: List of Thesis Spacecraft Parameters

Spacecraft Parameter	Value
Spacecraft Mass	800 kg
Force Model: Primary Body	Earth
Force Model: Gravity Field Degree	30
Force Model: Third Body Point Masses	None
Force Model: Solar Radiation Pressure	None
Force Model: Tidal Forces	None
Force Model: Atmospheric Drag	None

These initial orbit parameters are used with a GMAT propagator to produce a simulated ephemeris of the scenario. This ephemeris is used for producing products throughout the simulation. Restrictions on this trade space were made to eccentricity and true anomaly. Eccentricity was set to accommodate for the Earth surface. The range of ECC from 0.0-0.8 avoids a perigee that is underneath the Earth surface. TA was restricted to decrease the size of the trade space. TA is an angle that is relative to the eccentricity vector, while AOP is a relative angle that relates the eccentricity vector to the Earth's equatorial plane. This inherent coupling and a limitation in computation time resulted in fixing the TA to an initial value of 0°.

The experiment period from the start epoch was chosen to observe transient and steady state behavior of the filter performance. Due to the trade space of SMA, the experimental period needs to be significantly longer than the maximum orbital period in order to observe any transient behavior as well as steady state behavior.

www.manaraa.com

Table 5.2: List of Thesis Orbit Trade Study

Initial Orbit Parameter	Value
Start Epoch	02/25/2017 00:00:00.000 UTC
Experimental Period	3 days
SMA	6678 km - 42158 km (LEO to GEO)
ECC	0.0 - 0.8
INC	0 - 180 degrees
AOP	0 - 360 degrees
RAAN	0 - 360 degrees
TA	0 degrees

The minimum orbital period is 5400 seconds, with the largest orbital period being 86400 seconds (1 day). A three day experimental period was chosen to observe steady state behavior of XNAV performance.

The rest of the chapter will describe models used within the orbit design and the XNAV measurement process seen in Figure 5.1. The first section will focus on the preliminary orbit design and pulsar information required for XNAV. That section of the simulation is shown in Figure 5.3.

www.manaraa.com

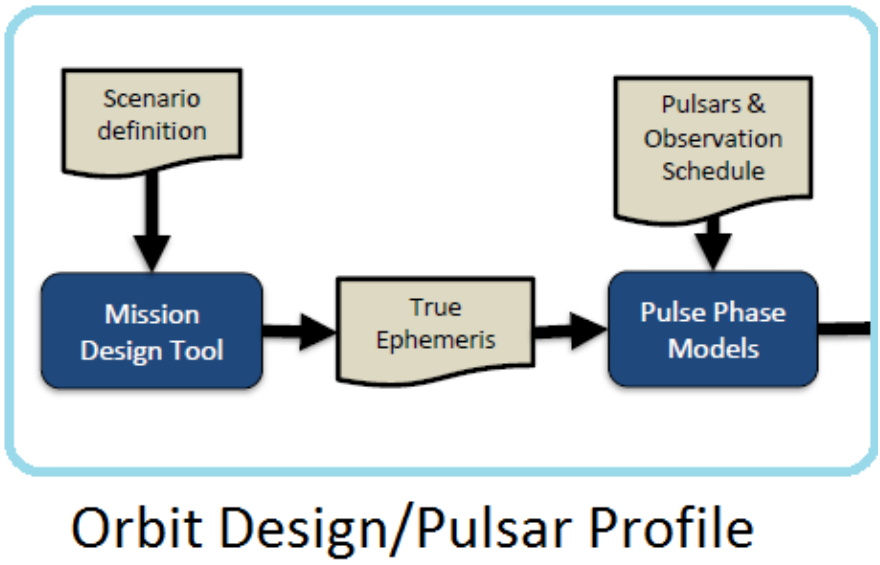

Figure 5.3: Thesis Simulation: Orbit Design/Pulsar Profile Information for XNAV

5.3 Pulsar Visibility

An XNAV measurement is based on collecting photon TOAs. This process requires an observation time on each pulsar based on the CRLB reviewed in chapter 3. Due to the significant observation time, the XNAV process is subject to physical blockages between the detector and the pulsar. This thesis checks for occultations for each truth ephemeris time step, detailed below. The data is generated in the orbit design/pulsar profile section seen in Figure 5.3. This thesis models occultations from celestial bodies and areas of highly variable background radiation.

The driving occultations are celestial body occultations. This thesis models occultations from the Sun, Earth, and Moon. See Figure 5.4. For this diagram, the instantaneous angle calculated per propagation step is calculated between the pulsar/spacecraft detector/celestial body center (α) and an angle between the celestial

www.manaraa.com

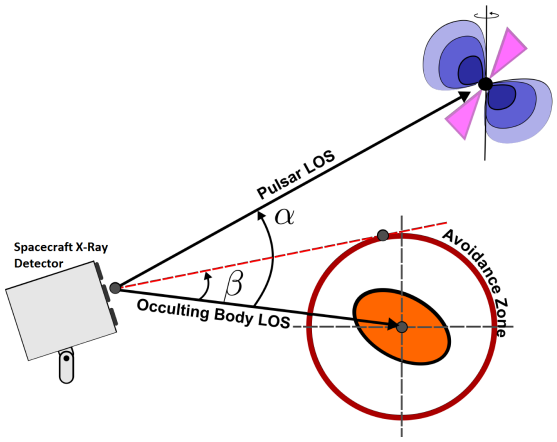

Figure 5.4: Celestial Body Occultation Model

body center/spacecraft detector/tangential intersection with a spherical avoidance zone (β). These angles are not the same as the variables used to define the total photon count rate in chapter 3; they are only angle definitions for this diagram and are not used anywhere else in this thesis. The lines drawn are based on the instrument boresight/Line of Sight (LOS). The avoidance zone is a spherical volume around the celestial body that is dependent upon the amount of energy reflected or emitted by that object. The conservative angles that were used as the avoidance zones in this thesis were 45° for the Sun, 30° for the Earth and 15° for the Moon, based upon any interference with operating the X-ray detector instrument. Finally, celestial body ephemeris were referenced from the JPL Spacecraft Planet Instrument C-matrix Events (SPICE) database [1].

As the experimental period is three days, a particular start epoch needed to be found in order to ensure that all pulsar targets were available for the experimental period. From Figure 3.9, solar occultations have an annual influence that can eliminate a pulsar target with a low ecliptic latitude for months at a time. Lunar

www.manaraa.com

influences can occur monthly in relation to the lunar orbital ecliptic around the Earth. The thesis pulsar visibility is seen in Figure 5.5 by truncating Figure 3.10.

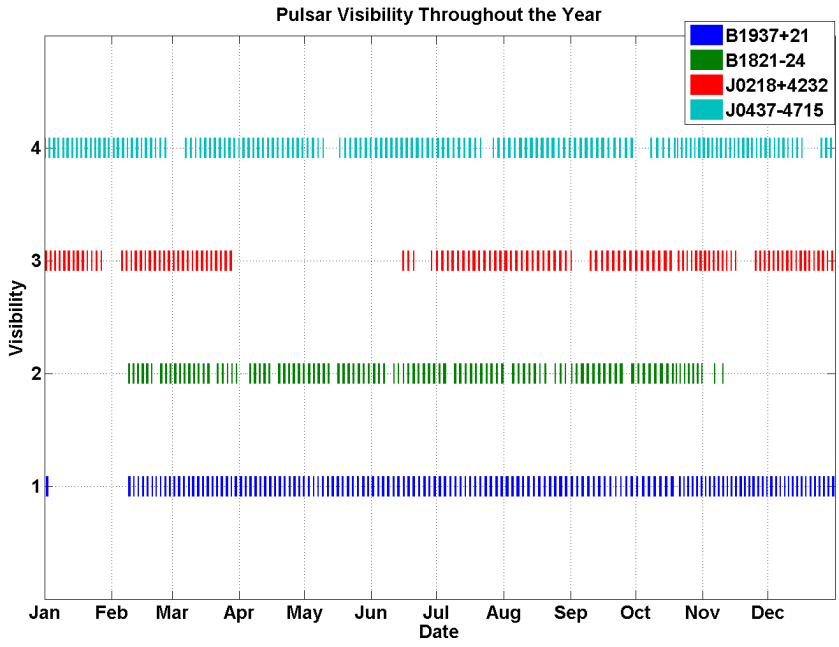

Figure 5.5: Visibility of Thesis Pulsars in LEO throughout the Year

The x axis of Figure 3.10 are months throughout the year. The y axis represents each pulsar. Over time, the colored lines indicate that the pulsar is visible. If the line is broken, the pulsar is occulted for that period of time.

Large occultations occur because of the sun. These solar occultations can be seen in Figure 3.10 for months at a time. Solar occultations have a direct relationship to a pulsar's galactic latitude, as seen in Figure 3.9. Pulsars B1937+21 and B1821-24 have the largest solar occultations in the winter time frame. Their galactic latitude is +/- 30°off from the Earth's orbit plane around the Sun. Because of this lower range in latitude, solar occultations are significant for these pulsars. On the other

www.manaraa.com

hand, J0437-4715 has a galactic latitude magnitude of greater than 60°. The galactic latitude is larger, so it does not experience any solar occultations throughout the year. Finally, pulsar J0218+4232 has an occultation similar in latitude to B1937+21. In the process, it has a solar occultation that occurs in the late spring/early summer time frame.

Lunar occultations are dependent on the relative geometry between the lunar orbit plane around Earth and the inertial directions of the pulsars. The small white occultations seen in Figure 5.5 are from lunar occultations. Based on lunar and solar occultations, the first period that all four pulsars appear visible and available is in late February.

Unlike solar and lunar occultations, Earth occultations are highly dependent on the orbit trajectory and will occur year round. Earth occultations occur daily and are dependent on the spacecraft's orbital period and radial distance from Earth. This can be seen in Figure 5.6.

www.manaraa.com

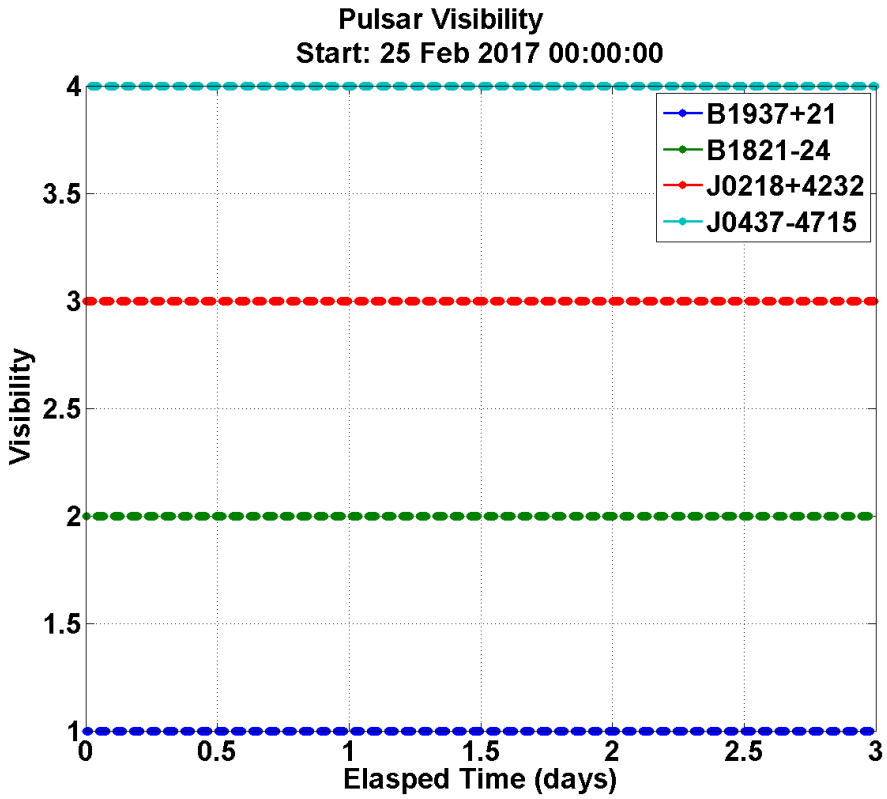

Figure 5.6: Visibility of Thesis Pulsars in LEO during the Experimental Period

As seen in Figure 5.6, the visibility of each pulsar can be seen for an example LEO. The natural orbit design varies this availability across different parts of the natural orbit, changing the overall nature of XNAV measurement frequency and the immediate spacecraft dynamics during the measurement time. A visual graphic of the pulsar availability from a spacecraft state can be seen in Figure 5.7. There is a pulsar visible at all times in the LEO scenario, even with the orientation of the four pulsar targets and more importantly, lunar and solar occultations do not influence the three day trade space used with XNAV.

Another area of occultation applied in this thesis were areas with highly variable background radiation. Areas with too variable of a background rate in the

www.manaraa.com

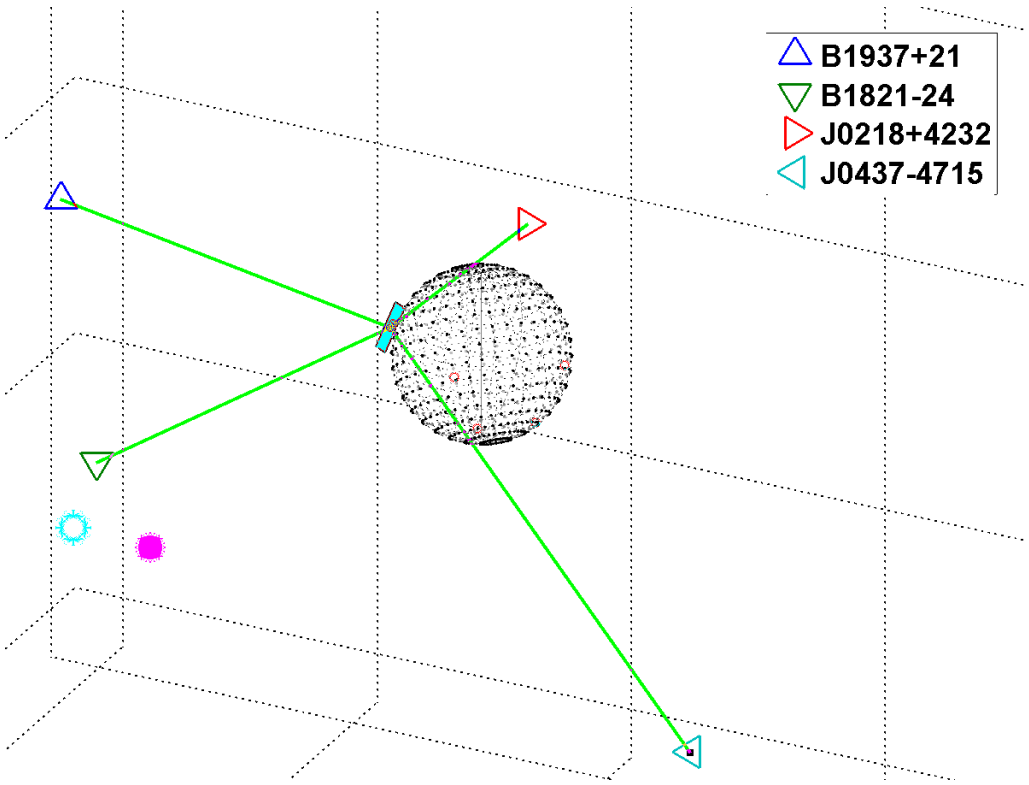

Figure 5.7: Graphic of Pulsar Visibility around Earth. Lines are drawn in the pulsar unit direction from the spacecraft. The two circles represent the Sun (magenta dot) and the Moon (cyan circle) unit directions.

spacecraft's immediate area were considered occulted. Large variations of radiation were considered a risk for the X-ray detector. Further study of X-ray detector hardware is required to confirm this, but this thesis treats them like physical occultations. The South Atlantic Anomaly (SAA) at orbit altitudes around 300-1000 km as well as areas around the magnetic north and south poles have this variation in background radiation(see Figure 5.8).

To avoid these areas, the SAA and areas around the magnetic poles are restricted by a longitude/latitude box. For the SAA it is only applied at orbit altitudes

www.manaraa.com

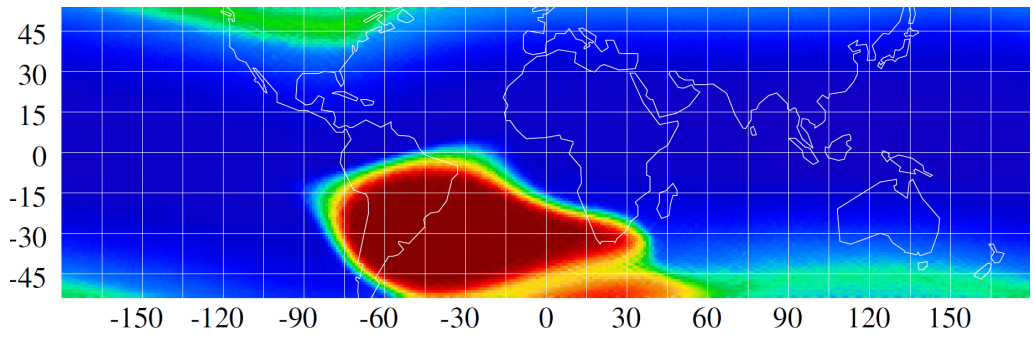

Figure 5.8: Background Radiation Environment around 400 km altitude versus Geodetic Longitude/Latitude (degrees). Note the high concentration areas around the South Atlantic as well as the magnetic poles [42].

between 300-1000 km, while the magnetic pole areas are enforced for any orbit altitude. With these background occultations, all the pulsars are considered occulted when the spacecraft orbit enters these regions. The geometry used for these structures comes from the National Oceanic and Atmospheric Administration (NOAA) geomagnetic map reference [14] [44].

The last occultation is related to background radiation. The areas stated earlier are considered occulted, but they are for areas of highly variable background radiation. The general modeling of background radiation is needed to simulate photons. This is described in the next section.

5.4 Background Radiation Environment

As stated in the photon TOA section of chapter 3, the background radiation environment has an influence on the XNAV measurement process. This section reviews how that parameter is modeled for the entire orbit trade space.

www.manaraa.com

The Earth's background radiation environment is a dynamic structure based on Earth's changing magnetic field. It is a result of the high energy interaction between the solar wind and the Earth's magnetosphere which redirects that energy. The dominating radiation structures around Earth are the Van Allen belts – two bands of high energy levels that exist within 10 Earth radii around the Earth [50].

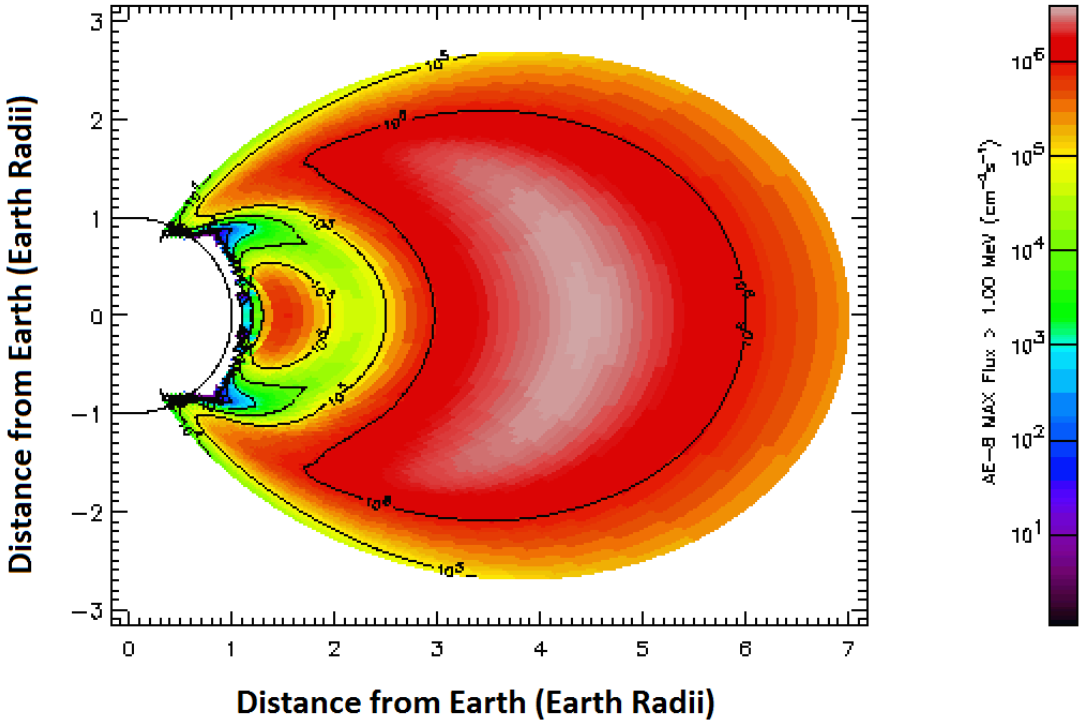

Figure 5.9: Background Radiation Electron Environment from the Earth surface to 7 Earth Radii. Heat plot is scaled for electron flux greater than 1 MeV. Uses Data from the AE-8 model at solar maximum [24].

As seen with this high energy map in Figure 5.9, two areas between 1-2 Earth radii and 3-5 Earth radii have significantly higher concentrations of electrons than

www.manaraa.com

other areas. This map is based on empirical data [24]. In order to correct for more recent changes in the background radiation environment, researchers either model parameters that include or do not include individual solar events. Singular Solar events such as the "Halloween" solar storm of 2003 [4] or changes in the SAA [30] are common examples. Beyond the Van Allen Belts, the behavior of Earth's magnetosphere varies significantly between these models [24] [50].

With the significant variation in background environment, this thesis models the background environment based on the primary Van Allen Belt structures. See Figure 5.10 for a logarithmic plot used in the thesis. The horizontal axis is the spacecraft altitude at the equator in Earth radii, while the vertical axis represents the AE-8 model of electron flux at solar maximum that is greater than 100 MeV per centimeter squared seconds. A reference electron flux is marked in the simulation at 0.1 Earth radii. The other values on the plot are scaled relative to the flux at that value. The simulation provides the scaled energy level values directly into the photon simulation process. For a given spacecraft state from the truth ephemeris, a corresponding amount of background radiation is applied to the photon simulation and navigation measurement generation.

This application makes the assumption stated in past chapters that the hardware will be able to handle these environments and provide appropriate background rejection in order to effectively detect X-ray photon arrivals from individual MSP sources.

www.manaraa.com

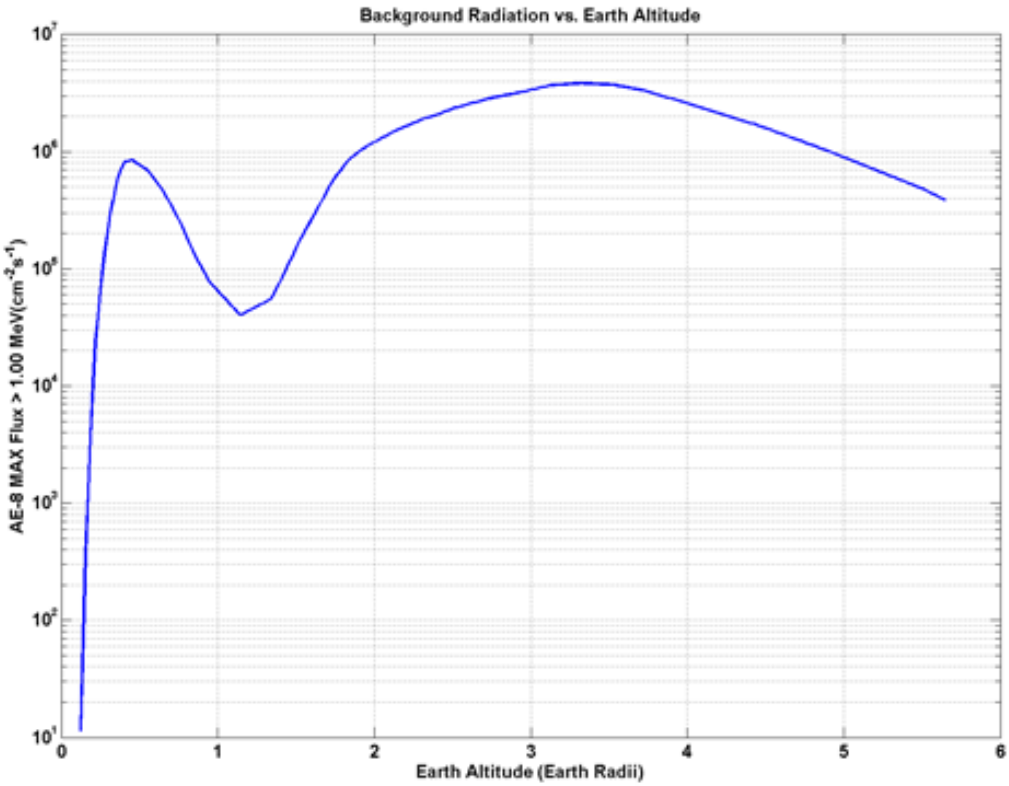

Figure 5.10: Background Radiation Electron Environment versus Distance from Earth. Uses Data from the AE-8 model at solar maximum [51].

5.5 Pulsar Observation Scheduling

In order to receive pulsar X-ray photons, observations of individual pulsars need to be prioritized to ensure that measurements are effective for XNAV. With the hardware assumptions built into this thesis, this also requires that one pulsar is observed at a time and that the schedule is produced before the EKF solution is simulated.

To generate a schedule, the scheduling process ingests a simulated ephemeris and a file that details the visibility of each pulsar for each ephemeris time step. As

www.manaraa.com

seen in Table 3.4 and Figure 3.12, a specific amount of observation time is required on each pulsar in order to assert enough photons have been detected for a pulsar phase/frequency measurement. Note that with hardware assumptions, this means that the observation of one pulsar is at the cost of the other pulsars.

With the ingested information, the schedule traverses forward in time through the data and schedules observations on each pulsar. The schedule does not follow a traditional optimization problem to decide on observations. This formulation solves a local problem by scheduling on a measurement by measurement basis using a local greedy heuristic [15]. It is a practical metric that is used to determine the next local XNAV measurement. While not an optimization formulation, it is a local method that is sufficient to minimizing state estimation error. This process is described in Figure 5.11. Once the local observation schedule for the next measurement is defined, the process repeats until the full schedule is realized.

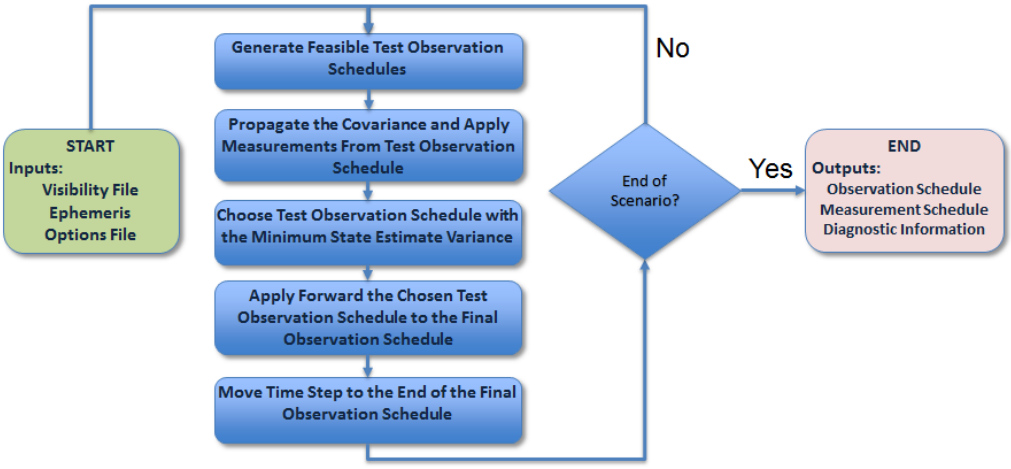

Figure 5.11: Pulsar Scheduling Flow Diagram

The following details the blocks in Figure 5.11. The first section goes into the

www.manaraa.com

generation of feasible test observation schedules. The second section goes into the covariance analysis and the metric used to determine which feasible test schedule is chosen for pulsar observation.

5.5.1 Generating Observation Schedules

From the initial start time and subsequent measurement times afterwards, the algorithm maps out possible observation schedules and then chooses one to build the final observation schedule. A possible observation schedule is created for each pulsar in the thesis. Each possible pulsar schedule is built using the local greedy heuristic seen in Figure 5.12.

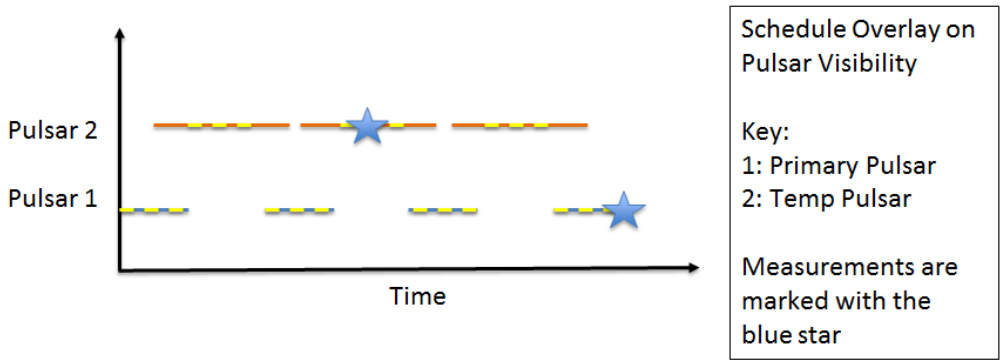

Figure 5.12: Example of a Pulsar Schedule Overlay to a Visibility Plot

As seen in the figure, the local greedy heuristic is a rule of thumb that attempts to observe the primary pulsar and achieve a measurement as soon as possible. If it is occulted, the pulsar with the smallest observation time based on the CRLB is chosen instead, called the temporary pulsar. The temporary pulsar may have enough observation for a measurement, but not always. Once possible schedules are made, they are evaluated and chosen to build the final pulsar observation schedule.

www.manaraa.com

5.5.2 Evaluating Observation Schedules

Once these observation schedules are created, each set of measurements is tested using a covariance based analysis. This is done with a state transition matrix (Φ) created from the ephemeris data. With a state transition matrix and a simulated state ephemeris at time t_0, the previous covariance P_{i-1} is propagated with Equation (2.35) in chapter 2.

$$P_i^- = \Phi(t_0, t_i) P_{i-1} \Phi(t_0, t_i)^T \tag{5.1}$$

Once the covariance is propagated to the measurement time (P_i^-), a Kalman gain is updated based on the covariance. This also uses the relevant measurement noise from the pulsar R_i as well.

$$K_i = P_i^- H_i^T [H_i P_i^- H_i^T + R_i] \tag{5.2}$$

Finally, the covariance is updated with the given measurement.

$$P_i = [I - K_i H_i] P_i^- \tag{5.3}$$

If more than one measurement was made with a given observation schedule, the process is repeated until the last measurement is made. Each covariance from each observation schedule now represents the uncertainty of the state estimate based on each new measurement.

Based on past research [10] [9], the current criteria of this scheduling algorithm is to minimize the projected SMA variance. This primary objective drives the scheduling algorithm for the thesis. To do so, one must take the components of the

www.manaraa.com

covariance solved for each pulsar observation schedule and solve for the SMA variance. This is done with a partially differentiated vis viva equation (Equation (2.12)) with respect to r and v. Once the observation schedule is selected, it is compiled into the final observation schedule. An example schedule product can be seen in Figure 5.13.

$$\delta r = \frac{1}{2}\left[\frac{(2\mu - rv^2)^2}{\mu^2}\right]\delta a \tag{5.4}$$

$$\delta v = \frac{1}{2}\left[\frac{(2\mu - rv^2)^2}{\mu r^2 v}\right]\delta a \tag{5.5}$$

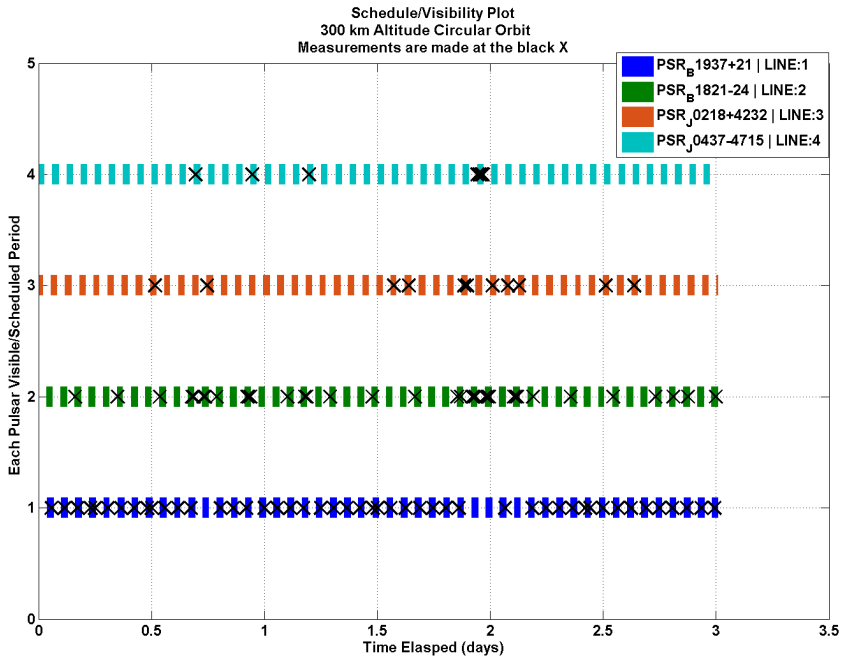

Figure 5.13: Example of a Pulsar Schedule Overlay to a Visibility Plot

The horizontal axis represents the elapsed time in days. The vertical axis shows the visibility plot as seen in earlier sections, with each line representing the

www.manaraa.com

visibility of each pulsar. Observations are scheduled in a separate color on top of these visibility periods, shown in cyan. Finally, the black X indicates where a pulsar measurement from that pulsar is generated.

This formulation has been sufficient to provide convergent navigation solutions in closed two-body orbits. In the general case, this objective function has a significant amount of complexity that is similar to dynamic programming job-shop telescope scheduling problems [8] [34]. As the choice of observing one pulsar must be made, the observation of one pulsar changes the optimal use of the other pulsars. Also included in the general formulation are both discrete and continuous constraints. Visibility periods are discrete, while many of the metrics used in modeling spacecraft dynamics and navigation can be continuous. This thesis approaches this problem with a simplified heuristic, but more work can be made within this area to better characterize the scheduling problem.

Separate from scheduling, the next section elaborates on how the photons are simulated and the phase is formally estimated for the measurements model to the EKF. Further reading can be found at [53].

5.6 Simulate XNAV Measurements

The end goal of creating navigation XNAV measurements is to estimate a range distance between the Earth and the spacecraft at a particular epoch. As stated in chapter 1, this is determined by comparing a signal at a spacecraft X-ray detector versus the expected signal at Earth. In chapter 3, the pulsar X-ray

www.manaraa.com

signal was described as a phase within a periodic cycle of X-ray wave fronts. This chapter describes how the simulation takes the information from chapter 3 and generates the information described in chapter 1. This information is called the XNAV measurement.

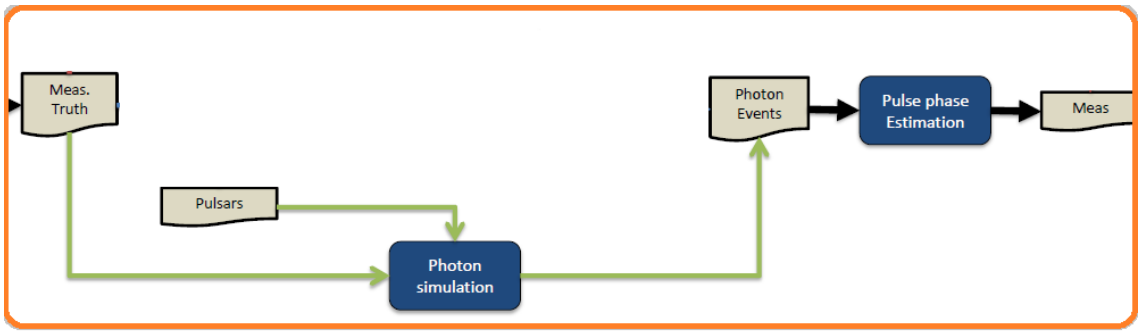

Figure 5.14: Thesis Simulation: XNAV Measurement Generation with the Thesis Path

To create the XNAV measurement, the simulation calculates the phase difference between Earth and the spacecraft. This equates to the range difference due to light time delay. The simulation starts with the given estimate state from the EKF and the reference timing model. This simulation uses a reference called TEMPO2, a pulsar timing model package. The software fits empirical radio observations of pulsar targets and calculates the phase/frequency of a pulsar signal at a reference state [31]. With a given state from the EKF and TEMPO2, a first order phase difference is revealed. However, the dynamics of the spacecraft causes higher order behavior in phase evolution that is unique to the spacecraft trajectory. This be-

www.manaraa.com

havior is inherently embedded in each detected X-ray photon TOA. A correction is then required using detected X-ray photon TOAs.

Photons are collected and time tagged and the information is correlated to the expected pulsar count rate from a database. The simulation then calculates the phase/frequency correction that correlates to the incoming photon data. That process is described in this chapter with two parts: the estimation of the pulsar phase/frequency and the XNAV measurement model. The design of the pulsar measurement model is discussed in detail in [54]. Background on pulsars used in this chapter can be found in chapter 3.

5.6.1 Differenced Phase and Frequency Estimation

As stated earlier in this chapter and in chapter 3, this section and the section on the XNAV measurement model are an explanation based on reference [54]. The thesis did not create this process. The thesis uses this process to produce XNAV measurements. The terminology used in this section come from both chapter 3 and chapter 2. The goal of this section is to calculate the difference in phase/frequency between Earth and the X-ray detector.

With the previous assumptions from chapter 3, the phase at the detector ϕ_{det} is modeled as:

$$\phi_{det}(t) = \phi_0(t - \tau(t)) \tag{5.6}$$

where ϕ_0 is the calculated phase at the reference location (Earth center).

www.manaraa.com

TEMPO2 software is used to quickly reference ϕ_0. The software holds piecewise polynomial approximations of the full timing model [31]. $\tau(t)$ represents the propagation time that the photon has between the detector's location and the reference location at the speed of light c. It is defined as follows:

$$\tau(t) = \frac{\vec{x} \cdot \hat{n}}{c} \tag{5.7}$$

where $\vec{x}$ is the general spacecraft position and $\hat{n}$ is the unit vector in the direction of the pulsar. This is the basis which the measurement model is ascertained. It assumes that the spacecraft is in an Earth orbit. If the origin is significantly farther away from Earth, the addition of timing delays due to relativistic effects and parallax must be included.

The objective of simulating an XNAV measurement is to estimate both parameters in Equation (5.6). The parameters are used with the TEMPO2 phase estimate at Earth (ϕ_0) to calculate the phase/time difference between photon arrivals at Earth and at the spacecraft. This equates to the Earth range of the spacecraft.

The previous equation demonstrates a relationship between the pulsar phase at the detector and Earth. Expanding the detector phase model by substituting τ and the EKF state estimate $\hat{\vec{x}}$:

$$\phi_{det}(t) = \phi_0(t - \frac{\vec{x} \cdot \hat{n}}{c}) \tag{5.8}$$

$$= \phi_0(t - \frac{\hat{\vec{x}} \cdot \hat{n}}{c} + \frac{\delta\vec{x} \cdot \hat{n}}{c}) \tag{5.9}$$

$$\simeq \phi_0(t - \frac{\hat{\vec{x}} \cdot \hat{n}}{c}) + \dot{\phi}_0(t - \frac{\delta\hat{\vec{x}} \cdot \hat{n}}{c})\frac{\delta\vec{x} \cdot \hat{n}}{c} \tag{5.10}$$

$$=: \hat{\phi}(t) + \dot{\phi}_0(t - \frac{\delta\hat{\vec{x}} \cdot \hat{n}}{c})\frac{\delta\vec{x} \cdot \hat{n}}{c} = \hat{\phi}(t) + e(t) \tag{5.11}$$

www.manaraa.com

where $\delta\vec{x}(t) = \hat{\vec{x}}(t) - \vec{x}$.

As stated earlier, the photon TOAs are used as a correction to the initial phase offset from TEMPO2. This offset is represented in this specific section as the function $e(t)$ from Equation (5.8). The assumed model for e(t) for short observation intervals is:

$$e(t) \simeq q + f(t - t_a) \tag{5.12}$$

The variables q and f are constants that need to be estimated. Once estimated, the values can be used to correct the phase estimate. The maximum likelihood formulation is used in this context with the following steps:

1. Observe the arrival times of photons $t_k{}_{k=1}^{N}$ during a fixed interval of time $[t_a, t_b]$.

2. Using Maximum Likelihood Estimation (MLE), calculate estimates $(\hat{q}, \hat{f})$

3. Use these values to estimate the phase as well as Doppler of the pulsar profile: $\hat{\phi} = \hat{\phi(t)}^{-} + \hat{q} + \hat{f}(t - t_a)$ and $\dot{\hat{\phi}} = \hat{f}$

And the formal definition of the MLE is below:

$$(\hat{q}, \hat{f}) = \underset{q,f}{\operatorname{argmax}} \sum_{k=1}^{N} \log \lambda(\hat{\phi}(T_k)^{-} + q + f(T_k - T_a)). \tag{5.13}$$

The $-$ superscript indicates the previously estimated value of ϕ is used to calculate the upcoming estimate phase and Doppler shift. Once the phase and Doppler shift is estimated, these values are processed to make the phase estimate and the measurement model.

www.manaraa.com

5.6.2 XNAV Measurement Model

With the phase offset estimated from Equation (5.6), $\tau(t)$ from that equation relates the phase offset to a navigation measurement. Defined in the previous section, the value $\tau(t)$ from Equation (5.6) and Equation (5.7) is the connection between estimating the phase difference and the navigation measurement. This section expands on that relationship for the XNAV measurement model used in the EKF. All this information is a summary from reference [54] as it is used in this thesis.

The measurement model represents the state as well as the first order partial derivatives of the state. In this case, the state includes the phase of the pulsar profile and the frequency. As the phase with pulsar information is sufficient to get a first order range estimate, the earlier definition of phase is applicable. Once these measurements are generated, they are directly passed into the EKF for processing. The NASA software GEONS is used to implement the state estimation and the filter for the final output product.

$$\phi(t) = \phi_0(t - \frac{\hat{n} \cdot \vec{x}(t)}{c}) \tag{5.14}$$

The frequency is obtained by differentiating (5.14), leading to

$$\dot{\phi}(t) = \dot{\phi}_0(t - \Delta(t)) \left[1 - \frac{\hat{n} \cdot \dot{\vec{x}}(t)}{c}\right], \tag{5.15}$$

with $\Delta(t) = \hat{n} \cdot \vec{x}(t)/c$.

www.manaraa.com

The filter also requires the first order partial derivatives which are given by

$$\frac{\partial \vec{y}}{\partial \vec{z}} = -\frac{1}{c}\begin{pmatrix} \dot{\phi}(t-\Delta(t))\hat{n}^T & 0 \\ (1-\ddot{(}t))\dot{\phi}(t-\Delta(t))\hat{n}^T & \dot{\phi}(t-\Delta(t))\hat{n}^T \end{pmatrix}, \tag{5.16}$$

with $\vec{y} = (\phi, \dot{\phi})^T$ and $\vec{z} = (\vec{x}, \dot{\vec{x}})$.

5.6.3 Phase Ambiguity Resolution

XNAV Measurements created within the photon simulation are predicated on using an MLE. Ideally, the photon TOA information should stay contiguous and encompass the periodic dynamics of a closed Earth orbit. If there are multiple smaller peaks in the pulsar lightcurve profile or a significant amount of background radiation / occultation, the resultant phase and frequency may find the wrong peak and/or be off by too many phases. This is called phase cycle ambiguity [56], as the phase correction created using the photon TOAs are significantly off nominal from the phase estimate in the TEMPO2 software. If an XNAV measurement is used, it will hurt the navigation filter with corrupted timing information.

In this formulation, a measurement tolerance based on the CRLB bounds the acceptable measurements for the EKF filter. Stated in chapter 2, the CRLB definition is the definition of the EKF measurement noise matrix. Measurement phase residuals that are too noisy are discarded. The time difference in Equation (3.15) can be translated into a phase difference (equal to 1σ) due to light time delay. When the phase is estimated in the earlier section, it is differenced with the reference phase calculated from the TEMPO2 reference software. This produces the measurement phase residual. If the residual is greater than 3σ, the measurement is edited out.

www.manaraa.com

This is the common result of XNAV measurements with pulsar observation breakup and significant background radiation.

www.manaraa.com

Chapter 6: Orbit Characterization Results

The results of the simulation are reviewed in this chapter. The study first observes individual cases to describe the overall nature of the results. It then demonstrates the influences of each Kepler orbital element on XNAV tracking performance. Finally, it studies the first order influence of changing Kepler elements.

The trade study varies the initial orbit of the spacecraft in semi-major axis (SMA), eccentricity (ECC), inclination (INC), argument of periapsis (AOP), and right ascension of the ascending node (RAAN). The addition of orbit true anomaly (TA) would complete a full definition of the spacecraft initial state. This thesis chose to focus on the orbit geometry(shape and orientation) and not the spacecraft's state itself. There is potential future work in adding the orbit anomaly as well, which would add further insight on its influence on initial XNAV measurements.

6.1 Individual Case Performance

To evaluate XNAV tracking performance across this trade space, four post-processing areas were chosen.

Visibility is a critical resource for generating XNAV measurements, so it is represented in Table 6.1. If the breakup in visibility is too great, the collection

www.manaraa.com

المنارة للاستشارات

Table 6.1: List of Thesis Post Processing Metrics for a Single Orbit

Metric	**General Definition**
Pulsar Visibility	Amount of Time a Pulsar is Visible to the Detector
Measurement Quality	The Estimated Phase based on the X-ray Photon TOA - The Expected Phase from the TEMPO2 reference
Definitive State Error	Truth State - Estimate State
Definitive SMA Error (Provides Predictive Accuracy)	Definitive State Error Projected into SMA by Equation (2.12).

www.manaraa.com

of photon TOAs are broken up over multiple periods of visibility. These photon TOAs attempt to carry information about the spacecraft dynamics. If they are too broken up, they lose their value in the phase estimation process explained in chapter 5. The ideal visibility for XNAV would allow photon TOAs to be collected in one continuous period. The photon TOAs would span a period of time where the spacecraft's average velocity would be minimal.

Measurement quality is a metric that evaluates the resultant XNAV measurements. As mentioned in the phase ambiguity section of chapter 5, measurements that have a phase over an expected 3σ bound are edited out. This is calculated by differencing the expected phase from the TEMPO2 software with the estimated phase using photon TOAs at the X-ray detector. If the correction is too great, it is edited and removed from the EKF. The more edited measurements, the worse the XNAV performance. The indicators that influence this performance come from background radiation and from pulsar visibility, which the first post processing metric can confirm.

With the information about visibility and measurement quality, the actual performance of the EKF is summarized with the definitive state error. The definitive state error itself is the instantaneous difference between the truth state and the estimate state at each measurement time. The truth state comes from the propagator that created the orbit trajectory in Figure 5.3, while the estimate state is the calculated state from the EKF. Finally, that definitive state error is converted into semi-major axis error via Equation (2.12). It was used as a strong indicator of overall orbit determination convergence for the upcoming state performance [10].

www.manaraa.com

The common example used to describe the simulation testing procedure and the EKF settings has been a 300 km altitude circular equatorial orbit. This particular case's XNAV performance is detailed in Figures 6.2, 6.3, 6.4, and 6.5.

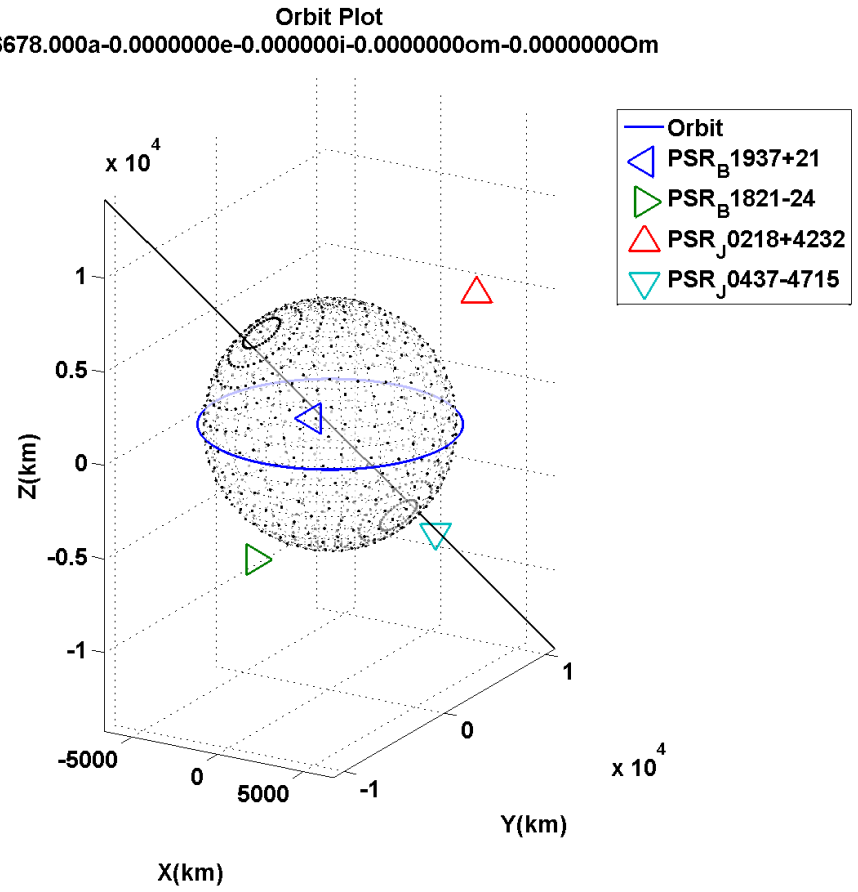

Figure 6.1: 300 km Altitude Circular Equatorial Orbit: ECI MJ2000 Orbit Plot. Pulsar unit directions are represented. The line through the Earth is the Earth's magnetic axis.

www.manaraa.com

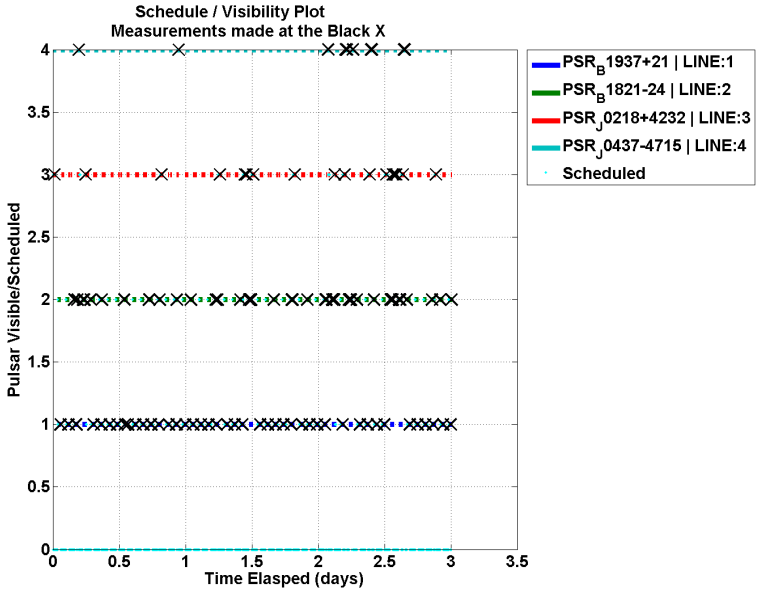

Figure 6.2: 300 km Altitude Circular Equatorial Orbit: Visibility/Scheduling of Pulsars

Visibility and the chosen schedule for this LEO is represented in Figure 6.2. The horizontal axis is the time elapsed and the vertical axis has each pulsar and its visibility marked throughout the experimental period. The black x indicates a pulsar measurement chosen for scheduling. Note that for a LEO, there are about 16-17 orbits per day.

www.manaraa.com

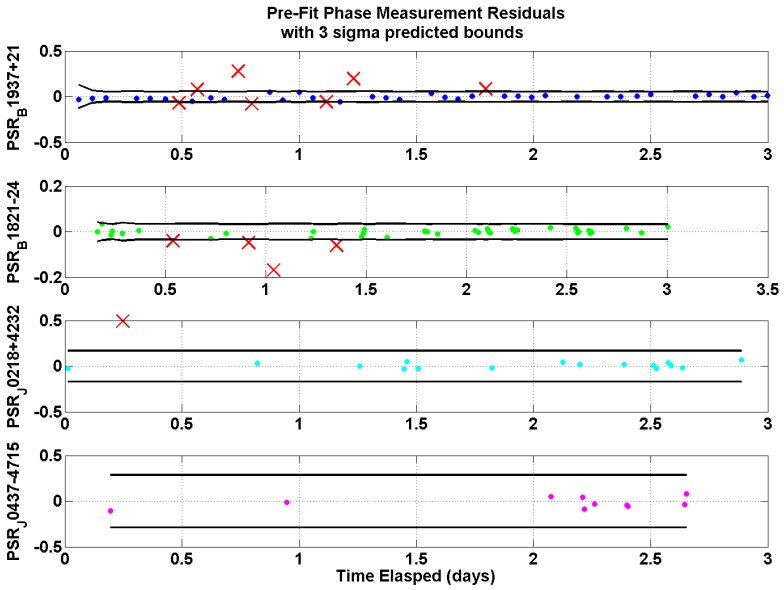

Figure 6.3: 300 km Altitude Circular Equatorial Orbit: Phase Measurement Residuals. A red X is a rejected measurement.

The phase residual plot used to judge measurement quality is seen in Figure 6.3. The horizontal axis is the time elapsed in the experimental period. Each subplot is for each pulsar, with the vertical axis representing the difference in phase between the nominal TEMPO2 software calculated phase and the estimated phase from photon TOAs. This corrected phase was explained in the phase estimation section of chapter 5. The black lines encompass the expected 3σ phase with the corrected phase. A red x indicates a rejected measurement. Next, the definitive state error is shown in two plots for magnitude and semi-major axis for Figures 6.4 and 6.5.

www.manaraa.com

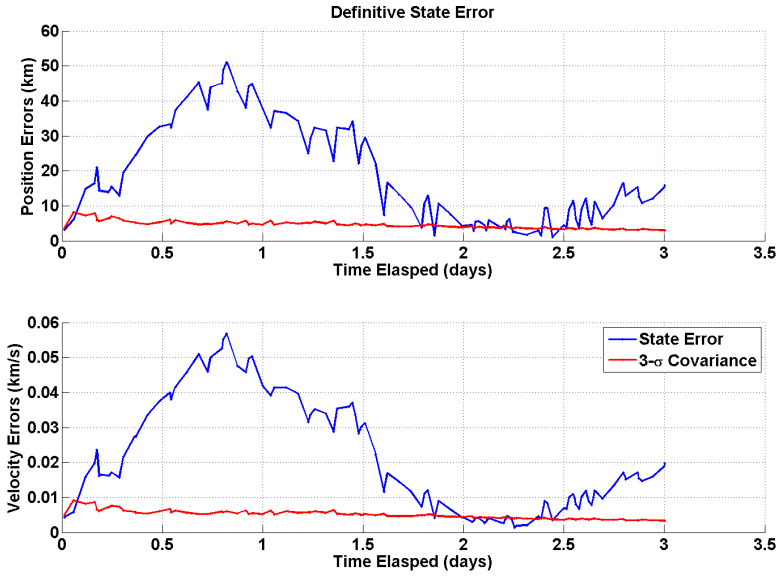

Figure 6.4: 300 km Altitude Circular Equatorial Orbit: Definitive State Error

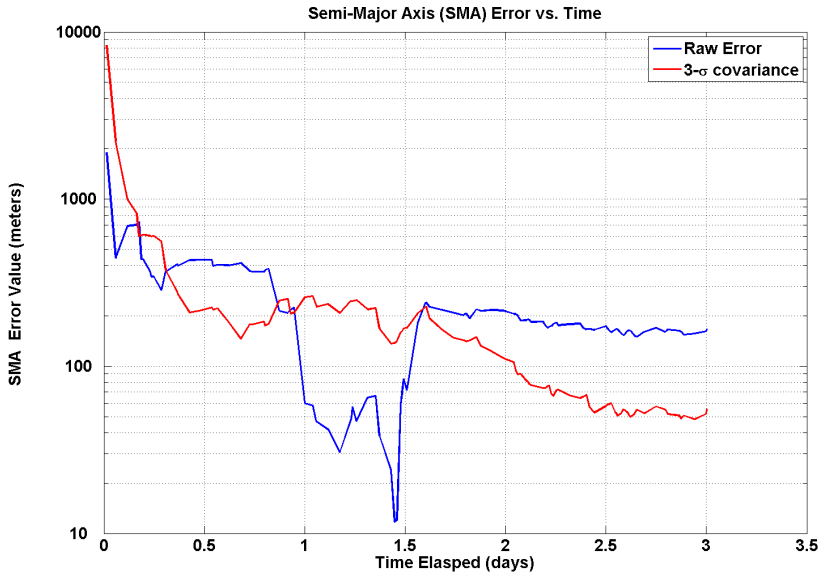

Figure 6.5: 300 km Altitude Circular Equatorial Orbit: Definitive semi-major axis Error

The state error is the difference between the truth and the estimate states of

www.manaraa.com

the navigation filter. The magnitude plots show both position and velocity error in km and km/s. The semi-major axis error plot vertical axis is the offset of semi-major axis truth and estimate in meters. The horizontal axis indicates the time elapsed in both of these figures. The red line indicates what the EKF filter estimates is the total error, based on the 3σ covariance. The blue line is the raw error itself.

As seen in both Figure 6.4 and 6.5, the spacecraft state estimate error exhibits a periodic behavior between 5-40 kilometers without any clear convergence. The filter covariance also does not bound most of the actual state error as it changes, so the filter has misinformation on the amount of state error in the scenario. Finally, a combination of edited measurement residuals seen in Figure 6.3 show a total of 101 measurements, with approximate 12% of them rejected.

This behavior is directly due to properties derived from the semi-major axis. The orbit period for this 300 km altitude orbit is about 5400 seconds (90 minutes). In terms of visibility, the approximate angle made with Earth that determines visibility seen in Figure 5.4 is about 100°. As the spacecraft is still within Earth's atmosphere, the range of pulsar visibility is greater than 90°. Finally, the orbit is circular and equatorial (eccentricity is 0 and inclination is 0°). This makes the definition of orbit angles argument of periapsis and right ascension of the ascending node undefined. While other orbit planes will precess over time due to J_2, this particular orbit will not. Even so, XNAV measurements are still made with observations over multiple orbits. This results in greatly deteriorated measurement information which hurts the navigation solution.

An orbit representation can be seen in Figure 6.1. The plot is in the MJ2000

www.manaraa.com

frame and shows the X,Y, and Z Cartesian axes with units of kilometers. The first set of measurements, due to slew time and availability, occur at about 20 minutes and then 85 minutes into the scenario. With an approximate 90 minute orbit period, that means that only two measurements were created in the first orbit. As seen, this lack of measurement information within an orbit does not allow the EKF to converge, but instead causes periodic behavior. In summary, the visibility and the short orbit period relative to the observation times in Table 3.4 eventually result in the overall inability to track in LEO.

To demonstrate a more stable solution, the increase of semi-major axis to a GEO greatly improves the overall performance of XNAV. XNAV performance is detailed in Figures 6.7, 6.8, 6.9, and 6.10.

www.manaraa.com

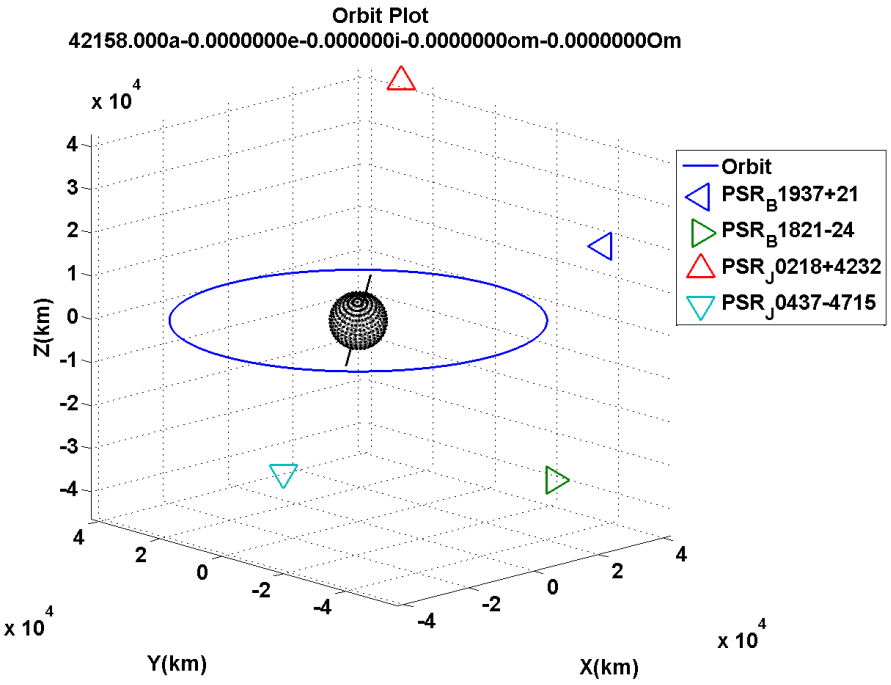

Figure 6.6: 35780 km Altitude Circular Equatorial Orbit: ECI MJ2000 Orbit Plot. Pulsar unit directions are represented. The line through the Earth is the Earth's magnetic axis.

www.manaraa.com

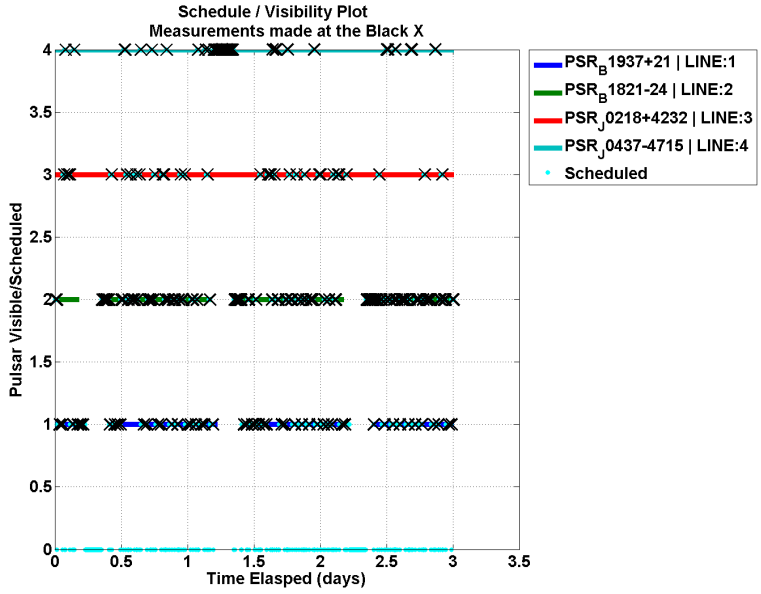

Figure 6.7: 35780 km Altitude Circular Equatorial Orbit: Visibility/Scheduling of Pulsars

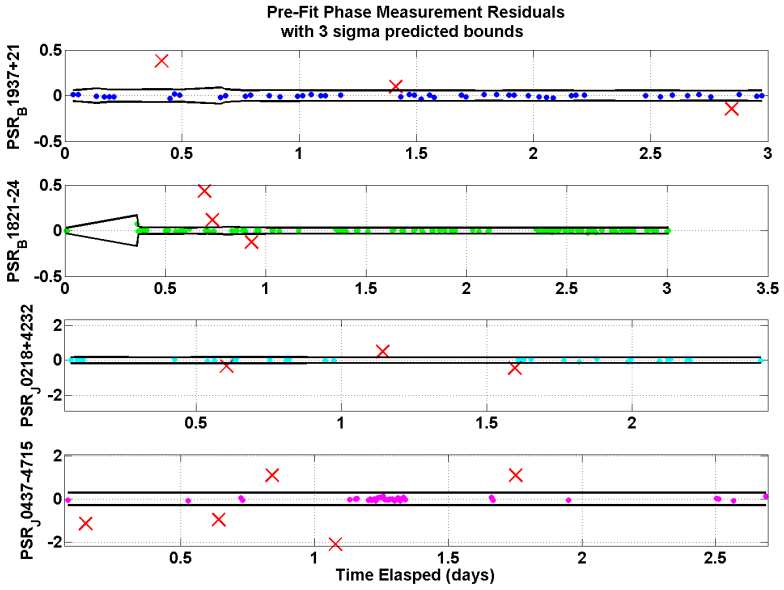

Figure 6.8: 35780 km Altitude Circular Equatorial Orbit: Phase Measurement Residuals. A Red X is a rejected measurement.

www.manaraa.com

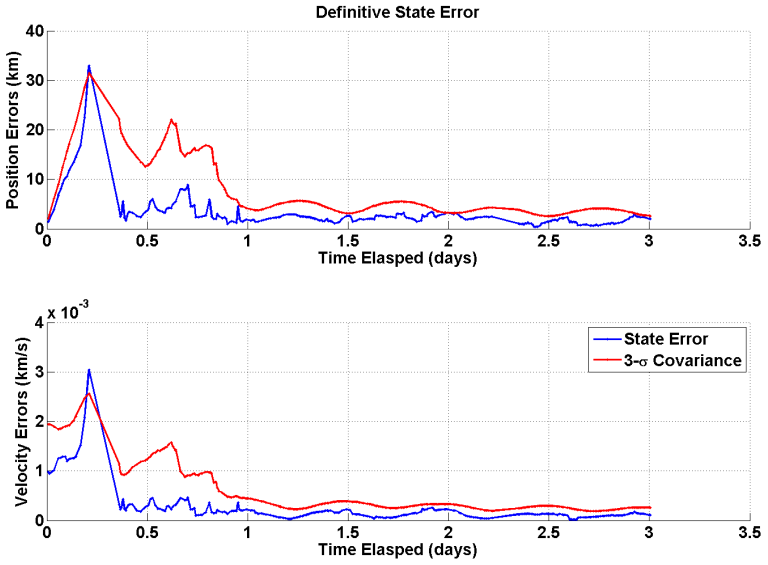

Figure 6.9: 35780 km Altitude Circular Equatorial Orbit: Definitive State Error

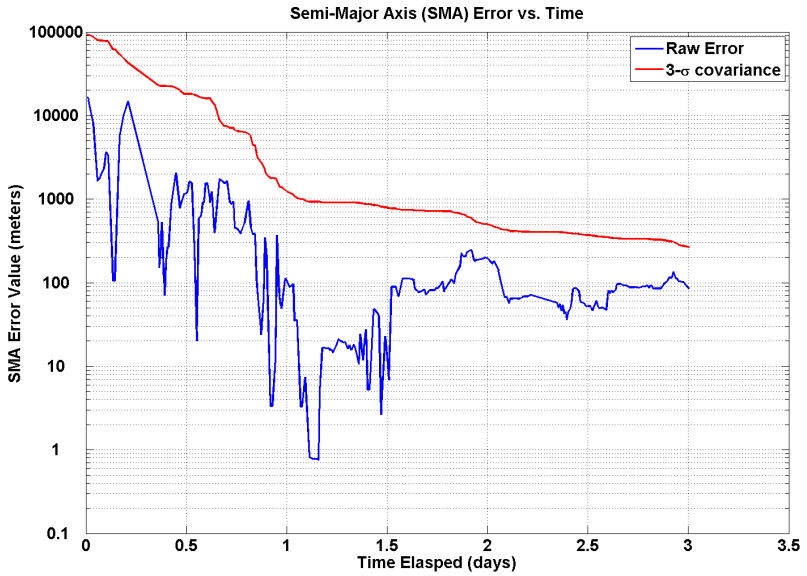

Figure 6.10: 35780 km Altitude Circular Equatorial Orbit: Definitive SMA Error

Seen in Figure 6.9 and 6.10, the increase in semi-major axis has allowed XNAV measurements to bring the orbit determination solution below 5 km RSS. Various

www.manaraa.com

parameters helped improve the overall XNAV performance. The orbital period is now 86400 seconds (or 1 day). Like the LEO case, the value of argument of periapsis and right ascension of the ascending node are undefined. About the same percentage of measurements were accepted by the EKF, but the total number of measurements have increased to about 250 throughout the three day scenario. This increases the amount of knowledge that the filter has on the state error through the measurements. The background radiation environment is also outside of the Van Allen belts as seen in Figure 5.10 and there are large periods of continuous pulsar visibility, with some having complete visibility throughout the three day scenario. The angle that the Earth makes with a GEO is closer to 40° instead of the 100° of a LEO. This increases the visibility for all pulsars as well as a greater frequency of measurements from all four pulsars.

Note that, though two other pulsars are always visible, periodically occulted pulsar B1821-24 is commonly scheduled for observation. Pulsar B1821-24 has the smallest observation time (600 seconds or 10 minutes) per measurement and also has the second best timing accuracy of the four pulsars as seen in Figure 3.12. As a result, the scheduling algorithm frequently schedules B1821-24 over the others. This is particularly important for the first few XNAV measurements. As seen in Figure 6.7, B1821-24 is used for the first two measurements at the 10 and 20 minute mark of the scenario, the shortest amount of time possible to observe two B1821-24 measurements.

www.manaraa.com

6.2 Single Kepler Element Variation

In order to better observe XNAV performance over a wider orbit design space, the metrics mentioned for the individual case performance are now summarized.

Shown in Table 6.2, the metrics are changed in order to observe variation across each orbit element. They allow one to observe XNAV tracking performance over multiple orbit designs. The following paragraphs go into further detail on each item in the table.

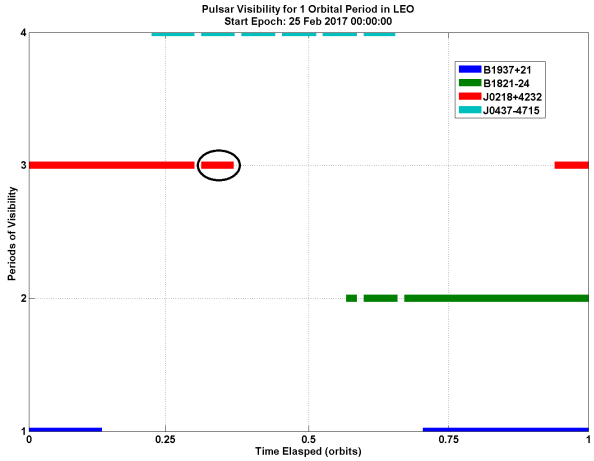

Figure 6.11: Example Visibility Plot of Pulsars for a LEO over one orbital period. A continuous period of visibility is circled in black.

The averaged definitive state error is the primary metric. The definitive state error is the state error difference measured at a specific time of the simulation. It is designated as definitive as it does not provide any information about the projected error growth of the filter estimation. Once calculated, this error is averaged over the final day of the simulation. This period was chosen to represent the steady state behavior of the state estimate. This averaged error parameter is also converted

www.manaraa.com

المنارة للاستشارات

Table 6.2: List of Thesis Post Processing Metrics for the Single Orbit Element Trade

Metric	**General Definition**
Pulsar Visibility Averages	Average Continuous Period of Visibility for the Entire Simulation and Average Visibility per Orbital Period for the Entire Simulation
Measurement Quality	Total Number of XNAV Measurements and the Percentage of XNAV Measurements Rejected
Definitive State Error Average	(Truth - Estimate Magnitude) / Total Number of Measurement Updates over the Final Day of Tracking
Definitive State Error SMA Average	(Definitive State Error Projected into SMA) / Total Number of Measurement Updates over the Final Day of Tracking.

www.manaraa.com

into the definitive error semi-major axis by using the position and velocity error in Equation (5.4) and (5.5).

Visibility is averaged in two different ways. The continuous visibility average is the average between every period of visibility that is unbroken by an occultation. An example of such a period is circled in Figure 6.11. This average was chosen to see if a pulsar XNAV measurement can be made within one visibility period. Any breakup in observations for a measurement results in a decrease in measurement accuracy, which increases the chance a measurement will be removed. The second visibility average is the average visibility per orbital period. As seen in Figure 6.11, the visibility per orbital period is summed over multiple periods of visibility. As demonstrated in chapter 2, a spacecraft orbit can precess over multiple orbits. Keeping the entire observation of a pulsar XNAV measurement to one orbit is beneficial to the XNAV measurement accuracy.

Measurement quality now uses two metrics: total number of measurements and percent of measurements removed. The total number of measurements is the total number of measurements that were generated in the simulation. The percentage of measurements removed records the ratio of rejected over total measurements due to the phase residual limits. Both numbers are needed to determine the total number of XNAV measurements used in the EKF. The total number of XNAV Measurements used in EKF equals the total number of XNAV measurements times the percent of edited measurements. The best case for XNAV tracking performance would be a large number of measurements and a small percentage of edited measurements. For this analysis, maximizing the number of used measurements is one way to improve

www.manaraa.com

the overall XNAV tracking performance.

One last thing to note is the influence of J_2 secular perturbations on an orbit plane. For the study of semi-major axis, eccentricity, and inclination, the other orbit parameters that are not varied are set to an equatorial and circular orbit. For a circular orbit (eccentricity is set to 0) the definition of argument of periapsis is invalid. Likewise for an equatorial orbit with an inclination at 0°, the definition of right ascension of the ascending node is undefined. This means that any J_2 orbit plane precession will be invalid for those angles. For the study of semi-major axis, both angles are undefined. For eccentricity and inclination, right ascension of the ascending node and then argument of periapsis are undefined, respectively. Finally, the study of argument of periapsis and right ascension of the ascending node are set to an orbit that will define both angles. This can be seen in Equations (2.14) and (2.15).

By making an orbit circular and equatorial, the influence of J_2 is separated between the variation of each orbital element. The change of the spacecraft orbit plane is then restricted to orbits which, by definition, should have secular out-of-plane orbit precession.

6.2.1 Variation of Orbit Semi-Major Axis

Looking first at semi-major axis, XNAV performance over varying semi-major axis is represented in Figures 6.13, 6.14, and 6.15. The nominal orbit parameters have an eccentricity of 0 and an inclination of 0°. As the orbit is circular and equa-

www.manaraa.com

torial, argument of periapsis/RAAN are not formally defined. For implementation into the simulation and with the GMAT software, they are defined at a value of 0°.

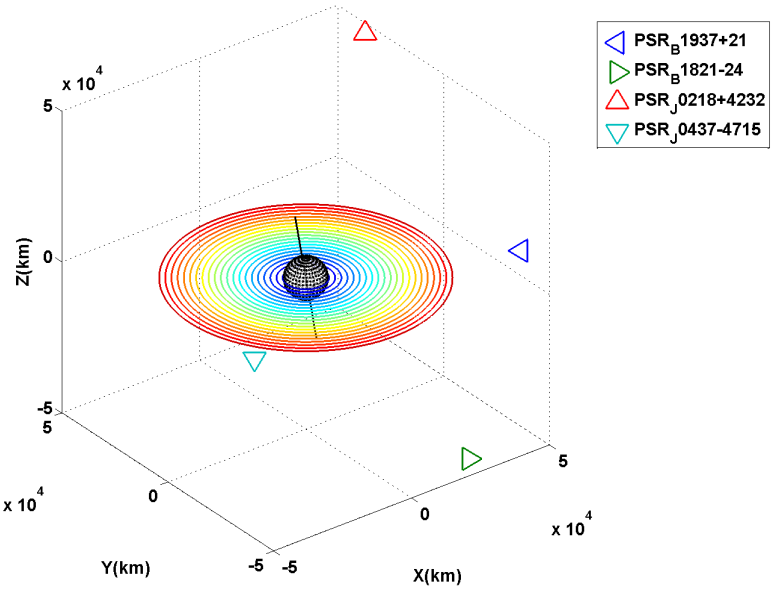

Figure 6.12: SMA Orbit Trade Space. Orbit trade value increases from blue (6678 km) to red (42158 km) for each trajectory.

The semi-major axis trade space is shown graphically in Figure 6.12 in the MJ2000 frame. The blue orbit is the smallest value of semi-major axis at 6678 km(LEO). The changing color of the orbit indicates an increase in semi-major axis. The red orbit is the maximum value of semi-major axis in the trade space, at 42158 km(GEO).

Changing semi-major axis modifies a couple of orbit parameters. The orbital period increases with the increase of semi-major axis. The trade study orbit periods range from 5400 seconds (90 minutes) to 86400 seconds (1 day). As this is a circular orbit, the orbit speed will be constant for this trade space. The circular

www.manaraa.com

orbit speed is inversely proportional to the semi-major axis. It ranges from 11 km/s to 4.3 km/s. Also, the angle used in Earth limb occultation is based on the spacecraft distance from the Earth geocenter. This angle decreases with spacecraft distance as seen between Figures 6.1 and 6.6. Also, as these orbits are all circular and equatorial orbits, there is no J_2 secular perturbation on the orbit plane itself. This means that the orbit argument of periapsis/RAAN are undefined and will not precess over time. Finally, the background radiation environment peaks at the Van Allen belts. As seen in Figure 5.9, the peaks of radiation are based on orbit radius. In this trade space, the orbit radius is directly determined by the orbit semi-major axis. The semi-major axis determines if the spacecraft will be orbiting in one of the Van Allen belts.

As seen in Figure 6.13, 6.15, and 6.14, the four post processing metrics for this section are shown versus semi-major axis.

www.manaraa.com

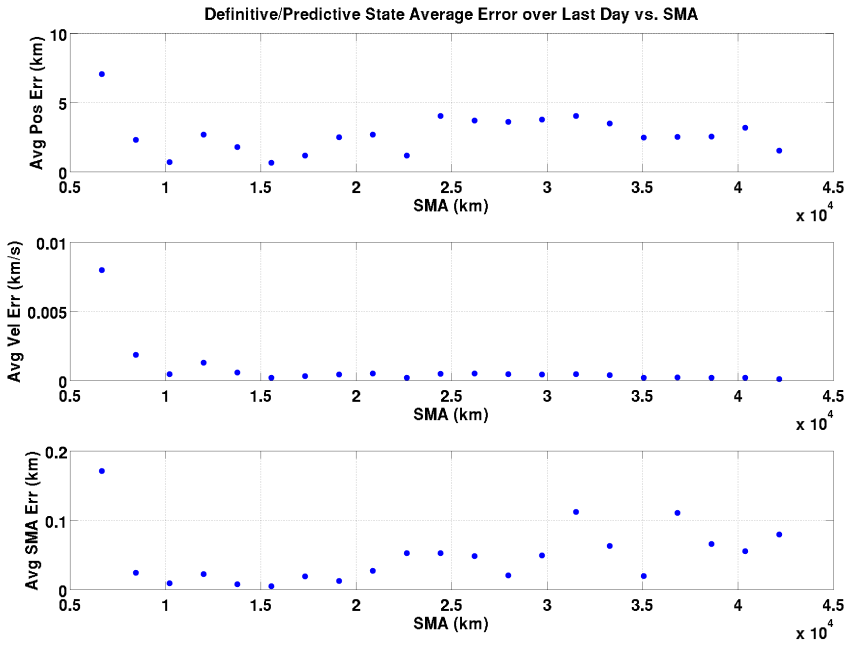

Figure 6.13: Average State Error vs. SMA. Equatorial Circular Orbit.

For definitive state error and the definitive state semi-major axis error, the lowest value in the trade space of 6678 km semi-major axis had an average position error above 5 km and an average velocity error above 0.005 km/s. The rest of the semi-major axis trade space stays below those values. The orbit design has the most influence on the lowest value of semi-major axis, and averages out for the rest of the trade space. There is also an increase in the definitive position error that peaks in the middle of the trade space (25000 km semi-major axis). Finally, there is also some variation in definitive semi-major axis error at the upper end of the trade space. This final note was ignored as the variation is +/- 0.1 km across the trade space. On the other hand, the definitive position state error is +/- 5 km across the same trade space. semi-major axis has a greater driving behavior of definitive state error, so that metric was focused on for this part of the analysis.

www.manaraa.com

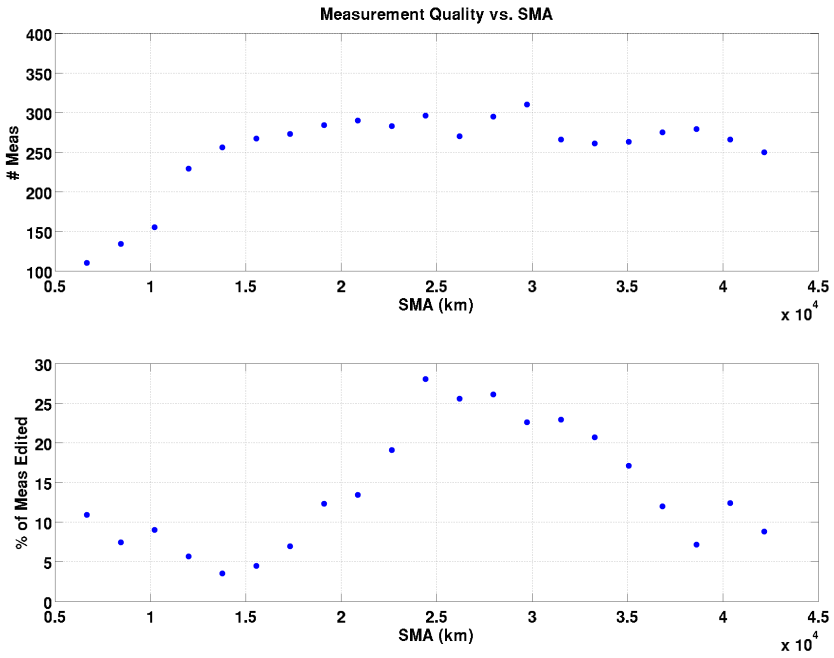

Figure 6.14: Measurement Quality vs. SMA. Equatorial Circular Orbit.

The measurement quality can be seen in Figure 6.14. A peak percentage of measurements (around 30%) are edited out around an semi-major axis of 25000 km, just like the peak in state error averages. The number of measurements increases with semi-major axis until a value of 300 measurements around 20,000 km semi-major axis. At this point, the total number of measurements remains +/- 50 measurements off that nominal value for the rest of the trade space.

It is important to note here the relationship between total measurements and the percent of measurements edited. In this trade study, the total number of measurements hover at a consistent value at 20,000 km semi-major axis. That means that, with an semi-major axis greater than 20,000 km, a higher percentage of XNAV measurements were rejected. A higher percentage of rejected measurements means fewer XNAV measurements were used with the EKF, and vice versa.

www.manaraa.com

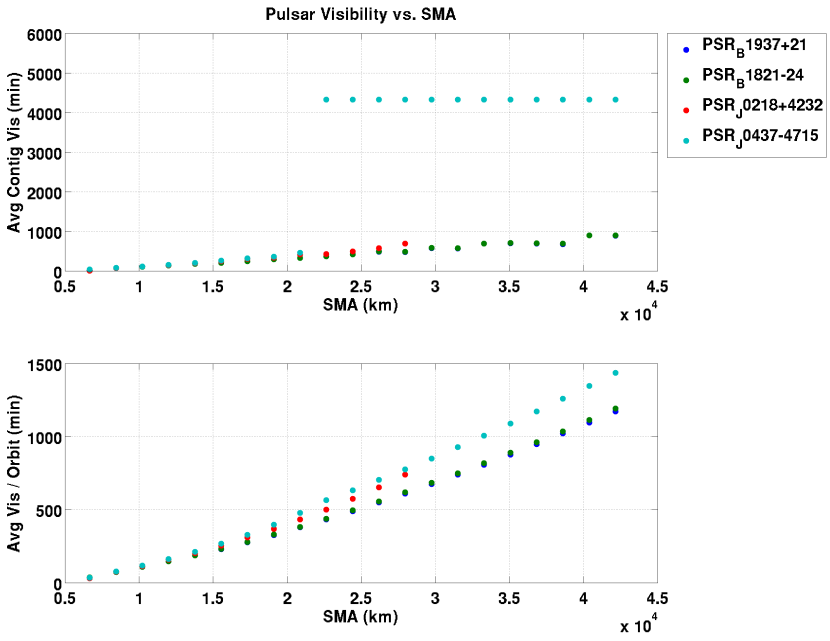

Figure 6.15: Average Visibility vs. SMA. Equatorial Circular Orbit.

Finally, increasing semi-major axis increases visibility of all pulsars. With increasing semi-major axis, each pulsar increases visibility at a different linear slope. With the geometry seen in Figure 6.12, pulsar J0437-4715 always has visibility on the spacecraft after a certain threshold of semi-major axis. The visibility for that pulsar peaks at about 4320 minutes, or the full simulation time of three days.

The increase of semi-major axis significantly increases the visibility of all pulsars. The increase in visibility allows the scheduling to maximize the number of XNAV measurements throughout the simulation. That maximum is reached around 20,000 km semi-major axis. At the same time, an increase in background radiation peaks between 20,000-25,000 km in Figure 5.10. This corresponds to the increase in edited measurements and the increase in the state error plot. As a result, it is generally favorable to increase semi-major axis beyond 40,000 km semi-major axis.

www.manaraa.com

This allows the maximum number of XNAV measurements while decreasing the total number of rejected measurements. It also equates to low definitive state error averages while avoiding areas with high background radiation.

It is also important to address the 6678 km semi-major axis case. This case has the highest definitive state error of the trade space. A high percentage of measurements were removed early in the scenario, which hurts the EKF performance throughout the scenario. This is due to the relatively small orbital period versus the CRLB pulsar observation times. The visibility of pulsars are broken up for a significant amount of time due to the proximity to Earth. The CRLB observation times are also a significant part of the orbital period, so the XNAV measurements are created with photon data from a large number of non-continuous periods. As seen in Figure 6.1, this is a bad scenario for XNAV in general. Due to the orbit dynamics of the spacecraft, the resultant XNAV measurements are insufficient to estimate the spacecraft state.

6.2.2 Variation of Orbit Eccentricity

Varying eccentricity, resultant XNAV performance is shown in Figures 6.18, 6.19. The nominal orbit parameters have an semi-major axis of 42158 km, an inclination of 0°, and an argument of periapsis at 0°. This set of orbits will be equatorial, so right ascension of the ascending node will be undefined. For implementation into the simulation software, the value of right ascension of the ascending node was set to 0°.

www.manaraa.com

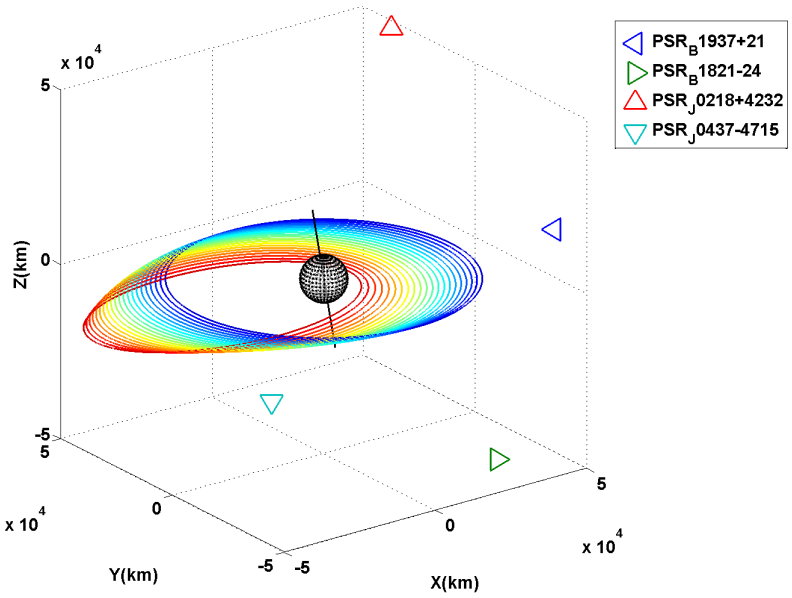

Figure 6.16: ECC Orbit Trade Space. Orbit trade value increases from blue (0) to red (0.8) for each trajectory.

The eccentricity trade space has a more complex relationship than the semi-major axis trade space. This trade space has a constant semi-major axis of 42158 km (a GEO orbit when eccentricity is 0) and all the other orbit parameters are at an initial value of 0°. Increasing eccentricity with constant orbit parameters means that the perigee of orbit begins to decrease, while the apogee of the orbit begins to increase. Within the trade space, the orbit perigee decreases from 42158 km at an eccentricity of 0 to a value of 8431.6 km (an 80% decrease) at an eccentricity of 0.8. The apogee increases from 42158 km at an eccentricity of 0 to 75884.4 km (an 180% increase) at an eccentricity of 0.8. An example of the eccentricity of 0 is seen from the earlier Figure 6.6, while an example of the eccentricity at 0.8 is seen in Figure 6.17.

www.manaraa.com

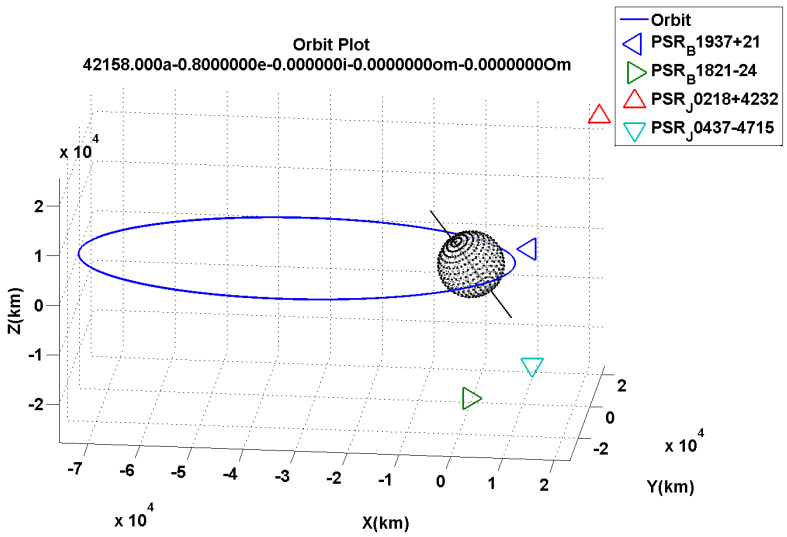

Figure 6.17: 35780 km Altitude Equatorial Orbit with an Eccentricity of 0.8: ECI MJ2000 Orbit Plot. Pulsar unit directions are represented. The line through the Earth is the Earth's magnetic axis.

A constant semi-major axis indicates a constant orbital period, as seen in Equation (2.13). The orbit period of this trade space is 1 day, or 86400 seconds. The increase of eccentricity then means that the spacecraft will spend more time at apogee within the orbital period due to Kepler's laws. Also, as seen in Figure 6.17, the spacecraft is oriented away from the inertial directions of the pulsar targets. Another influence is that, with Kepler's laws, the orbit velocity at perigee is much greater than at apogee. With an eccentricity of 0.8, the spacecraft velocity will range from 2.3 km/s at apogee and 6.9 km/s at apogee. Finally, the rate of change of argument of periapsis due to the J_2 oblateness increases when eccentricity increases. This can be seen in Figure 2.10. As the orbit is still equatorial, the rate of change of right ascension of the ascending node will not precess over time.

www.manaraa.com

These orbit behaviors are related to the visibility of these pulsars, which will be explain later in this section with Figure 6.20.

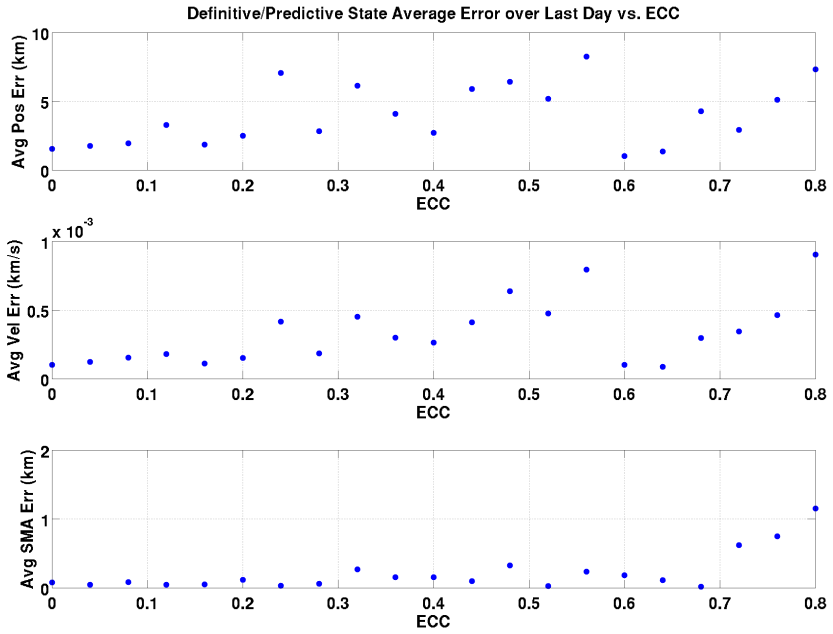

Figure 6.18: Average State Error vs. ECC. 42158 km semi-major axis Equatorial Orbit.

As seen in Figure 6.18, the average position and velocity error averages has an upper bound of 10 km and 0.8 m/s, respectively. The position and velocity averages has a lower bound of 1.9 km in position error and 0.15 m/s velocity error, respectively.

There are a couple of trends that exist within the eccentricity definitive error plots. The position error and velocity error averages increase between an eccentricity of 0.2 and 0.6. At an eccentricity of 0.6, the definitive state error for both position and velocity drops sharply. Increasing eccentricity past 0.6, the error begins to grow again in both position and velocity. Increasing eccentricity past 0.6 also shows an

www.manaraa.com

increase in the averaged semi-major axis definitive error.

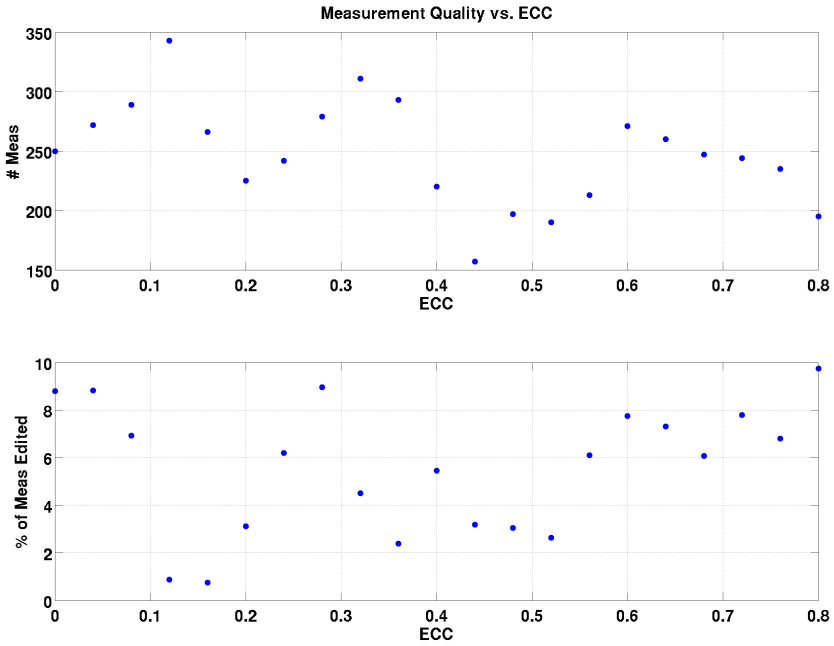

Figure 6.19: Measurement Quality vs. ECC. 42158 km SMA Equatorial Orbit.

As seen in Figure 6.19, there is a fluctuation in total number of measurements and the edited measurements. The maximum rejected number of measurements is around 10%, and the total number of measurements can peak up to 350 measurements. As seen in Figure 6.19, the increase of eccentricity is related to a downward periodic trend of total XNAV measurements. At 0.2, 0.4 and 0.6 eccentricity, the total number of measurements reaches a local minimum. At the same time, increases in edited measurements occur between 0.2-0.3 eccentricity and after 0.5 eccentricity. Together, the total number of used XNAV measurements peaks between 0.1 and 0.2 eccentricity, while the other values of eccentricity show a drop in used XNAV measurements.

www.manaraa.com

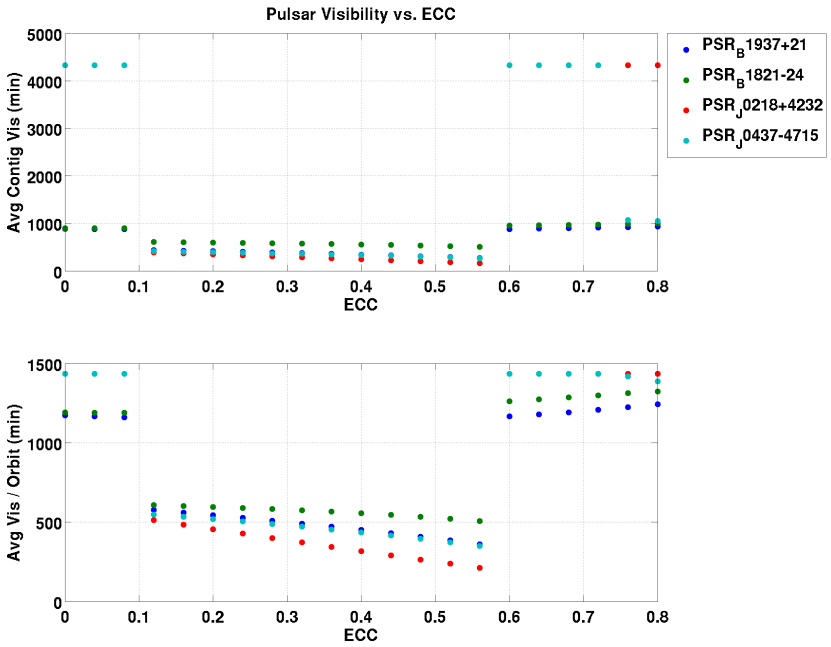

Figure 6.20: Average Visibility vs. ECC. 42158 km SMA Equatorial Orbit.

Seen in Figure 6.20, visibility has a significant drop between values of 0.1 and 0.6. The visibility averages double in value beyond 0.6 eccentricity. The orientation of the orbit seen in Figure 6.16 and 6.17 show that apogee is in an area away from the four pulsar targets. With the statements made earlier on Figure 6.16 and 6.17, the values of eccentricity between 0.1 and 0.6 indicate that Earth occultations of the pulsars decreased the overall average of pulsar visibility. Beyond an eccentricity of 0.6, the pulsars in general have much more visibility. J0437-4715 having full visibility of three days when the orbit is an eccentricity of less than 0.1 or greater than or equal to 0.6.

In summary, an eccentricity up to 0.2 has some minor benefits to XNAV performance. Those benefits drop out with increasing eccentricity. Increasing eccentricity shows an increase in visibility and total measurements while decreasing rejected

www.manaraa.com

measurements. Even though the definitive average error in position, velocity, and semi-major axis stay at a lower value up to 0.2 eccentricity, the pulsar visibility and total number of measurements drop between 0.1 and 0.2 eccentricity. Beyond 0.2 eccentricity, a growth in definitive state error is observed. The return of pulsar J0437-4715 visibility at an eccentricity of 0.6 equates to the sudden jump in total measurements and thus definitive average error. Increasing eccentricity past 0.6 decreases the total measurements and the number of rejected measurements, which brings up all the averages of definitive state error.

Kepler's laws and the J_2 Earth oblateness seen in Figure 2.10 indicate that by increasing eccentricity, the orbit will have more precession in argument of periapsis. More photon TOAs are then required to receive timing information about the orbit plane change. Also, due to the orientation of apogee, pulsar targets will be commonly visible to the spacecraft around perigee. The orbital speed will also increase at perigee as eccentricity increases. With the photon TOAs distributed across areas of visible pulsar targets, there is a high chance that few photon TOAs were collected for phase estimation around perigee. The timing information in the photon TOAs are required to correct the phase estimate of the spacecraft state relative to Earth. The sparsity of photon TOAs around perigee deteriorates the photon information over that part of the orbit. The deteriorated photon information relates to an increase in XNAV phase residuals. As a result, for values of eccentricity greater than 0.6, there is a definite increase in definitive state estimation error and rejected XNAV measurements.

www.manaraa.com

6.2.3 Variation of Orbit Inclination

XNAV performance over varying inclination is shown in Figures 6.22, 6.23, and 6.24. The nominal orbit parameters have an semi-major axis of 42158 km, an eccentricity of 0, and a right ascension of the ascending node at 0°. argument of periapsis is undefined for a circular orbit, but for implementation into the simulation, the value was set to 0°.

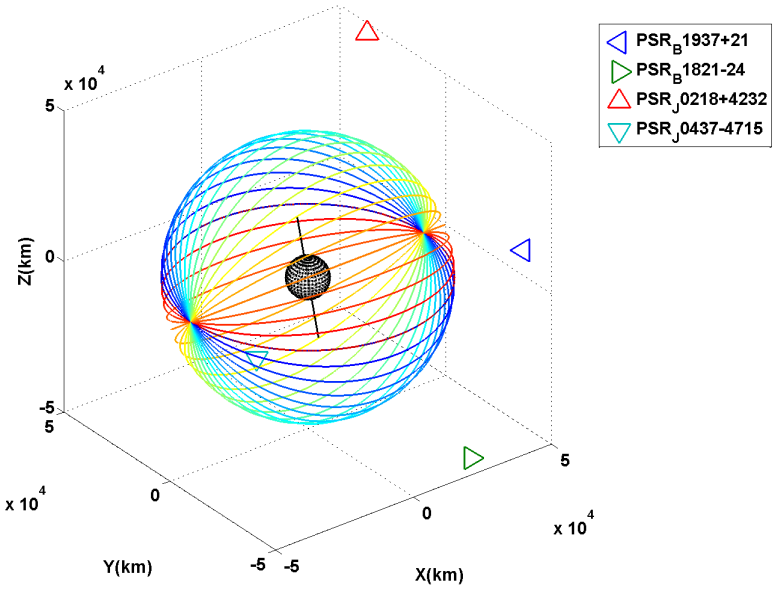

Figure 6.21: INC Orbit Trade Space. Orbit trade value increases from blue (0°) to red (180°) for each trajectory.

The inclination trade space is seen in Figure 6.21. A change in inclination, described in chapter 2, rotates the orbit plane around the line of nodes vector. This line of nodes vector happens to be closely aligned with the horizontal axis of the MJ2000 frame. With a constant semi-major axis and eccentricity, the orbital period and speed will stay constant at 86400 seconds and 4.3 km/s respectively. The

www.manaraa.com

orientation of the magnetic axis of Earth now varies with the change in inclination, seen as the black line cutting through the Earth in Figure 6.21. inclination can directly align the orbit so that the magnetic axis lies almost perpendicular to the orbit plane. The variable background radiation environment around the magnetic poles was modeled as an occultation in this thesis. The result of this occultation is seen in this trade analysis.

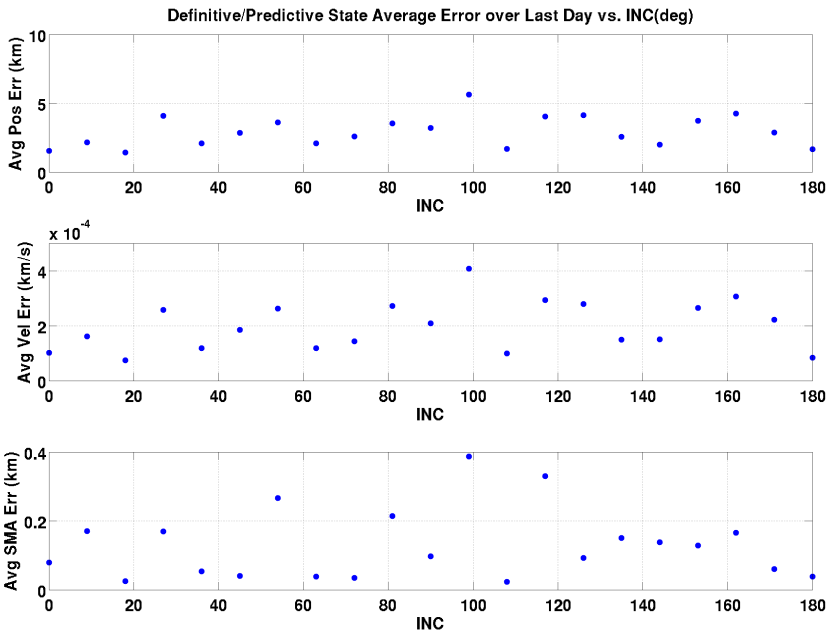

Figure 6.22: Average State Error vs. INC. 42158 km SMA Circular Orbit.

The variation of inclination shows an averaged state error below 6 km RSS in position, 4.2e-4 km/s in velocity, and 0.4 km for SMA estimation for the entire trade space. There is a maximum average state error in all plots of Figure 6.22 near 90° INC.

www.manaraa.com

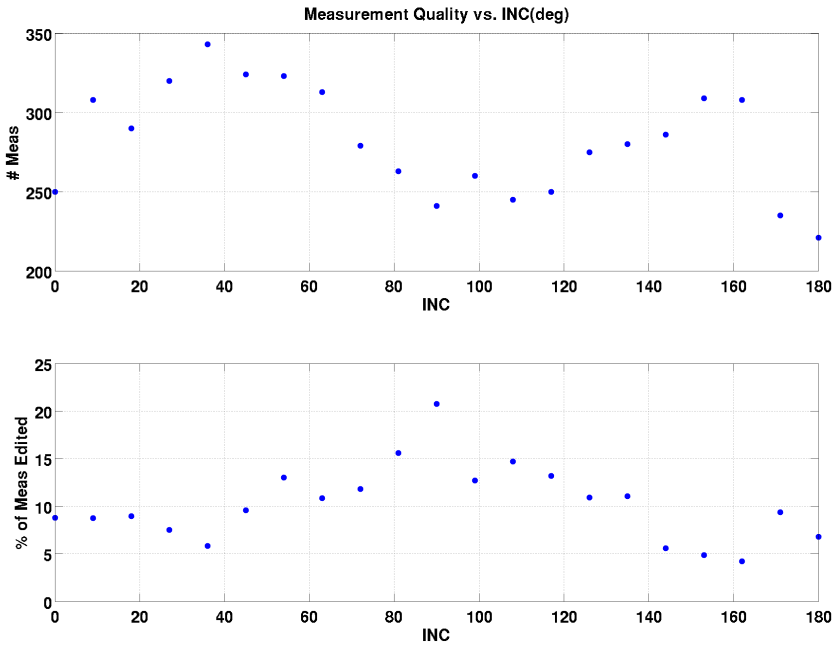

Figure 6.23: Measurement Quality vs. INC. 42158 km SMA Circular Orbit.

There is a drop in total measurements and an percentage increase in edited measurements around 90° INC, as seen in Figure 6.23.

www.manaraa.com

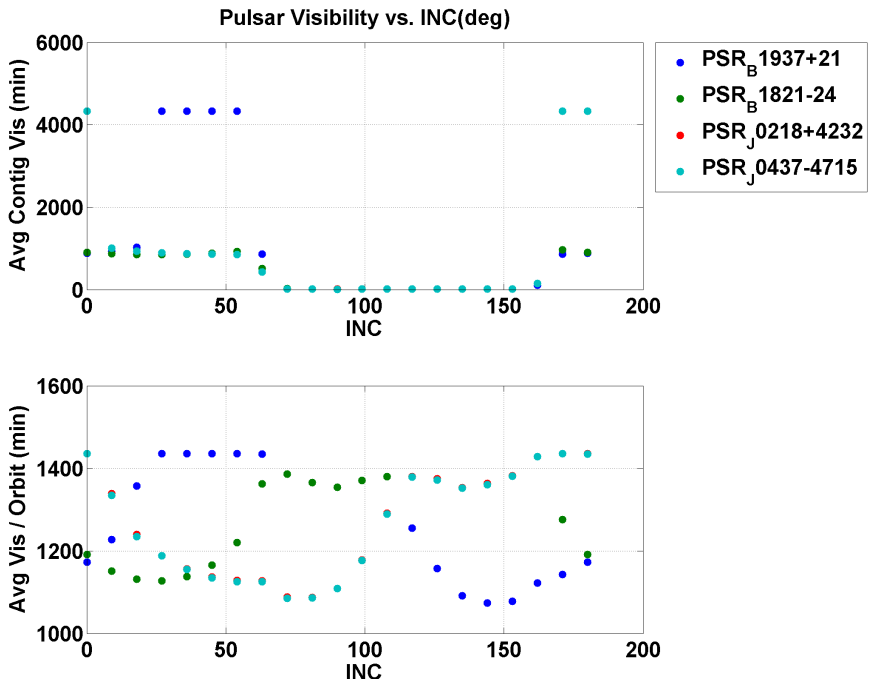

Figure 6.24: Average Visibility vs. INC. 42158 km SMA Circular Orbit.

The visibility averaged periods between an inclination of 60°and 160° suddenly drops for continuous periods but not for orbital periods. Also, pulsar J0427-4715 is visible for the entire three day scenario between an inclination of 25° and 50°.

For this thesis, areas near the magnetic north pole and south pole were treated similarly to occultations due to the significant variation of background radiation. As a result, orbits with an inclination around 90° spend more time passing over these poles, during which all pulsars are occulted. This causes the sudden drop in visibility and thus a lower drop in total measurements. With the breakup of observations due to the magnetic pole occultations, the percentage of edited measurements increased as well. As a result, the averaged definitive state error increased to 6 km in position, 4.1e-4 km/s in velocity, and 0.391 km in definitive semi-major axis error.

www.manaraa.com

6.2.4 Variation of the Orbit Argument Of Periapsis

XNAV performance versus argument of periapsis is shown in Figures 6.30, 6.31, and 6.32. The nominal orbit parameters have an semi-major axis of 42158 km, a eccentricity of 0.3, an inclination of 28.5°, and a right ascension of the ascending node at 0°. The argument of periapsis and right ascension of the ascending node are rotation angles that are ambiguous in value for a circular (eccentricity = 0) and an equatorial (inclination = 0°) orbit. As a result, both the study of argument of periapsis and right ascension of the ascending node are with inclined and eccentric orbits. They are also, unlike the earlier orbit parameters, driven by the J_2 orbit perturbation. This trade study shows their initial values, but they linearly change over the 3 day experiment period.

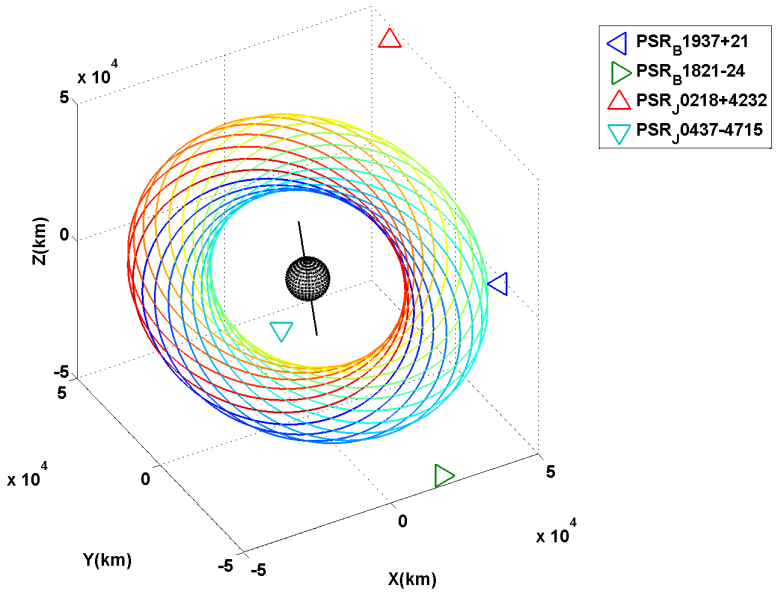

Figure 6.25: AOP Orbit Trade Space. Orbit trade value increases from blue (0°) to red (360°) for each trajectory.

www.manaraa.com

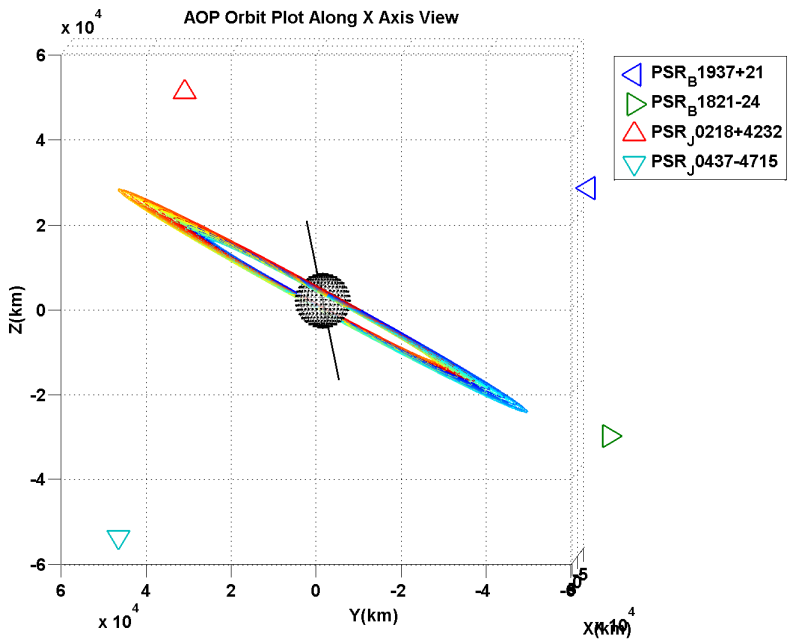

Figure 6.26: AOP Orbit Trade Space, Along X Axis View.

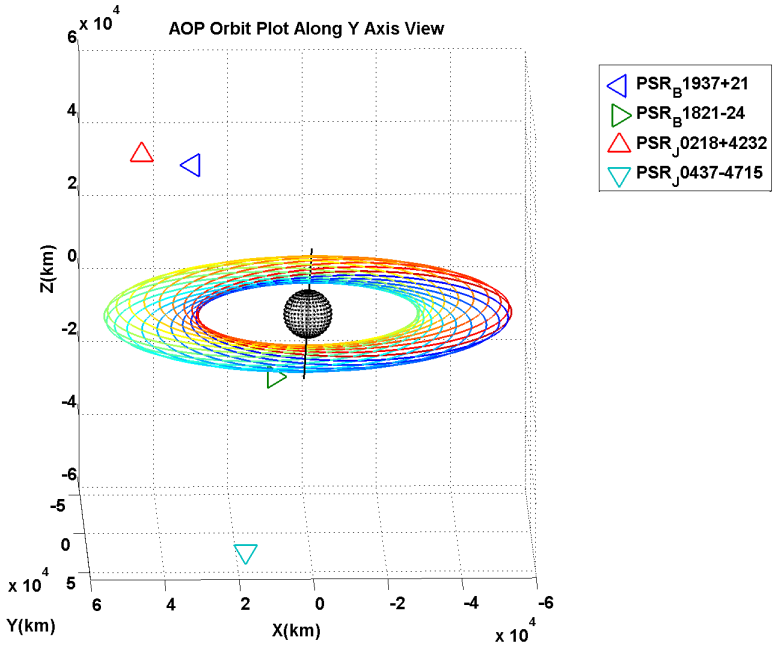

Figure 6.27: AOP Orbit Trade Space, Along Y Axis View.

www.manaraa.com

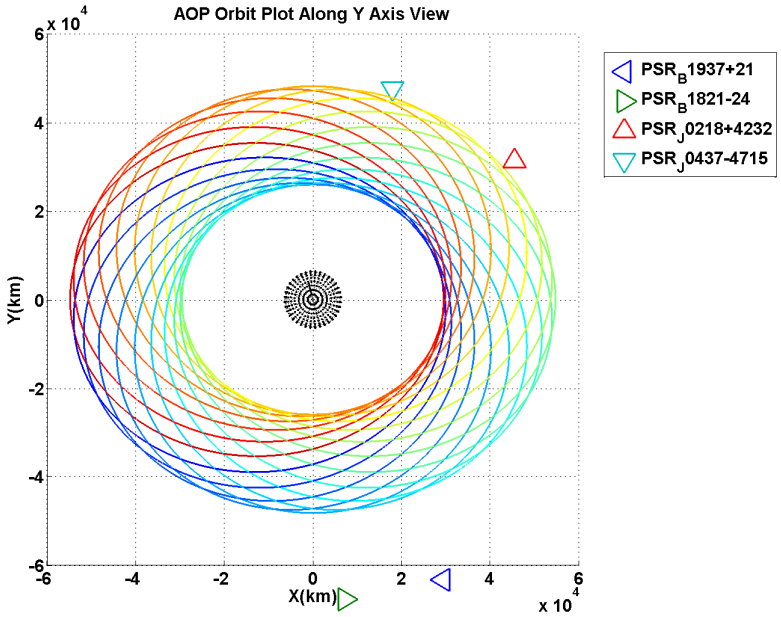

Figure 6.28: AOP Orbit Trade Space, Along Z Axis View. AOP range from 0° (blue orbit) to 360° (red orbit).

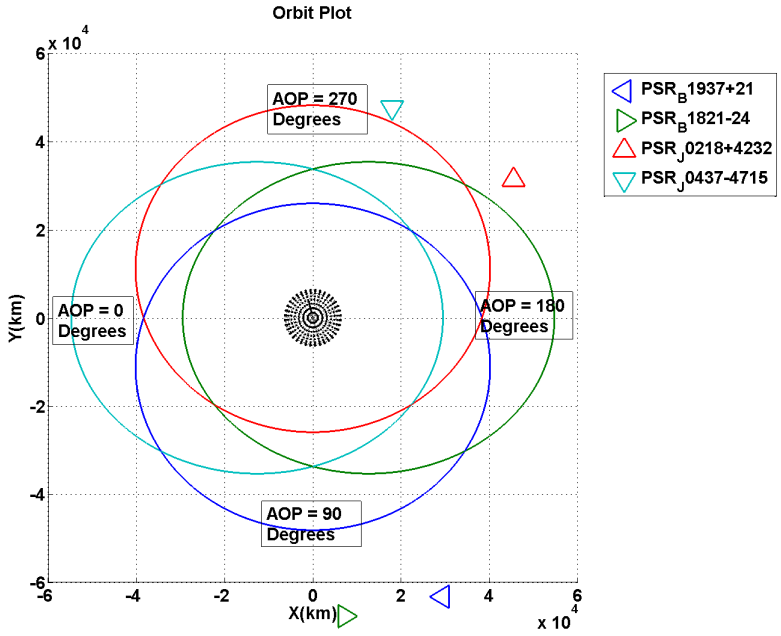

Figure 6.29: AOP Orbit Trade Space, Along Z Axis View.

Changing an orbit argument of periapsis rotates the orbit around its angular

www.manaraa.com

momentum vector. As this orbit has a nonzero value of eccentricity, the change of argument of periapsis also rotates the orbit apogee location around. Seen in Figure 6.29, the apogee of the orbit rotates counterclockwise from the negative X axis to the positive X axis and back. Similar to the patterns seen in the eccentricity trade analysis, the orientation of apogee will change the visibility of each pulsar as the spacecraft will spend more time at apogee than at perigee.

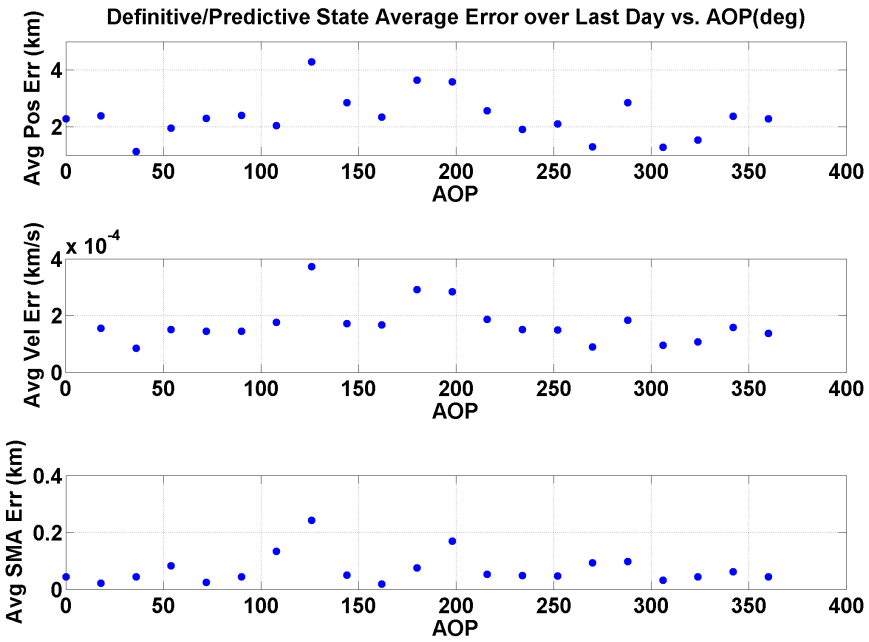

Figure 6.30: Average State Error vs. AOP. 42158 km SMA Eccentric Inclined Orbit.

The argument of periapsis trade in Figure 6.30 shows a maximum averaged position error of 4.5 km and a maximum averaged velocity error of 4e-4 km/s. The definitive semi-major axis error is bounded to 0.3 km error. The semi-major axis error indicates periodic increases about every 65° with various amplitudes.

www.manaraa.com

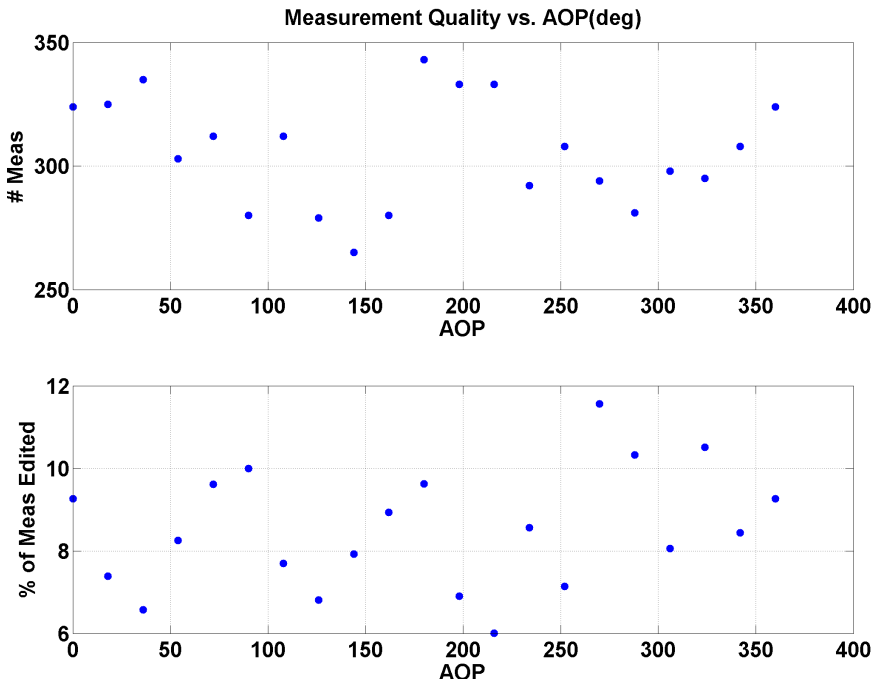

Figure 6.31: Measurement Quality vs. AOP. 42158 km SMA Eccentric Inclined Orbit.

There is a general decrease in XNAV measurements from 0° to 150°. A maximum of XNAV measurements appears between 150° and 200°. There is also a repeated pattern in rejected measurements between 0° to 150°. Higher values of argument of periapsis beyond 150° are varied in quality.

www.manaraa.com

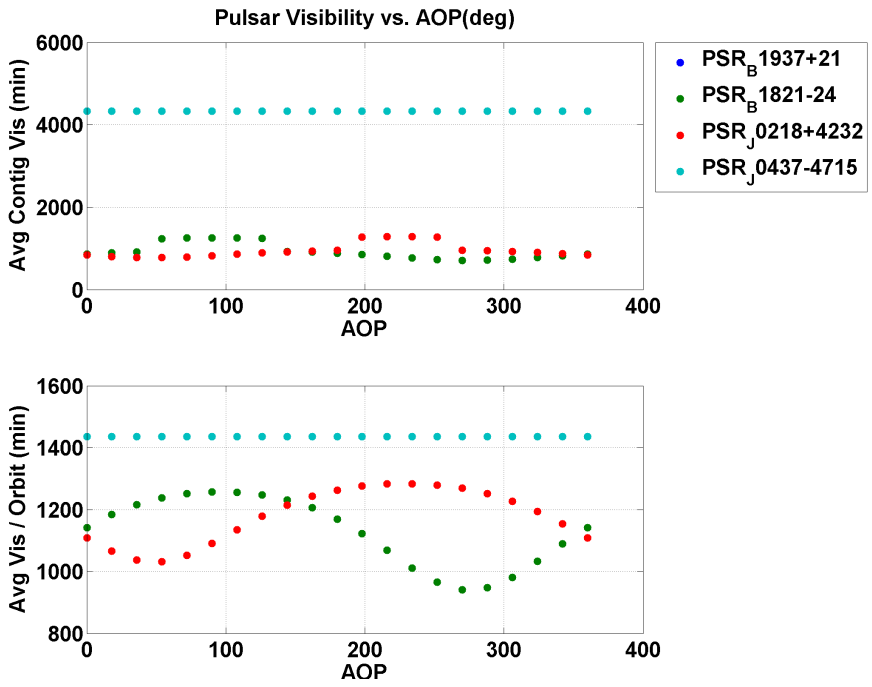

Figure 6.32: Average Visibility vs. AOP. 42158 km SMA Eccentric Inclined Orbit.

Pulsar visibility shows the most pronounced pattern based on argument of periapsis. Pulsar B1937+21 and J0437-4715 are visible for the entire trade space, and the other two pulsars sinusoidally vary in visibility throughout the scenario. This visibility pattern can be seen in Figure 6.25, as the change in argument of periapsis simply rotates where the orbit apogee is without changing the orbit plane's inertial position is to the pulsars. As the spacecraft must take more time orbiting past apogee, the sinusoidal peaks of visibility are related to the visibility of the pulsars for that orbit's apogee. It is also important to note that at around 150°argument of periapsis, the averaged visibility per orbit is maximized across all four pulsars. For values of argument of periapsis over 150°, pulsar B1821-24 visibility drops at most over 200 minutes per orbit period.

www.manaraa.com

The orbit geometry reveals more about XNAV performance and argument of periapsis. From the general diagram of XNAV in Figure 1.2 and the phase estimation equation (5.14), navigation measurements are used to estimate spacecraft dynamics based on the light time delay in the unit direction of the pulsar. A batch of photon TOAs are required to correct a phase estimate as the timing information is used to summarize the spacecraft dynamics. This means that timing information aligned with the pulsar unit direction will reveal more variation in the photon TOAs and better reflect the spacecraft change of state. At the same time, the greatest build-up of definitive state error is in the in-track direction of the RIC frame [9]. As this component is consistently in the orbit plane, finding an orbit plane that is aligned with the pulsar unit vector allows the photon pulsar information from that target to address the worst local direction of definitive state error.

As seen in Figures 6.26, 6.27, and 6.28, three of the four pulsars have a significant component that is perpendicular to the orbit plane. When comparing the angle between the pulsar unit vectors and the orbit angular momentum vector averaged over the trade space of argument of periapsis, the values are: 46.5° for B1937+21, 3.49° for B1821-24, 23.3° for J0218+4232, and 71.5° for J0437-4715. B1821-24 is the closest to the orbit plane, but there is only a weak correlation between the availability of B1821-24 versus navigation performance.

Overall, information on the XNAV performance based on argument of periapsis is limited based on the current data. For a given value of semi-major axis, eccentricity and inclination in the trade space, the total rate of change of right ascension of the ascending node and argument of periapsis varies significantly over

www.manaraa.com

time. As seen in Figure 2.9, 2.10, and 2.11, the rate of change of both argument of periapsis will increase when semi-major axis/INC is minimized and eccentricity is maximized. A secular precession of the orbit plane requires appropriate information to perform orbit determination. If there is less out-of-plane orbit motion, the XNAV measurements will not need to estimate that motion. This alleviates the burden of the EKF estimation.

Unlike the earlier orbit parameters, the averaged definitive position, velocity and semi-major axis error do not have as wide a variation in magnitude as the other elements. Little can be concluded from the averaged steady state definitive error. Also, the trend of XNAV measurements do not match the trend of averaged visibility as well as the trend in state error. In previous analyses, the increase in overall pulsar visibility indicated an increase in XNAV measurements, which usually led to a decrease in state error. Argument of periapsis is an exception to this trend. A cyclic behavior of pulsar visibility is observed in Figure 6.32, but the other plots do not follow this trend.

Further study of the argument of periapsis trade space would need to study the relationship of timing accuracy, the scheduling algorithm, and the relative orbit geometry of the pulsar targets. As the measurements are scheduled sequentially, the analysis of argument of periapsis with encompassing all possible groups of XNAV measurements is non-trivial. The XNAV performance of argument of periapsis is most likely within this relationship, as it will drive the long term steady state error shown in Figure 6.30.

www.manaraa.com

6.2.5 Variation of the Orbit Right Ascension of the Ascending Node

XNAV performance versus right ascension of the ascending node is shown in Figures 6.35, 6.36, and 6.37. The nominal orbit parameters have an semi-major axis of 42158 km, a eccentricity of 0.3, an inclination of 28.5°, and an argument of periapsis at 0°.

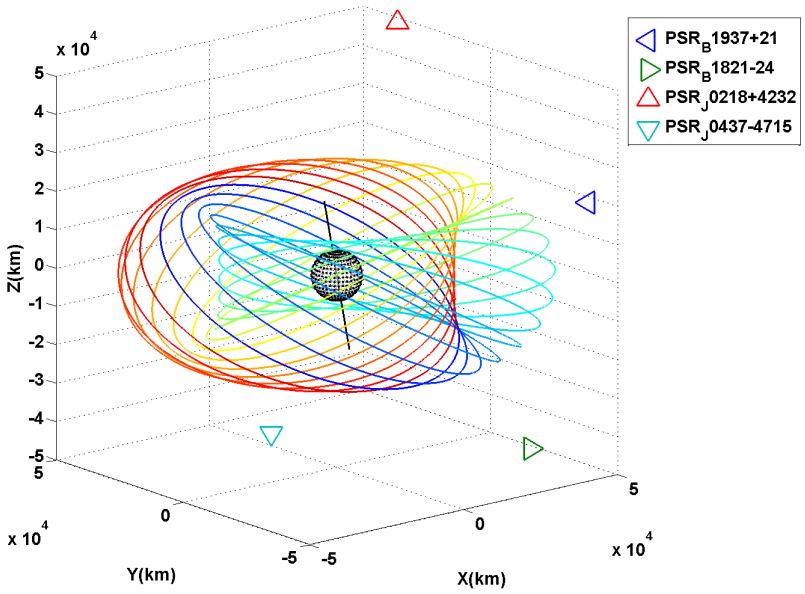

Figure 6.33: RAAN Orbit Trade Space. Orbit trade value increases on from blue (0°) to red (360°) trajectories.

www.manaraa.com

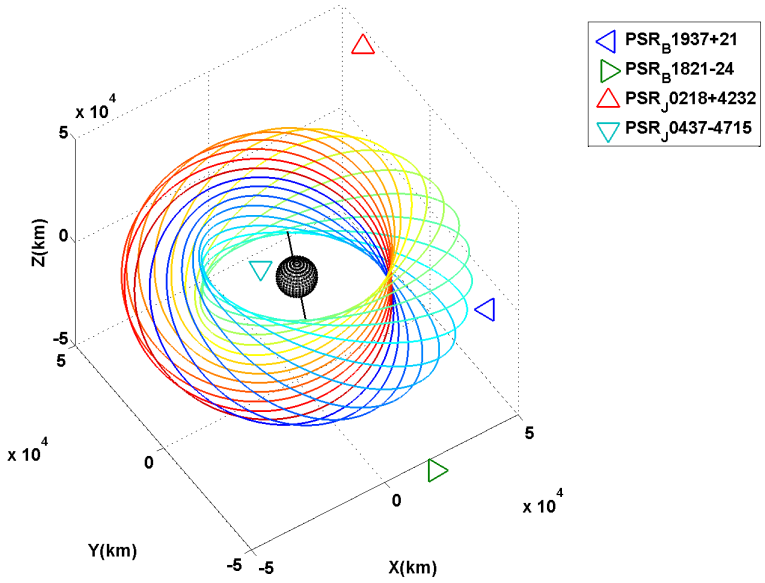

Figure 6.34: RAAN Orbit Trade Space from the perspective of Pulsar J0437-4715. Orbit value increases from blue (0°) to red (360°) trajectories.

The variation of right ascension of the ascending node is an orbit rotation that rotates about the ECI Z Axis. With the nonzero inclination and the nonzero eccentricity, the trade space of right ascension of the ascending node orbits slowly form the shape of a torii versus the spherical shape that the inclination trade space creates. This can be seen in Figure 6.33.

www.manaraa.com

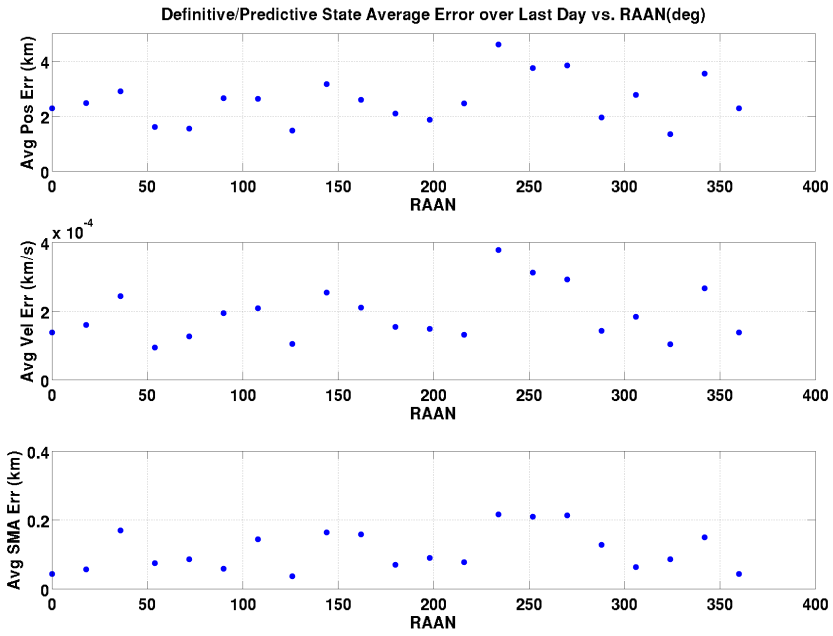

Figure 6.35: Average State Error vs. RAAN. 42158 km SMA Eccentric Inclined Orbit.

RAAN does not show as strong of periodic behavior of argument of periapsis, but the state error averages for right ascension of the ascending node are capped by the same limits as the results across argument of periapsis. There is a peak of definitive state error between 200° and 250° RAAN.

www.manaraa.com

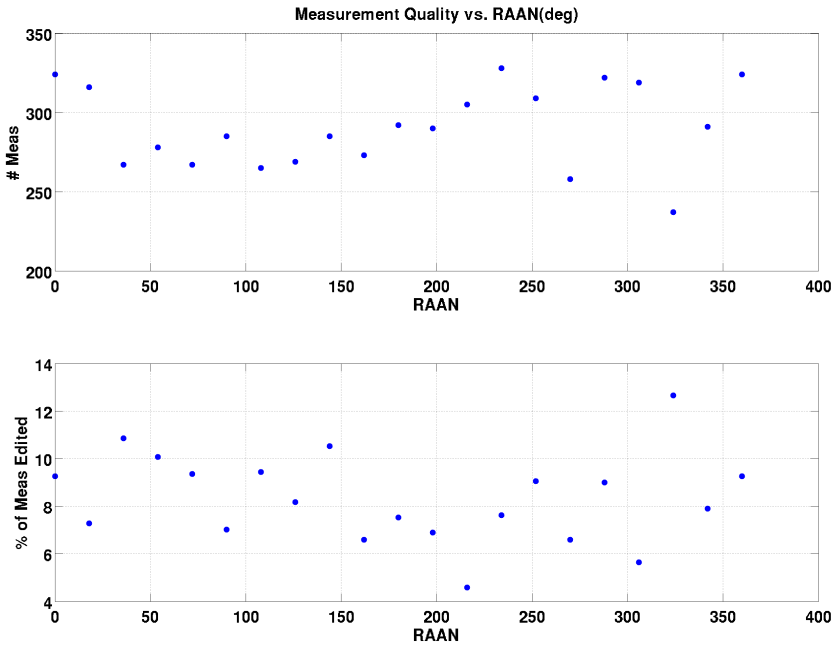

Figure 6.36: Measurement Quality vs. RAAN. 42158 km SMA Eccentric Inclined Orbit.

Seen in Figure 6.36, the total number of XNAV measurements stay around 270 measurements between 50°and 200° RAAN. For a value of right ascension of the ascending node greater than 200°, the total number of XNAV measurements vary by +/- 100 measurements.

www.manaraa.com

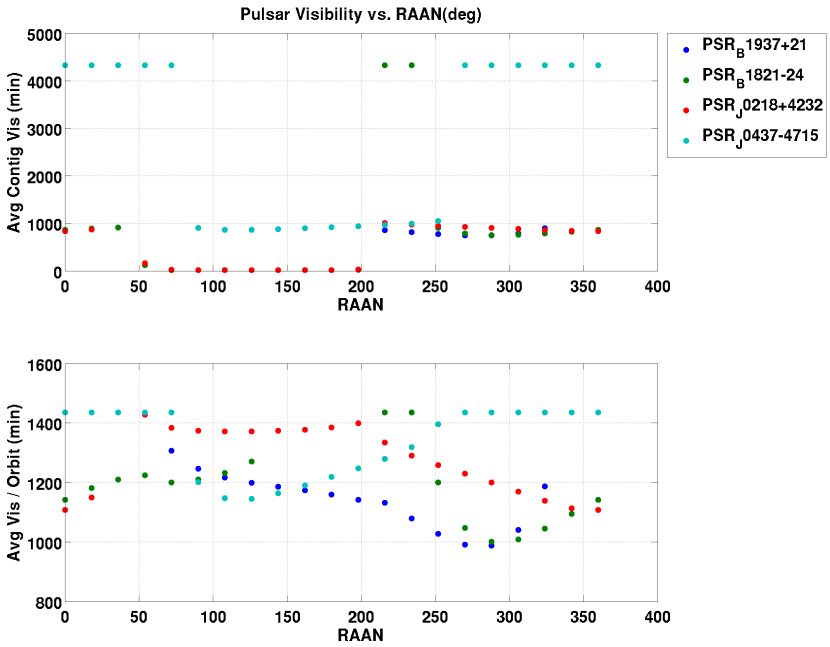

Figure 6.37: Average Visibility vs. RAAN. 42158 km SMA Eccentric Inclined Orbit.

As seen in Figure 6.37, pulsar J0437-4715 has almost constant visibility except from 50°to 200°. B1821-24 is fully visible for the entire scenario for a right ascension of the ascending node between 200° and 250°. Each pulsar has a unique trend of pulsar visibility averaged over and orbit period. As per the definition of the three orbit rotation angles right ascension of the ascending node, argument of periapsis, and inclination, the pattern is periodic over the entire trade space. For right ascension of the ascending node, the pattern is less sinusoidal than the other orbit parameters. The sudden drop in visibility is due to the orbit geometry and the change of right ascension of the ascending node. Right ascension of the ascending node changes the orbit orientation to the pulsars inertially which results in a toroidal pattern seen in Figure 6.33 and more so in Figure 6.34. With the orbit slightly eccentric and slightly inclined, a small breakup in visibility can occur with a particular set of orbits which

www.manaraa.com

drops the overall average of continuous visibility.

Overall, the conclusions for XNAV performance versus right ascension of the ascending node is similar to the study of argument of periapsis. Future work is needed to define the relationship between the pulsar timing accuracy, geometry of XNAV measurements and the scheduling algorithm. Also, the values of semi-major axis, eccentricity, and inclination cause both right ascension of the ascending node and argument of periapsis to change linearly over time due to the J_2 perturbation. This adds another layer of complexity to this orbit parameter and the XNAV measurement. Finally, XNAV definitive state error with varying right ascension of the ascending node is on the same order of magnitude as argument of periapsis, so right ascension of the ascending node seems to have a small influence on averaged state errors as does argument of periapsis.

However, there is a sensitivity of right ascension of the ascending node and argument of periapsis which is explained in the next section, based on the thesis formulation of creating XNAV measurements.

6.2.6 Sensitivity of Initial Conditions

It has been observed that initial measurements of XNAV dictate a large part of XNAV performance with this thesis. The filter in this thesis is designed to rely on measurements and it begins with an initial error on the estimate state. Thus, the initial measurements are critical to reducing state error before it can continue to propagate. It is the value of all the orbit elements that drives the first XNAV

www.manaraa.com

measurement which subsequently dictates navigation performance. As one pulsar is observed at one time in this thesis, the cadence of subsequent measurements then changes for the rest of the scenario.

One way to observe this behavior is to track an orbit with a small trade space value of semi-major axis, as the total amount of pulsar visibility per orbit shortens. With an eccentricity of 0 and an inclination of 0°, the right ascension and the argument of periapsis will drive which pulsars will be available for observation. This is a discrete way to change the cadence of measurements and thus navigation performance.

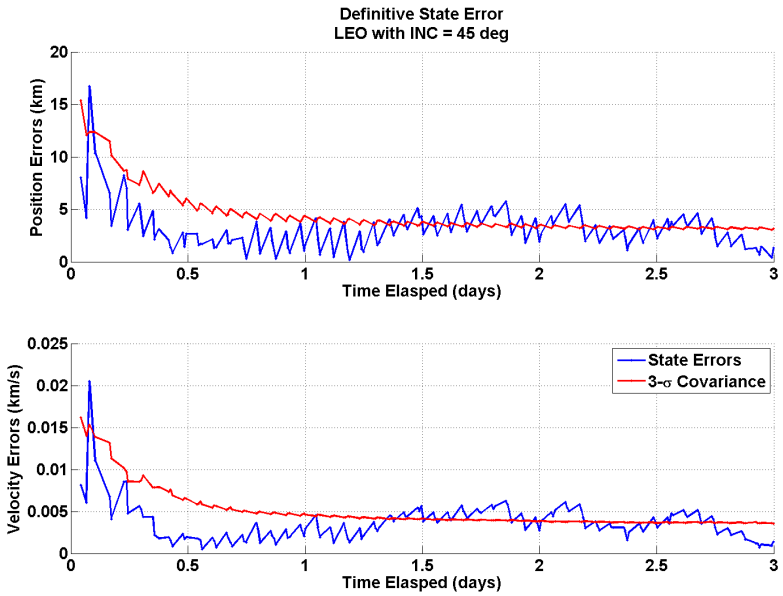

Figure 6.38: Definitive Error performance for a LEO with an INC of 45°with AOP and RAAN equal to 0°.

www.manaraa.com

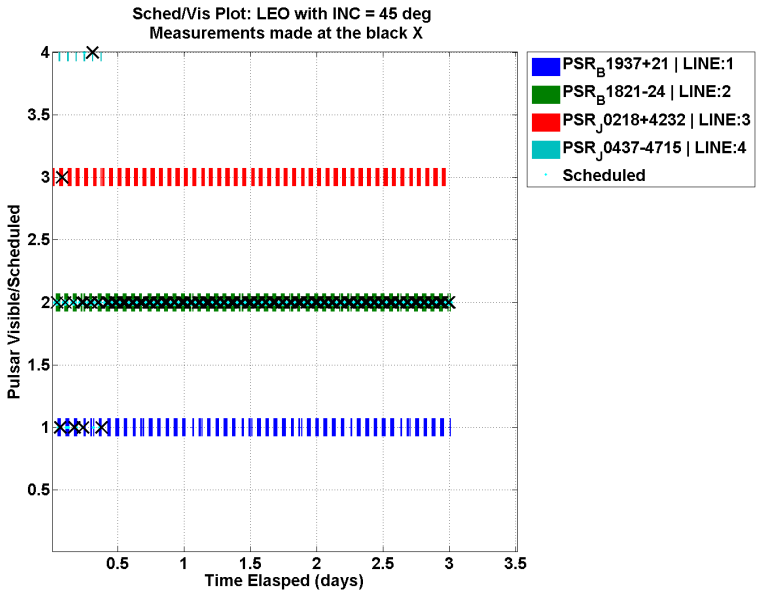

Figure 6.39: Pulsar Visibility/Schedule for a LEO with an INC of 45°with AOP and RAAN equal to 0°.

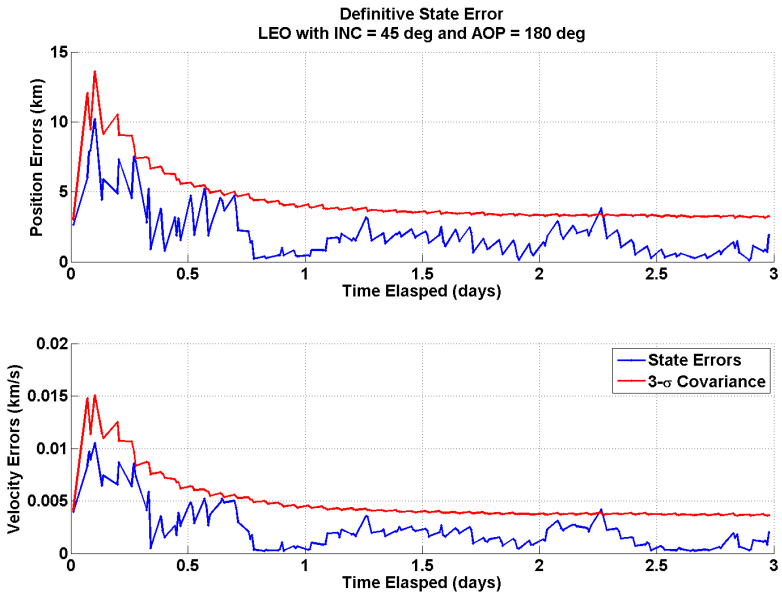

Figure 6.40: Definitive Error performance for a LEO with an INC of 45°, an AOP of 180°and a RAAN of 0°

www.manaraa.com

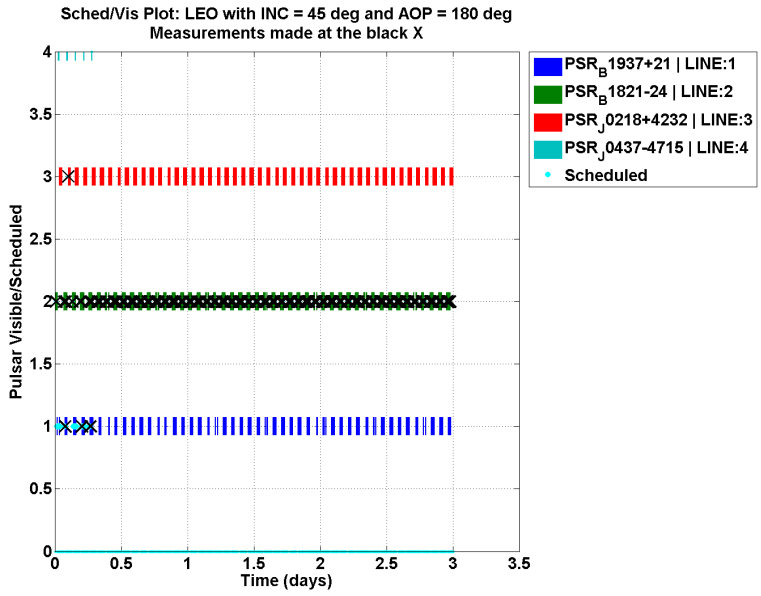

Figure 6.41: Pulsar Visibility/Schedule for a LEO with an INC of 45°, an AOP of 180°and a RAAN of 0°

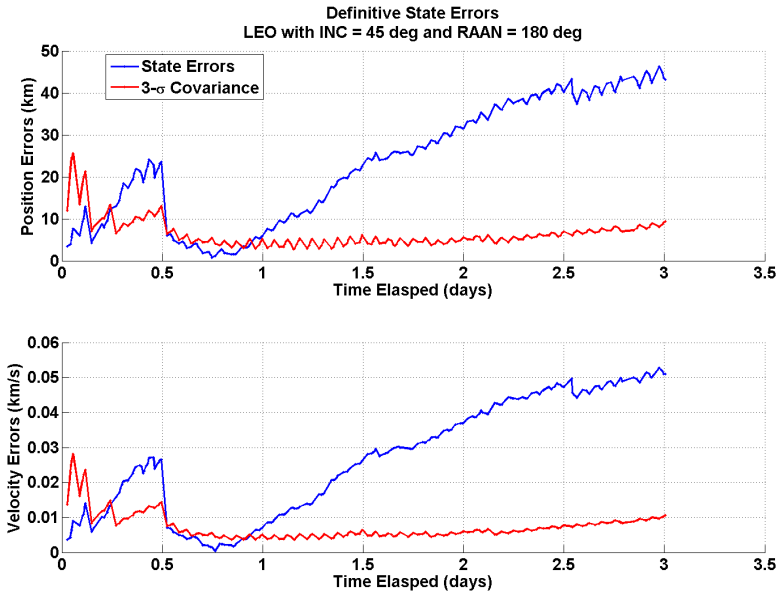

Figure 6.42: Definitive Error performance for a LEO with an INC of 45°, an AOP of 0°and a RAAN of 180°

www.manaraa.com

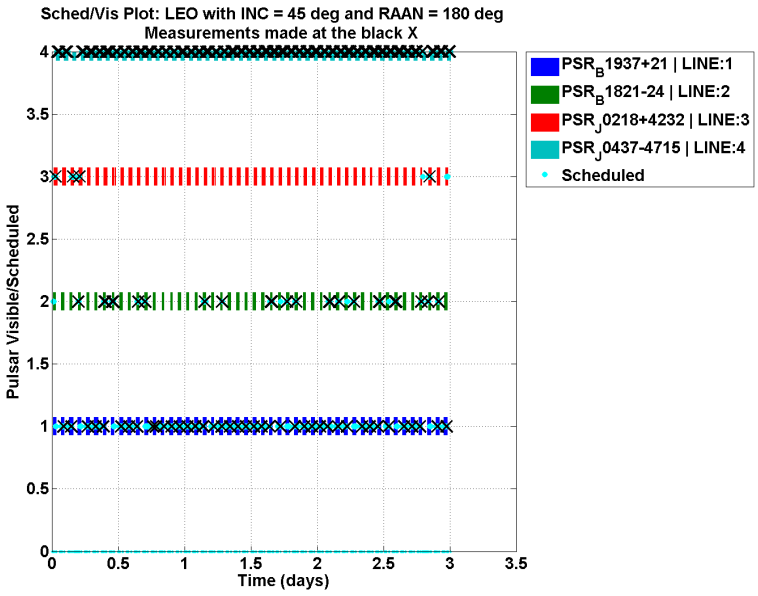

Figure 6.43: Pulsar Visibility/Schedule for a LEO with an INC of 45°, an AOP of 0°, and a RAAN of 180°

Figures 6.38, 6.40, and 6.42 show that performance can change from convergence to divergence with the change of argument of periapsis and right ascension of the ascending node. With Figure 6.39, 6.41 and 6.43, the schedules are significantly different. The initial measurement of B1821-24 results in navigation convergence, while the initial measurement of another pulsar caused by a different right ascension of the ascending node results in navigation state divergence.

This particular formulation of XNAV makes a significant number of linearity assumptions. In the process, it has a sensitivity to the total number of pulsar measurements over a given time period. As the state will deteriorate without any XNAV measurements, subsequent state estimate updates from XNAV measurements must be frequent enough to assert that the orbit dynamics can still be linearized. This re-

www.manaraa.com

quirement is seen in multiple places of the XNAV formulation. First, Equation 5.12 shows that the optimization of phase and frequency offsets q and f are for short observation periods and a linear model is adopted to model these offsets. This linearization is, to first order, related to the offset of state accuracy in the direction of the pulsar. If a linear estimate cannot be found to perform phase estimation, the XNAV measurement is less accurate for state estimation. Second, the measurement model for XNAV requires an estimate state, seen in Equation (5.14). If a series of inaccurate estimate states (from inaccurate measurements) are used in the measurement model, the solution will naturally diverge. Finally, the EKF is formulated by linearizing around the estimate state as seen in Equation (2.35). Within the EKF formulation, the Kalman filter optimal control input is predicated on linear state dynamics. If estimate states in the EKF cannot be related to each other by the linear transformation of the state transition matrix, the filter itself will also fail to estimate the spacecraft state.

There is a significant amount of coupled behavior of an orbit design and XNAV performance due to the sensitivity of initial XNAV measurements. The next section will do a first order study of that coupled behavior within the orbit design trade space.

6.3 Coupled Kepler Element Variation

The previous section explored how each individual orbital element influences XNAV performance. However, these results assumed constant values from the other

www.manaraa.com

orbital parameters. This section observes the sensitivity of XNAV performance when one Kepler element is now constant and the other four orbital elements are varied across the trade space. The constant Kepler element is held at three values: the lower bound, the median, and then the upper bound of its own trade space. In this way, a sensitivity analysis across the other four orbit parameters can be explored to first order.

This study is a broad exploration of sensitivity between orbital parameters and XNAV performance. The analysis results do not isolate each orbit parameter's relationship to the other. Further studies that prove correlations between individual Kepler elements and other combinations are a potential direction of study beyond this thesis.

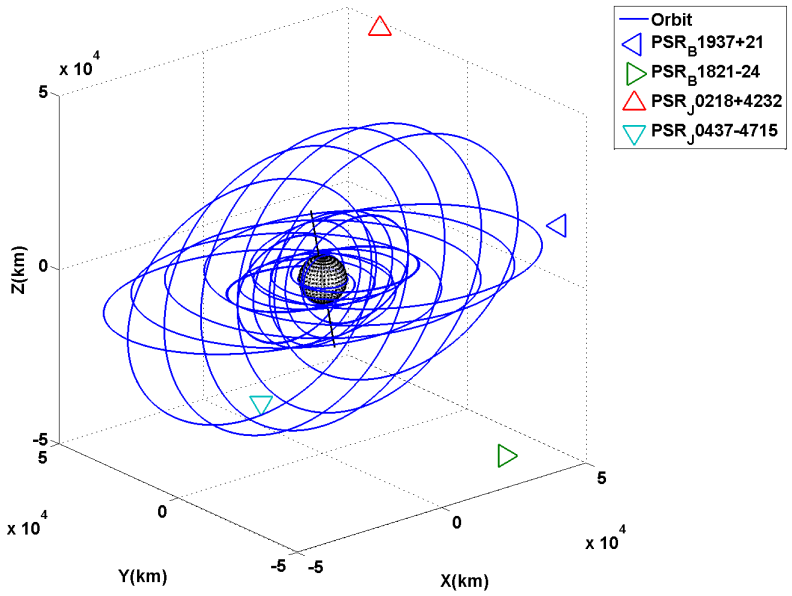

Figure 6.44: Coupled Kepler Element Orbit Trade Space. An equal distribution of variation across all the orbital elements are represented.

www.manaraa.com

Table 6.3: List of Coupled Elements Orbit Trade Study

Kepler Element	Low Value	Median Value	High Value
SMA	6678 km	18504.7 km	42158 km
ECC	0.0	0.3	0.6
INC	0 degrees	90 degrees	180 degrees
AOP	0 degrees	180 degrees	360 degrees
RAAN	0 degrees	180 degrees	360 degrees

Seen in Figure 6.44, the orbits represented are the orbits used in this section of the analysis. It is the distribution of all combinations of orbit parameters across the trade space. Those orbits consist of the lower, median and upper limits of the trade space as seen in Table 6.3.

Note that the value of argument of periapsis and right ascension of the ascending node could be undefined depending on the value of eccentricity and inclination. The software simulation itself will still input a value for argument of periapsis or right ascension of the ascending node, it will just not drive the orbit dynamics in the simulation itself. All results are presented below, whether argument of periapsis or right ascension of the ascending node are defined or undefined angles.

XNAV performance in this section are represented with logarithmic axes. The x axis is the averaged definitive position error and the y axis is the averaged velocity error. This format was chosen to display the spread of definitive state error with the variation of orbit parameters.

With those axes, the same data set is repeated in the following five Fig-

www.manaraa.com

ures: 6.45, 6.46, 6.47, 6.48,and 6.49. The averaged position/velocity error logarithmic plot is reformatted to display the sensitivity of a single parameter to all other parameters. This is done with the coloring scheme of each plot; blue points represent the bottom of the trade space, green indicates the median of the trade space and red points represent the upper part of the trade space.

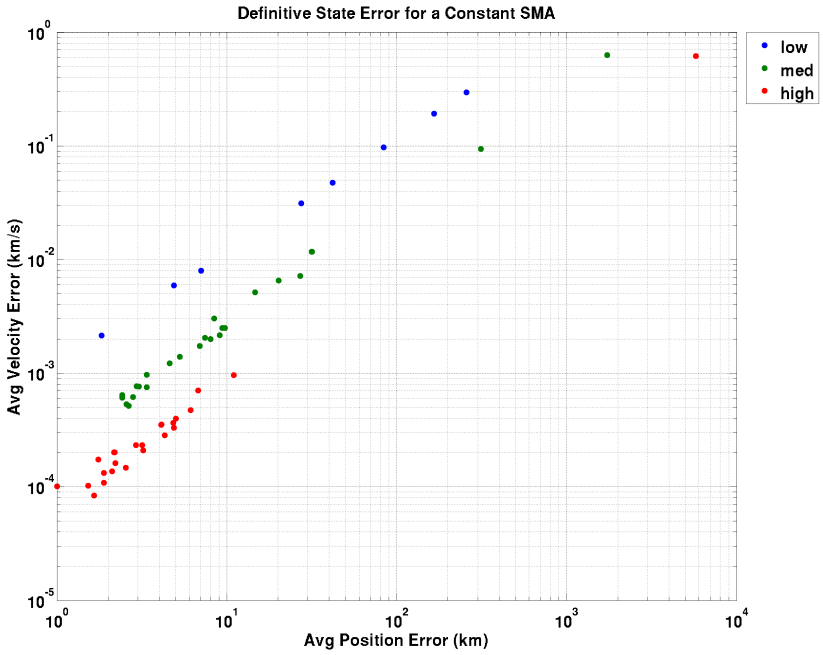

Figure 6.45: Varying other Kepler elements with three values of SMA (low, med, high) to Observe Average Position and Velocity Error over the Last Simulation Day.

As seen in Figure 6.45, the full data set consists of averaged position/velocity error from the subset of the trade space, seen in Figure 6.44. The data linearly increases between position/velocity error. The bounds in this data set range between 0.0001 km/s to 1 km/s velocity error and 1-10000 km position error. There are about 200 points total in all plots. The solution is considered diverged in this thesis if the position error is greater than 10 km in position error, similar to the requirements

www.manaraa.com

for the SEXTANT mission.

The separation of semi-major axis seen in Figure 6.45 creates discrete groups of XNAV performance. There are fewer points of data for the low semi-major axis of 6678 km. This is because the orbit perigee is unreal when semi-major axis is 6678 km and eccentricity is a value of 0.6.

The position error indicates that a lower bound occurs for an semi-major axis of 18504.7 km. At this value of semi-major axis, the position error is held to a magnitude lower bound of 4 km. The other two values of semi-major axis do not have sufficient data to confirm a lower bound. However, there is a lower bound for velocity errors. An semi-major axis of 6678 km has a lower bound around 2e-3 km/s error, an semi-major axis of 18504.7 km has a lower bound at 5e-4 error, and an semi-major axis of 42158 km have lower bounds of 8e-5 km/s.

Semi-major axis is a strong indicator of overall XNAV performance, even with the variation of other orbit parameters. Though the other orbit parameters may cause the solution to diverge, the value of semi-major axis caps the lower bound of velocity state error. The previous section detailed how the increase of semi-major axis increases the orbital period, decreases the average orbit velocity, and increases the visibility of pulsars. While the other orbit parameters can also change these resources for XNAV, they are not directly involved in influencing all the stated metrics. semi-major axis is a critical choice when deciding if XNAV measurements are practical for an Earth orbit.

Looking at eccentricity, the data is now divided into three values of eccentricity in Figure 6.46. The other degrees of freedom are then varied to observe any possible

www.manaraa.com

behaviors.

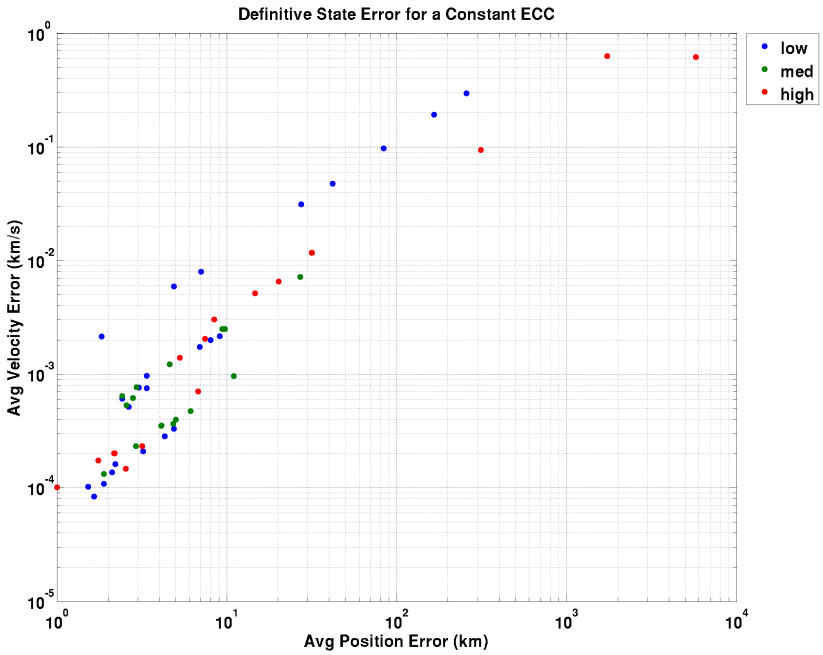

Figure 6.46: Varying other Kepler elements with a Constant ECC to Observe Average Position and Velocity Error over the Last Simulation Day.

Eccentricity does not have as much of an influence on the other orbital elements as compared to semi-major axis, seen in Figure 6.46. Most of the cases with a velocity error over 1e-3 km/s either have an eccentricity of 0.0 or 0.6. For the same variations in all other orbital elements, an eccentricity of 0.3 bounds the solution to within 50 km position error and 15e-3 km/s velocity error. The cases with an eccentricity of 0.0 or 0.6 have over 10% of their cases outside of these bounds. Choosing an eccentricity that is closer to 0.3 decreases the spread of position and velocity errors to below 50 km and 15e-3 km/s error.

The value of eccentricity influences in-plane orbit dynamics by extending and contracting the orbit. In doing so, it also has an influence on out-of-plane orbit

www.manaraa.com

dynamics thanks to the J_2 perturbation. With Kepler's laws, the eccentricity also changes the time the spacecraft spends at each part of the orbit which can change pulsar visibility. However, the orbit semi-major axis sets the orbital period, so eccentricity as a parameter manipulates only the distribution of time spent within that orbital period. Argument of periapsis, right ascension of the ascending node, and inclination also influence the orientation of the perigee and apogee of the orbit. The relative time spent at apogee could equate to either large periods of pulsar visibility or large periods of pulsar occultation.

XNAV performance versus eccentricity is dependent on the value of semi-major axis. An LEO will see a greater benefit from varying eccentricity than GEO. This is because, for a given semi-major axis, the value of eccentricity is a trade between the benefit of the orbit's increased apogee versus the demerit of a decreased perigee. A larger value of eccentricity produces a larger apogee and a smaller perigee. A larger value of apogee can provide longer periods of visibility on a pulsar target. If that pulsar target is in-plane with the orbit, the timing information from photon TOAs will better estimate the orbit. However, this is sensitive to the orientation of the orbit plane, making it sensitive to inclination, argument of periapsis and right ascension of the ascending node. On the other hand, the increase in eccentricity causes further argument of periapsis precession. This ultimately rotates the orbit apogee, which manipulates the distribution of pulsar visibility over an orbit. This behavior makes the orbit harder to estimate with XNAV. This is the first order trade off of eccentricity sensitivity to the other orbit parameters.

Looking at inclination, the data is now divided into three values of inclination

www.manaraa.com

in Figure 6.47. The other degrees of freedom are then varied to observe any possible behaviors.

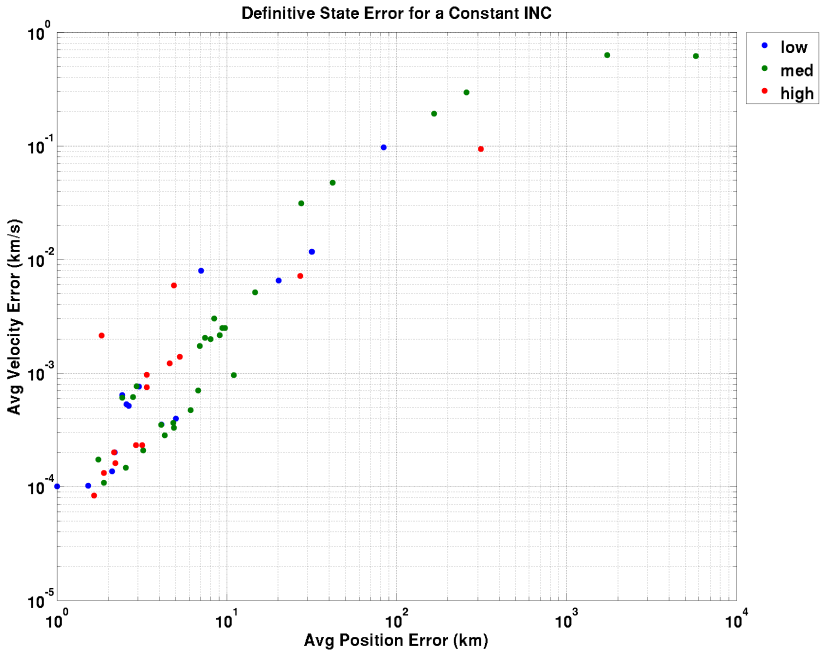

Figure 6.47: Varying other Kepler elements with a Constant INC to Observe Average Position and Velocity Error over the Last Simulation Day.

The variation of orbit parameters based on inclination are also significantly coupled, as seen in Figure 6.47. About 85% of orbits with 0° INC are bounded to less than 10 km position error and 10e-3 km/s velocity error, unlike the performance with 90° or 180° INC. The orbit with a 90° INC show a lower number of cases inside of these bounds at around 77%. The added occultations of Earth's magnetic poles are directly oriented with orbits near +/- 90°, and thus the results with the median inclination of 90°shows the highest number of outliers. At the upper end of the trade space, the retrograde orbit of inclination 180°is orientated in the same physical plane a 0°orbit. Though the orbit is now in retrograde with the reversed cadence of pulsar

www.manaraa.com

XNAV measurements, there are about 82% of orbits that are bounded to less than 10 km position and 10e-3 km/s velocity error. This percentage is within 3% of an orbit inclination of 0°.

INC influences the spacecraft's ambient background radiation and its orbit J_2 perturbation. While the in-plane orbit parameters of semi-major axis and eccentricity have a strong influence on all the resources needed for XNAV, the orbit inclination's influence is on visibility and the spacecraft dynamics. When the orbit is away from 90° INC, the variation of other orbit parameters have a greater sway over the total pulsar visibility than inclination. On the other hand, as the value of inclination reaches 90°, the higher order gravity terms have less and less of an influence on argument of periapsis and right ascension of the ascending node as seen in Equation (2.14) and (2.15). However, semi-major axis and eccentricity are still active indicators of these equations which minimizes the influence of inclination on the orbit's out-of-plane motion.

Looking at argument of periapsis and right ascension of the ascending node, the data is now divided into three values of argument of periapsis in Figure 6.47 and three values of right ascension of the ascending node in Figure 6.49. The other degrees of freedom are then varied to observe any possible behaviors.

www.manaraa.com

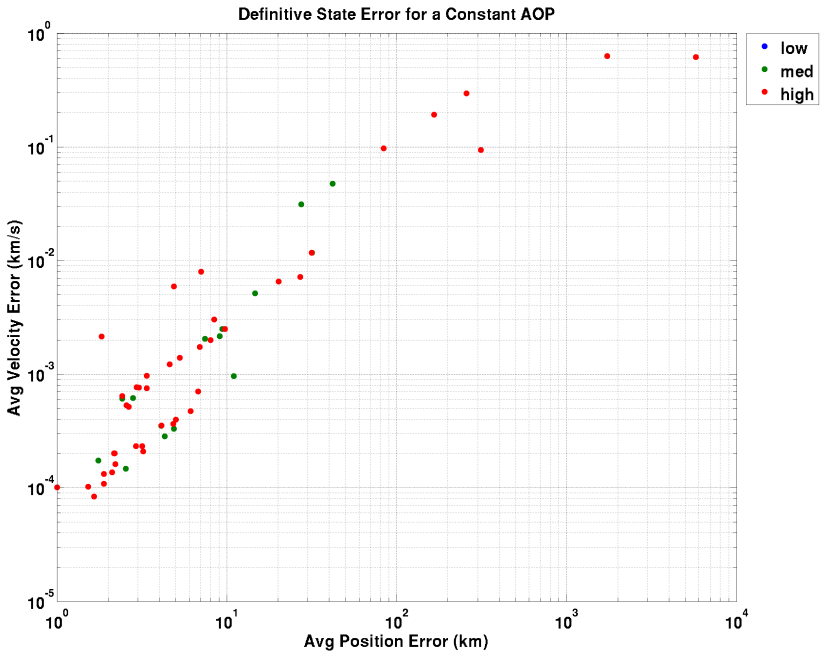

Figure 6.48: Varying other Kepler elements with a Constant AOP to Observe Average Position and Velocity Error over the Last Simulation Day.

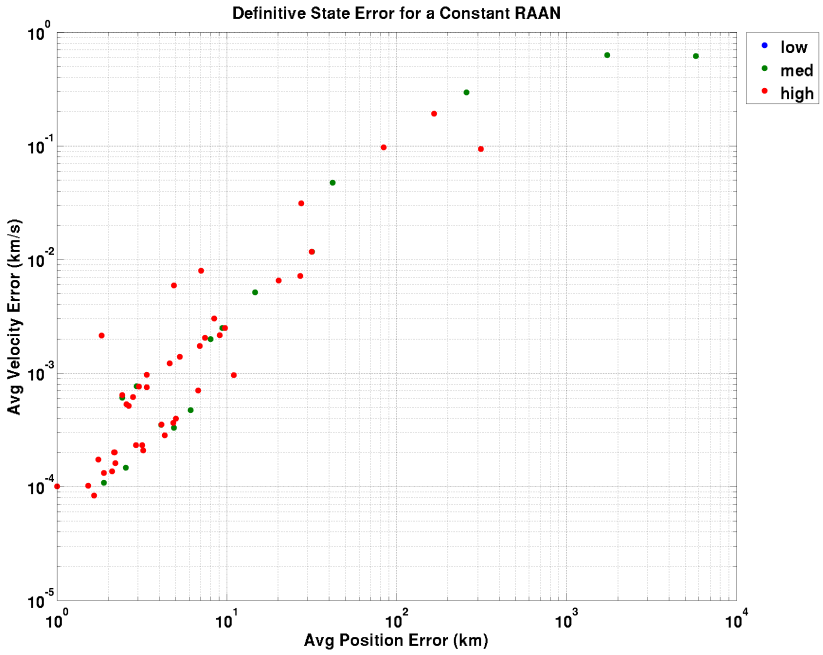

Figure 6.49: Varying other Kepler elements with a Constant RAAN to Observe Average Position and Velocity Error over the Last Simulation Day.

www.manaraa.com

XNAV performance distributions across Figures 6.48 and 6.49 are thoroughly mixed and sensitive to the other values of orbit parameters. The lower and upper bounds of these orbital angles also place the spacecraft in the same initial state, but unlike inclination, they result in the exact orbit trajectory. Even with the median values of 180°for both angles having different orbit plane orientations, they still fall into similar distributions of performance that are spread across both figures. An orbit design based on argument of periapsis and right ascension of the ascending node are very sensitive to the other orbit parameters.

The sensitivity of argument of periapsis and right ascension of the ascending node is due to the force model of the spacecraft dynamics. One of the major force models used in this thesis is the higher order non-spherical gravity terms. As seen in Equation (2.15), the semi-major axis, inclination, and eccentricity all have a direct influence on a rate of change of argument of periapsis and right ascension of the ascending node. Finally, it is important to note that eccentricity and inclination could be a value of 0 or 0° in this analysis. These orbit values would make the angle argument of periapsis or right ascension of the ascending node an undefined value, respectively. That implies that the average position/velocity error will be completely decoupled from the initial value of argument of periapsis or right ascension of the ascending node, whichever one is undefined.

If either angle is defined, argument of periapsis and right ascension of the ascending node shift periods of pulsar visibility by shifting the inertial location of orbit perigee and apogee. They are two angles that do not have a direct influence on the other orbit parameters by angle definition, and they do not have influences

www.manaraa.com

on the orbit dynamics due to the J_2 perturbation. However, as the orbit requires these two angles to fully define a spacecraft state, they help define the initial XNAV measurements which will reduce state estimation error throughout the experimental period.

www.manaraa.com

Chapter 7: Conclusions and Recommendations

The initial orbit parameters of a closed Earth orbit are an indicator of expected XNAV tracking performance. These parameters drive the availability, frequency, and the overall quality of pulsar XNAV measurements. This thesis shows a deeper insight on how XNAV performs with simulated hardware. The following chapter covers the orbital elements and how they interplay with the spacecraft orbit. It then provides a listing of future work and concludes with final comments on the subject of XNAV.

7.1 Summary of Results

Initial orbit parameters of closed Earth orbits are an indicator of XNAV performance in terms of pulsar availability, the background radiation environment and the resultant spacecraft dynamics. The results of this thesis show a sensitivity of the EKF state estimate performance based on the resultant cadence of XNAV measurements. That cadence is a result of pulsar availability and the measurement quality, whose behavior is a result of spacecraft dynamics and ambient background radiation. The majority of orbits can be tracked with XNAV measurements to within no more than 10 km position error, worst direction, in the 3 day experiment period.

www.manaraa.com

If the orbit parameters are restricted to a particular subset, this can improve to no more than 5 km position error, worst direction, over 1 day. This section summarizes the influences that each orbit parameter has on XNAV performance. The subsequent section enumerates the discrete design range suitable for no more than 5 km position error, worst direction.

The primary indicators of XNAV performance are SMA and ECC. There is observable behavior that the these orbit parameters will influence pulsar visibility, in-plane orbit dynamics, and the spacecraft's ambient background radiation. None of the other orbit parameters have this entire set of influences. SMA and ECC indicate the background environment and influence the total visibility on each pulsar target. This is because these two parameters control the radial distance of the spacecraft from Earth, the value used to define both background radiation as well as occultations due to Earth. The in-plane dynamics of a spacecraft are also driven by these two parameters. The specific energy of an orbit is primarily driven by SMA, while the instantaneous velocity at a given point on an orbit is driven by ECC.

The INC of an orbit also drives the environment for XNAV measurements as well as the underlying spacecraft dynamics. The occulted magnetic pole regions due to the dynamic variation of background radiation results in periodic breaks in visibility with orbits close to +/- 90°inclinations. In conjunction with SMA and ECC, the non-spherical gravitational acceleration J_2 modifies the rate of change of AOP and RAAN. This perturbation changes the periodic timing of pulsar visibility/pulsar measurements and thus the overall performance of XNAV. Between SMA, ECC, and INC, orbit determination using XNAV measurements can consis-

www.manaraa.com

tently drop down to ≤ 5 km position error over a single orbit period.

Finally, AOP and RAAN complete the orbit that drives the immediate cadence of XNAV measurements. While the realm of possible XNAV measurements are already set by SMA, ECC and INC, the initial AOP and RAAN are required to fully define the orbit. As the chosen EKF and the XNAV measurement model relies on a state estimate, an appropriate AOP and RAAN introduces an initial pulsar measurement.

7.2 Effective Closed Orbits for XNAV Tracking

XNAV tracking, by design, is for planetary and interplanetary missions beyond Saturn. XNAV performance will not compare to other navigation assets near Earth. Observations with this thesis' formulation of X-ray detector hardware will provide 3-5 km position accuracy with 600-1000 seconds of pulsar observation time per measurement. On the other hand, GPS can provide a measurement within a second and to within tens of meters of position accuracy [23]. However, Earth is a practical basis of which to evaluate XNAV for future planetary missions where other navigation assets drop off in performance [23]. It is also required from a programmatic standpoint to test XNAV around Earth in order to justify its use for other types of orbit trajectories. This section considers effective XNAV tracked orbits based on the Kepler elements. This information is a basic summary for those who wish to evaluate XNAV tracking performance for their spacecraft mission. It will provide XNAV only tracking performance to no more than 5 km position error,

www.manaraa.com

worst direction.

With SMA, XNAV tracking is ideal when SMA is pushed the upper bounds of the trade space, which in this case is an SMA of 42158 km. This is to provide effective pulsar visibility, a longer orbital period, and avoid the Van Allen belts. The average spacecraft orbital velocity over an orbit also decreases which also improves XNAV tracking performance.

With ECC, XNAV tracking is ideal when the orbit is circular or slightly eccentric (between 0.0-0.2 ECC). For smaller values of SMA with a smaller orbit period, a mission that has some ECC and is aligned with a chosen set of pulsar targets will benefit from XNAV measurements.

With INC, XNAV tracking is ideal when the orbit is away from 90° INC. The magnetic poles of Earth were occulted areas in this thesis. As such, the 90° INC would align the orbit plane so that the spacecraft would pass each pole with each orbit, breaking up pulsar visibility.

With AOP and RAAN, these orbit parameters are the most sensitive to the other orbit parameters. The J_2 perturbation (defined by the other orbit parameters) causes both these angles to change over time. Meanwhile, the values themselves do not have a direct influence on the other orbit parameters. The ideal values for AOP and RAAN is dependent on each individual orbit. They are based on the chosen pulsar targets, the scheduling algorithm, and the resultant XNAV measurements on the EKF performance. A full summary of these parameters are stated in Table 7.1.

It is also important to note that J_2 perturbations cause secular changes in the orbit plane when AOP and RAAN are defined. For a circular and equatorial

www.manaraa.com

Table 7.1: Orbit Design Range for XNAV Tracking

Initial Orbit Parameter	Ideal Value for XNAV Tracking
SMA	42158 km (Maximize This Orbit Parameter)
ECC	0.0 - 0.2
INC	Away from 90 degrees
AOP	Dependent on Pulsar Choices and other Orbit Parameters
RAAN	Dependent on Pulsar Choices and other Orbit Parameters

orbit, these two angles do not apply. Thus, a GEO orbit is an effective candidate to provide within 5 km position error after 1 day of propagation using XNAV.

Finally, it is important to note that the X-ray hardware drives XNAV performance. In this thesis, many of the constants were set due to X-ray hardware. This includes the total observation time needed for an XNAV measurement, the background radiation rejection model, and the operational constraints of the hardware. Future developments in X-ray detector hardware has the potential to improving XNAV tracking performance. These orbit settings will still have use with XNAV tracking. However, the improvement of X-ray detector technology will only widen the potential for XNAV tracking performance.

In summary, XNAV can provide a consistent position accuracy of within 10 km position error, worst direction. With the metrics summarized in Table 7.1, it can provide position accuracy within 5 km position error, worst direction. Within Table 7.1, the simple answer is to consider an Earth GEO for XNAV.

www.manaraa.com

7.3 Future Work and Final Comments

The inherent assumptions made in this formulation of XNAV can be expanded in a variety of ways, each adding a level of reality to XNAV navigation performance. This formulation balances its focus on an implementation with closed Earth orbits using a realization of X-ray detector hardware.

It is important to note that many of the trends enumerated in this thesis can generally translate to central body orbits around other bodies. The primary drivers of navigation performance come from visibility, the ambient background radiation, and the relative spacecraft dynamics. The central body's mass, radius, and background radiation are the parameters needed. A smaller body will have more pulsar visibility and strengthen navigation performance, a stronger radiation environment will weaken measurements and weaken navigation performance, and a more massive body will change the relative dynamics, all for a given orbit state. Further study can better bridge this relationship for future XNAV studies.

Throughout this thesis, various suggestions of future work are presented in various areas within the thesis framework, primarily based on removing assumptions. In summary, potential future work includes:

1. Focusing this entire thesis around a different planetary body, or for interplanetary trajectories (Chapter 1).

2. The inclusion of added orbital force models such as atmospheric drag, solar radiation pressure, and third body forces into the spacecraft state dynamics

www.manaraa.com

(Chapter 2).

3. Choosing a different set of parameters to define the orbit design (Chapter 2).

4. The use of a different filter model than the EKF, as suggested and studied by various other researchers in the field (Chapter 2).

5. The inclusion of the process noise matrix and thus characterizing EKF performance for a specific orbit design (Chapter 2).

6. The addition of further pulsar targets and the appropriate timing models required to support them (Chapter 3).

7. A deeper investigation on X-ray detector hardware and a more detailed background radiation model for the given orbit trade space (Chapter 4).

8. Removing the fixed observation time of each pulsar and allowing the scheduling algorithm to explore the use of a variable observation period (Chapter 5).

9. Including an example spacecraft as a systems level design of XNAV hardware(Chapter 5).

10. Expanding the local optimization strategy heuristic used in scheduling and explore further optimization strategies (Chapter 5).

There are numerous avenues of further research. This thesis was designed to provide initial insight into closed Earth orbits and can be used as a basis to characterize closed orbit regimes around other large celestial bodies. Most of the future work consists of changing settings or using different models. However, the

www.manaraa.com

first item, the seventh item, and the last item are significant changes to the thesis. They are accepted limits of scope in this thesis. The following three paragraphs address these items because they provide the most potential for future work.

The first item states that future work could go into studying a different planetary body or an interplanetary orbit. It has been stated previously that there are other navigation assets that would surpass XNAV in tracking performance around Earth. Traditionally, research in the field of XNAV is for interplanetary orbits. This thesis was chosen because the author saw potential knowledge gained about XNAV tracking by studying closed Earth orbits. The background environment is better defined around Earth as well as the higher order spacecraft dynamics. For a planetary body other than Earth, this information is not as well defined. There is also limited research on XNAV tracking with planetary orbits. Moving forward, there is definitely a lot of potential work that this thesis did not study in the traditional areas of interplanetary orbits. This thesis is just a first step in testing XNAV using the restrictions of current X-ray detector hardware.

The seventh item goes into an investigation about X-ray detector hardware and background radiation. The radiation model used in this thesis was specific to this simulation and based on the NICER X-ray detector. This thesis also made the broad assumption that the hardware will still function in the entire orbit trade space. In truth, this detector would not function properly. Seeing as the background radiation in this thesis can remove up to 10-15% of all XNAV measurements, understanding how much rejection can be achieved is critical to further research on XNAV tracking performance. It is also important to accurately model the Earth

www.manaraa.com

background radiation as well. This thesis used a basic metric (orbit altitude) to determine this value. It also scaled the radiation to the limits of the software. Background radiation is a significant driver of XNAV measurements, and should be a driving factor in determining if XNAV use is appropriate for orbit determination.

Finally, the last item mentions the significant complexity of pulsar scheduling. The simplest solution is to provide an X-ray detector that can collect photons from all pulsars at all times. To the author's best knowledge, there is not a working X-ray detector that has this operational capability for XNAV. Any work on this would be related to the trade study mentioned in item ten. If scheduling is needed, the pulsar schedule is a dynamic programming problem. The resources for XNAV dynamically change for each time step of the experimental period and the scheduler must accommodate for all possible observations. In the process, the scheduler also drives which pulsar targets are required for XNAV.

This thesis proposes a novel scheduling formulation that has provided convergence to over 75% of the trade space. If the trade space is reduced, further optimization techniques may prove to be incredibly beneficial for XNAV.

The harsh reality of space flight is that any spacecraft mission, for any purpose, requires a great amount of risk, capital, and personnel to bring to fruition. XNAV is a technology that uses celestial sources and has the potential as an autonomous navigation asset for missions far from Earth. However, the costs and uncertainty of using XNAV technology increases significantly for these orbit designs. The development of XNAV is reliant on finding creative and cost effective opportunities to demonstrate performance and justify its worth. The SEXTANT mission is an

www.manaraa.com

example of such an opportunity, with its launch in 2016 to the ISS.

Testing XNAV around Earth, with the added knowledge gained for other closed planetary orbits is, in the opinion of the author, a cost effective step for XNAV development. It is a realistic way to evaluate XNAV for the 21st century.

www.manaraa.com

Appendix A: X-ray Detector Survey

X-ray detectors work by measuring the energy that is released when X-ray photons collide with detector material atoms. That energy is proportional to the amount of photons that are detected. Some common types of detectors are listed below which come from various references. Please see these references for further details [46] [25].

1. Proportional Counters: A windowed chamber filled with an inert gas, electrodes produce a high/low electric field to determine a 2-D position of the photon arrival. A photoelectron is generated when an X-ray photon arrives which is amplified by the ionized gas. This magnitude is recorded to calculate the energy of the X-ray photon. Microsecond timing is possible, but it is limited by anode wire damage and the lifetime of the inert gas.

2. Microchannel Plates: A tightly packed set of 10 mm diameter glass tubes within a UV Filter. When an X-ray photon arrives, it interacts with the glass and electrodes with the photoelectric effect, producing electrons. A position sensitive plate is aligned on the other side of the glass tubes which detects these electron interactions. Nanosecond timing is possible but there is a high cost to manufacturing channel plates.

www.manaraa.com

3. Scintillators: A telescope instrument that uses crystals to convert X-ray photons into visible light. This light then interacts with a photo cathode and multiplier to be detected by a plate at the other end of the telescope.

4. Calorimeters: A device that uses a thermistor to measure induced temperature pulses within a cryogenically cooled matter that interacts with incoming X-ray photons. Costly to maintain with the power costs of cooling the instrument, it does have possible nanosecond level timing.

5. Charge-Coupled Device Semiconductors: As with the namesake, it is an array of charge coupled semiconductors made of metal oxide silicon capacitors which are charged by the arrival of X-ray photons. Avionics systems scan and clear these semiconductors for any increased charge due to X-ray photons. They are particularly useful for imaging X-ray photon arrivals. It is possible to reach microsecond level timing with these instruments.

6. Solid State Semiconductors: A device that consists of doped semiconductors that create electron hole pairs when interacting with X-ray photons. The pairs are multiplied in order to calculate the X-ray energy of photons. Microsecond level timing is possible.

7. Silicon Drift Detectors: A device that measures X-ray photon energy by the ionization of high purity silicon. Once the electron arrives, a series of ring electrodes drift the electron into a collection electrode, allowing the instrument to measure higher count rates. Nanosecond level timing is possible.

www.manaraa.com

Bibliography

[1] C.H. Acton. Ancillary data services of NASA's navigation and ancillary information facility. *Planetary and Space Science*, 44(1):65–70, 1996.

[2] NASA Administration. FY 2016 NASA Budget Estimates. `http://www.nasa.gov/sites/default/files/files/NASA_FY2016_Summary_Brief_corrected.pdf`, 2015.

[3] K.D. Anderson, D.J. Pines, and S.I. Sheikh. Validation of pulsar phase tracking for spacecraft navigation. *AIAA Journal of Guidance, Control and Dynamics*, 38 No.10:1885–1897, 2015.

[4] D. Baker, S. Kanekal, X. Li, S. Monk, J. Goldstein, and J. Burch. Letters to nature: An extreme distortion of the van allen belt arising from the 'hallowe'en' solar storm of 2003. *Nature*, 432:878–881, 2004.

[5] R.R. Bate, D.D. Muller, and J.E. White. *Fundamentals of Astrodynamics*. Dover, New York, 1971.

[6] R.H. Battin. *An Introduction to the Mathematics and Methods of Astrodynamics, Revised Edition*. American Institute of Aeronautics and Astronautics (AIAA), Washington, D.C., 1999.

[7] P.G. Brown and P.Y.C. Hwang. *Introduction to random signals and applied Kalman filtering*. Wiley, Ann Arbor, Michigan, 1997.

[8] S. Bucher, B. Williams, M. Pendexter, and D. Balke. Chandra mission scheduling on-orbit experience. *Observatory Operations: Strategies, Process and Systems II*, 2008.

[9] J.R. Carpenter and K.T. Alfriend. Navigation accuracy guidelines for orbital formation flying. *The Journal of the Astronautical Sciences*, 53 No.2:207–219, 2005.

[10] J.R. Carpenter and E.R. Schiesser. Semimajor axis knowledge and GPS orbit determination. *Navigation: Journal of the Institute of Navigation*, 48 No.1:57–68, 2001.

www.manaraa.com

[11] NASA Goddard Space Flight Center. Imagine the Universe: Astronomer's Toolbox. http://imagine.gsfc.nasa.gov/science/toolbox/timing2.html, 2013.

[12] NASA Goddard Space Flight Center. NICER: Mission Overview. https://heasarc.gsfc.nasa.gov/docs/nicer/nicer_about.html, 2014.

[13] T. J. Chester and S. A. Butman. Navigation using X-ray pulsars. *Jet Propulsion Laboratory, Pasadena, CA, NASA Tech. Rep. 81N27129*, 1981.

[14] A. Chulliat, S. Macmillian, P. Alken, C. Beggan, M. Nair, B. Hamilton, A. Woods, V. Ridley, S. Maus, and A. Thomson. The US/UK world magnetic model for 2015-2020: Technical report. *National Geophysical Data Center, NOAA*.

[15] T. Cormen, C. Leiserson, R. Rivest, and C. Stein. *Introduction to Algorithms*. MIT Press, Boston, 3rd edition, 2009.

[16] CSIRO. Australia Telescope National Facility. http://www.atnf.csiro.au/.

[17] H.D. Curtis. *Orbital Mechanics for Engineering Students*. Elsevier, Oxford, UK, 2005.

[18] L. Cutler and C. Searle. Some aspects of the theory and measurement of frequency fluctuation in frequency standards. *Proceedings of the IEEE*, pages 136–154, 1966.

[19] NASA: Space Technology Game Changing Development. Station Explorer for X-Ray Timing and Navigation (SEXTANT). https://gcd.larc.nasa.gov/projects/deep-space-x-ray-navigation-and-communication/#.VOvcNvnF81I, 2015.

[20] G. S. Downs. Interplanetary navigation using pulsating radio sources. *NASA Technical Reports, N74-34150*, pages 1–12, 1974.

[21] R. T. Edwards, G. B. Hobbs, and R. N. Manchester. TEMPO2, a new pulsar timing package - II. the timing model and precision estimates. *Monthly Notices of the Royal Astronomical Society*, 372(4):1549–1574, 2006. pre-print: arXiv:astro-ph/0607664.

[22] A. A. Emadzadeh. *Relative navigation between two spacecraft using X-ray pulsars*. PhD thesis, University of California, Los Angeles, 2009.

[23] A. A. Emadzadeh and J. L. Speyer. *Navigation in space by X-ray pulsars*. Springer, 2011.

[24] ESA. ESA Space Environment Information System. https://www.spenvis.oma.be/, 2015.

www.manaraa.com

[25] G.W. Fraser. *X-ray Detectors in Astronomy*. Cambridge University Press, Cambridge, UK, 1989.

[26] K. C. Gendreau, Z. Arzoumanian, T. Okajima, and the NICER Team. The Neutron-star Interior Composition ExploreR (NICER): an Explorer mission of opportunity for soft X-ray timing spectroscopy. In *Space Telescopes and Instrumentation: Ultraviolet to Gamma Ray*, volume 8443 of *Proc. SPIE*. International Society for Optics and Photonics, Sep 2012. doi:10.1117/12.926396.

[27] J. E. Hanson. *Principles of X-ray navigation*. PhD thesis, Stanford University, March 1996.

[28] Jacob M. Hartman and Paul S. Ray. Timing accuracy for spin-powered millisecond pulsars: A comparison of predictions and rxte observations. DARPA XNAV Program Memo, 2005.

[29] John Hartnett and Andre Luiten. Colloquium: Comparison of astrophysical and terrestrial frequency standards. *Review of Modern Physics*, 83:1–9, 2011.

[30] J. Heirtzler. The future of the south atlantic anomaly and implications for radiation damage in space. *Journal of Atmospheric and Solar-Terrestrial Physics*, 64:1701–1708, 2002.

[31] G. B. Hobbs, R. T. Edwards, and R. N. Manchester. TEMPO2, a new pulsar-timing package - i. an overview. *Monthly Notices of the Royal Astronomical Society*, 369:655–672, June 2006.

[32] S. P. Hughes. General Mission Analysis Tool (GMAT). Retrieved Sep 6 2012.

[33] N. James, R. Abello, M. Lanucara, M. Mercolino, and R. Madde. Implementation of an ESA delta-DOR capability. *Acta Astronautica*, pages 1041–1049, 2006.

[34] M. Johnston and H. Adorf. Scheduling with neural networks- the case of Hubble Space Telescope. *Computers and Operations Research*, 19 Issues 3-4:209–240, 1992.

[35] J.F. Jordan. Navigation of Spacecraft on Deep Space Missions. *Journal of Navigation*, 40(1):19–29, 1987.

[36] Anne Long. *Goddard Enhanced Onboard Navigation System (GEONS) Mathematical Specifications*. a.i. solutions Inc., November 2012. FDSS-23-0035, Version 2, Release 2.17.

[37] Anne Long. *Goddard Enhanced Onboard Navigation System (GEONS) System Description and User's Guide*. a.i. solutions Inc., November 2012. FDSS-23-0026, Version 2, Release 2.17.

www.manaraa.com

[38] D.N. Matsakis, J.H. Taylor, and T.M. Eubanks. A statistic for describing pulsar and clock stabilities. *Astronomy and Astrophysics*, 326:924–928, 1997.

[39] Jason W. Mitchell, Munther A. Hassouneh, Luke M. Winternitz, Jennifer E. Valdez, Paul S. Ray, Zaven Arzoumanian, and Keith C. Gendreau. Station Explorer for X-ray Timing and Navigation Technology Architecture Overview. In *Proceedings of the 27th International Technical Meeting of the Satellite Division of the Institute of Navigation (ION GNSS+)*. Institute of Navigation, 2014.

[40] NASA. Chandra X-ray Observatory. `http://www.nasa.gov/chandra`, 2015.

[41] NASA. Hubble Space Telescope. `http://www.nasa.gov/mission_pages/hubble/main/index.html`, 2015.

[42] NASA. ROSAT Spacecraft Webpage. `http://science.nasa.gov/missions/rosat/`, 2015.

[43] NASA's Rossi X-Ray Timing Explorer Completes Mission Operations. Retrieved Sep 22 2012.

[44] NOAA. NOAA Geomagnetic Map. `http://www.ngdc.noaa.gov/geomag/WMM/data/WMM2015/WMM2015_F_MERC.pdf`, 2015.

[45] P. Reichley, G. Downs, and G. Morris. Use of pulsar signals as clocks. *NASA Jet Propulsion Laboratory Quarterly Technical Review*, 1 No.1:80–86, 1971.

[46] S. I. Sheikh. *The use of variable celestial X-ray sources for spacecraft navigation.* PhD thesis, University of Maryland, 2005.

[47] Sky Server Voyages. Voyages: Expeditions. `http://dev.skyserver.sdss3.org/voyages/pre-flight/ra-and-dec.aspx`, 2015.

[48] B.D. Tapley, B.E. Schutz, and G.H. Born. *Statistical Orbit Determination.* Elsevier Academic Press, Burlington, MA, 2004.

[49] D. Vallado. *Fundamentals of Astrodynamics and Applications.* McGraw Hill, Space Technology Series, New York, 1997.

[50] J. Van Allen and Louis Frank. Radiation around the earth to a radial distance of 107,400 km. *Nature*, 183:430–434, 1959.

[51] J. Vette. The ae-8 trapped electron model environment. *NASA Technical Report*, 1991.

[52] K. Wallace. Radio stars, what they are and the prospects for their use in navigation systems. *Journal of Navigation*, pages 358–374, 1988.

www.manaraa.com

[53] Luke M. B. Winternitz, Munther A. Hassouneh, Jason W. Mitchell, Fotis Gavriil, Zaven Arzoumanian, and Keith C. Gendreau. The Role of X-rays in Future Space Navigation and Communication. In *36th Annual Guidance & Navigation Control Conference*. American Astronautical Society, February 2013.

[54] Luke M. B. Winternitz, Munther A. Hassouneh, Jason W. Mitchell, Jennifer E. Valdez, Samuel R. Price, Sean R. Semper, Wayne H. Yu, Paul S. Ray, Kent S. Wood, Zaven Arzoumanian, and Keith C. Gendreau. X-ray Pulsar Navigation Algorithms and Testbed for SEXTANT. In *IEEE Aerospace Conference*. IEEE, March 2015. Accepted for publication.

[55] K. S. Wood. Navigation Studies Utilizing The NRL-801 Experiment and the ARGOS Satellite. In *Proc. SPIE*, volume 1940, pages 105–116, 1993.

[56] D. W. Woodfork. The use of x-ray pulsars for aiding GPS based satellite orbit determination. Master's thesis, Air Force Institute of Technology, March 2005.

www.manaraa.com